Geology and Geochemistry of Noachian Bedrock and Alteration Events, Meridiani Planum, Mars: MER Opportunity Observations

David W. Mittlefehldt[1], Ralf Gellert[2], Scott J VanBommel[3], Raymond E. Arvidson[3], James Warren Ashley[4], Benton C. Clark[5], Larry S. Crumpler[6], William H Farrand[5], Matthew P. Golombek[7], John A. Grant[8], Richard V. Morris[1], and Christian Schroeder[9]

[1]NASA Johnson Space Center
[2]University of Guelph
[3]Washington University in St. Louis
[4]Jet Propulsion Laboratory/Caltech
[5]Space Science Institute
[6]New Mexico Museum of Natural History
[7]California Institute of Technology/JPL
[8]Smithsonian Institution
[9]University of Stirling

November 26, 2022

Abstract

We have used Mars Exploration Rover Opportunity data to investigate the origin and alteration of lithic types along the western rim of Noachian-aged Endeavour crater on Meridiani Planum. Two geologic units are identified along the rim. The Shoemaker formation consists of two types of polymict impact breccia: clast-rich with coarser clasts in upper units; clast-poor with smaller clasts in lower units. Comparison with observations at terrestrial craters show that the lower units represent more distal ejecta from one or more earlier impacts, and the upper units are ejecta from Endeavour crater. Both are mixtures of target rocks of basaltic composition. Subtle compositional differences are caused by differences in post-impact alteration along the crater rim. The lower Shoemaker units and the Matijevic formation represent pre-Endeavour geology, which we equate with the regionally mapped Noachian subdued cratered unit. An alteration style unique to these rocks is formation of Si- and Al-rich vein-like structures crosscutting outcrops, and formation of smectite. Post-Endeavour alteration is dominated by sulfate formation. Rim-crossing fracture zones include regions of alteration that produced Mg-sulfates as a dominant phase, plausibly closely associated in time with the Endeavour impact. Calcium-sulfate vein formation occurred over an extended time period, including pre-Endeavour impact and after the Endeavour rim had been substantially degraded, likely after deposition of the Burns formation that surrounds and embays the rim. Differences in Mg, Ca and Cl concentrations on rock surfaces and interiors indicate mobilization of salts by transient water that has occurred recently and may be ongoing.

Geology and Geochemistry of Noachian Bedrock and Alteration Events, Meridiani Planum, Mars: MER Opportunity Observations

David W. Mittlefehldt[1], Ralf Gellert[2], Scott vanBommel[2,3], Raymond E. Arvidson[3], James W. Ashley[4], Benton C. Clark[5], Larry S. Crumpler[6], William H. Farrand[5], Matthew P. Golombek[4], John A. Grant[7], Richard V. Morris[1], Christian Schröder[8]

[1]Mail code XI3, Astromaterials Research Office, NASA/Johnson Space Center, Houston, Texas 77058, USA.

[2]Department of Physics, University of Guelph, Guelph, ON N1G2W1, Canada.

[3]Department of Earth and Planetary Sciences, Washington University in Saint Louis, Saint Louis, Missouri 63130, USA.

[4]Jet Propulsion Laboratory, California Institute of Technology, Pasadena, California 91109, USA.

[5]Space Science Institute, 4765 Walnut St., Suite B, Boulder, Colorado 80301, USA.

[6]New Mexico Museum of Natural History and Science, 1801 Mountain Rd NW, Albuquerque, New Mexico 87104, USA.

[7]Smithsonian Institution, NASM CEPS, 6th at Independence Ave. SW, Washington, DC 20560, USA.

[8]Biological and Environmental Sciences, University of Stirling, Stirling FK9 4LA, Scotland, UK.

Journal of Geophysical Research: Planets

submitted: 31 March 2021

Abstract We have used Mars Exploration Rover Opportunity data to investigate the origin and alteration of lithic types along the western rim of Noachian-aged Endeavour crater on Meridiani Planum. Two geologic units are identified along the rim. The Shoemaker formation consists of two types of polymict impact breccia: clast-rich with coarser clasts in upper units; clast-poor with smaller clasts in lower units. Comparison with observations at terrestrial craters show that the lower units represent more distal ejecta from one or more earlier impacts, and the upper units are ejecta from Endeavour crater. Both are mixtures of target rocks of basaltic composition. Subtle compositional differences are caused by differences in post-impact alteration along the crater rim. The lower Shoemaker units and the Matijevic formation represent pre-Endeavour geology, which we equate with the regionally mapped Noachian subdued cratered unit. An alteration style unique to these rocks is formation of Si- and Al-rich vein-like structures crosscutting outcrops, and formation of smectite. Post-Endeavour alteration is dominated by sulfate formation. Rim-crossing fracture zones include regions of alteration that produced Mg-sulfates as a dominant phase, plausibly closely associated in time with the Endeavour impact. Calcium-sulfate vein formation occurred over an extended time period, including pre-Endeavour impact and after the Endeavour rim had been substantially degraded, likely after deposition of the Burns formation that surrounds and embays the rim. Differences in Mg, Ca and Cl concentrations on rock surfaces and interiors indicate mobilization of salts by transient water that has occurred recently and may be ongoing.

Plain Language Summary Data returned by the Mars Exploration Rover Opportunity was used to investigate rock origins along the western rim of Endeavour crater on Meridiani Planum, Mars. The Shoemaker formation consists of impact-formed breccia of two types: coarser-grained upper subunits and finer-grained lower subunits. The lower units represent ejecta from one or more older, more distant craters, while the upper units are ejecta from Endeavour crater. Subtle compositional differences are caused by differences in post-impact alteration along the crater rim. The lower Shoemaker units represent part of the pre-Endeavour geology. An alteration style unique to the pre-Endeavour rocks is formation of Si- and Al-rich structures crosscutting bedrock. Post-Endeavour alteration is dominated by sulfate formation. Fracture zones in the rim include regions of alteration that produced Mg-sulfates as a dominant phase, plausibly closely associated in time with the Endeavour impact. Calcium-sulfate vein formation occurred over an extended time period, some before the Endeavour impact and some much later, likely after deposition of the sulfate-rich sandstones of Meridiani Planum. Differences in composition of rock surfaces and interiors indicate that mobilization of salts by transient water has occurred recently and may be ongoing on Mars.

Keywords: Mars geology; Mars geochemistry; Noachian crust; Endeavour crater; Mars Exploration Rover mission

1. Introduction

Mars Exploration Rover (MER) Opportunity explored the geology of Meridiani Planum within Arabia Terra for 5111 Sols (Mars days), from the date of landing on 25 January 2004 through the loss of signal on 19 June 2018, which was caused by a global dust storm that choked off her solar energy supply. Through Sol 2680, corresponding to the first seven and a half Earth years of the mission, Opportunity traversed the hematite plains making observations of sulfate-rich sedimentary rocks and associated hematite-concretion surface-lag (Arvidson et al., 2011; Squyres et al., 2006a). These constitute the upper layers of the Late Noachian/Early Hesperian Meridiani upper etched unit and the Early Hesperian hematite unit (Hynek & Di Achille, 2017).

Opportunity began exploring the northwestern rim of Endeavour crater on Sol 2681 (09 Aug. 2011). Endeavour crater is a 22 km diameter complex impact structure (Fig. 1a) formed in Noachian aged materials that predate the embaying sulfate-rich sedimentary rocks (Arvidson et al., 2014; Hynek et al., 2002). The Endeavour crater rim was chosen as a target because the rocks record an ancient epoch in martian history, and because phyllosilicate minerals were identified on portions of the rim from orbit (Wray et al., 2009). The latter demonstrate that a period of aqueous alteration is recorded in the rocks. Exploration of Endeavour crater rim directly addressed one of the main goals of the MER mission: to explore regions and associated rocks and soils where water might have been present and to make assessments regarding past habitability (Squyres et al., 2003).

Post-impact erosion has degraded the Endeavour crater rim into a series of rim segments (Grant et al., 2016; Hughes et al., 2019). The first rim segment explored by Opportunity was the ~700 m long Cape York that rises ~10 m above the surrounding plains (Fig. 1b) (Grant et al., 2016). Near-infrared spectra from the Compact Reconnaissance Imaging Spectrometer for Mars (CRISM) instrument indicated the presence of phyllosilicates in this region (Wray et al., 2009). Investigations with the rover science payload revealed that the orbitally resolved phyllosilicates correspond to ferric smectite occurring roughly midway down the inboard (southeastern) side of Cape York (Fig. 1b; online supplement Fig. L01) (Arvidson et al., 2014). At that location, the thin, fine-grained clastic Matijevic formation is exposed. It was identified as being part of the pre-Endeavour basement and the host of the ferric smectite (Arvidson et al., 2014; Crumpler et al., 2015). Shoemaker Ridge forms the topographic expression of Cape York and is composed of Noachian polymict impact breccias formed by the Endeavour impact; these constitute the Shoemaker formation (Crumpler et al., 2015; Squyres et al., 2012). The Grasberg formation, a thin, very-fine-grained airfall unit that drapes the lower, eroded pediment surfaces of Endeavour rim segments, also occurs on Cape York (Crumpler et al., 2015; Grant et al., 2016).

Cape Tribulation is a major rim segment south of Cape York (Fig. 1c). This segment also presented evidence for the localized presence of phyllosilicates, particularly in the region of a large, rim-transecting valley named Marathon Valley (Fig. 1d; online supplement Fig. L04) (Fox et al., 2016; Wray et al., 2009). Exploration of Cape Tribulation began at its northern tip and continued to Perseverance Valley, which cuts the rim between the southern terminus of Cape Tribulation and the next rim segment, Cape Byron (Fig. 1e; online supplement Fig. L09). For most of the traverse, Opportunity explored rocks on the outboard (western) side of Cape Tribulation, but major science campaigns were done in Marathon and Perseverance Valleys. Both valleys cut the rim and expose bedrock of the lower stratigraphic section. The focus of the discussion takes over from where Mittlefehldt et al. (2018a) left off. This includes data for all rock targets analyzed from Sol 3935 (17 Feb. 2015) through the last contact science measurements on Sol 5105 (03 June 2018). We also discuss the erratic block Marquette Island which was discovered on the hematite plains on Sol 2055 (04 Nov. 2009). This block is interpreted to be an ejecta block of the Noachian crust that predates sedimentary rocks of the hematite plains (Arvidson et al., 2011). Soil analyses are not discussed in detail but are utilized to help interpret relationships among rock compositions.

The instruments of the Athena payload (Squyres et al., 2003) that were used to investigate the geology and geochemistry of the region include: the Alpha Particle X-ray Spectrometer (APXS; Rieder et al., 2003), the Microscopic Imager (MI; Herkenhoff et al., 2003), the Panoramic Camera (Pancam; Bell et al., 2003) and the Rock Abrasion Tool (RAT; Gorevan et al., 2003). These were supported by imaging from the engineering cameras – Navigation Cameras (Navcam) and front and rear Hazard Avoidance Cameras (Hazcam) (Maki et al., 2003). The MIMOS II Mössbauer Spectrometer (Klingelhöfer et al., 2003) was still operational during observations on Marquette Island; we include data from it in that discussion.

The major focus of this paper is on the compositional information returned by the APXS and its use in defining alteration processes. These data are put into geological context using information derived from orbital and *in-situ* mapping. Pancam and Navcam images are used to interpret outcrop textures and structures, and Pancam spectra are used to help constrain mineralogy. The micro-textures of the rocks are interpreted from MI images. The Mars observations are compared to rocks from terrestrial craters and tied to information derived from cratering mechanics studies. The observations discussed here are developed into a geological and alteration history for the region around Endeavour crater.

2. The APXS Dataset

The APXS determines chemical compositions of rocks and soils using X-ray spectroscopy after irradiation with energetic alpha particles and X-rays. It resembles a combination of the laboratory methods of X-ray fluorescence spectrometry (XRF) and particle induced X-ray emission spectrometry (Rieder et al., 2003). The analysis field of view has a diameter of 38 millimeters, but the instrument response is strongest in the central region. Concentrations are extracted from the X-ray spectra using the empirical method described in Gellert et al. (2006). Complete results for 287 analyses of rocks and soils from the Endeavour crater rim and 2σ precision errors of the peak areas are reported in Table 1. Of these, 141 analyses were previously unpublished. Locations for all analyses presented in Table 1 except for Marquette Island and soils far from Endeavour rim are shown in the online supplement. [Note to reviewers: All data tables will be hosted in an online data repository. An Excel file with these tables was uploaded for review purposes.] The table also includes the typical relative accuracy of the method, which is taken from Table 1 of Gellert et al. (2006), and the typical relative precision of the measurements based on a representative Shoemaker formation rock analysis, taken from

Table S1 of Mittlefehldt et al. (2018a). A detailed discussion of the methodology used here is presented in Mittlefehldt et al. (2018a).

3. Geological Context

The basement in the region explored by Opportunity consists of the Early to Middle Noachian subdued cratered unit (Hynek & Di Achille, 2017). This unit is interpreted to be composed of primary (volcanic, pyroclastic) and secondary (impact breccia, fluvial and aeolian sedimentary) lithic types (Hynek & Di Achille, 2017). This highlands unit is overlain by three Meridiani etched plains units; the lower two are Middle to Late Noachian in age; the topmost unit is Late Noachian/Early Hesperian in age (Fig. 2). These units are interpreted to be aeolian and/or volcanic deposits (Hynek & Di Achille, 2017; Hynek & Phillips, 2008). The Burns formation is the uppermost lithified section of the etched unit stratigraphy, and is sulfate-rich aeolian sandstone (e.g., Grotzinger et al., 2005; Squyres and Knoll, 2005; Squyres et al., 2006a).

Endeavour crater is northeast of the ~160 km-diameter Miyamoto crater (Grant et al., 2016; Newsom et al., 2003) which is in the subdued cratered unit (Fig. 2a). Miyamoto crater is an ancient, degraded crater partially filled by Meridiani etched plains units on the north-northeast side. Morphologic evidence points to fluvial erosion having impacted the landscape outside and inside the crater (Newsom et al., 2003, 2010). Iron-Mg-rich smectite phases are located on the western floor of Miyamoto crater (Wiseman et al., 2008). Bopolu crater, 19 km in diameter, impacted on the Meridiani etched plains units that partially fill Miyamoto crater. This is a fairly pristine crater that exposes altered Noachian basement in its walls (Grant et al., 2016), further testifying to ancient alteration of the Miyamoto crater floor rocks. Alteration in this region is thought to have been a response to the hydrological environment of western Arabia Terra in which groundwaters from the highlands to the south emerged in local topographic lows and caused alteration of the bedrock (Andrews-Hanna & Lewis, 2011; Andrews-Hanna et al., 2007). The Endeavour impact occurred ~20 km outside the rim of Miyamoto crater within the region of its continuous ejecta deposit. The pre-impact terrain would have included polymict breccias from that earlier impact and these could have been altered as observed for floor rocks in Miyamoto crater (Wiseman et al., 2008). Iazu crater is a 6.8 km-diameter structure ~25 km south of Endeavour crater (Fig. 2b). It is a relatively pristine, simple bowl-shaped crater surrounded by a pedestal of ejecta. That latter is thought to be the result of wind erosion preferentially removing the less resistant Burns formation rocks (Powell et al., 2017). Iazu crater exposes Noachian-aged, ferric-smectite-bearing altered basaltic-composition basement below Burns formation in its crater walls (Powell et al., 2017), further establishing that the pre-impact terrain for Endeavour crater consisted of ancient, altered rocks.

The stratigraphy in the region of Endeavour crater rim is divided into four formations which are, oldest to youngest; the Matijevic, Shoemaker, Grasberg and Burns formations (Crumpler et al., 2015). The Matijevic formation is part of the pre-Endeavour terrain exposed at the inboard side of Cape York (online supplement Fig. L01), and is a fine-grained clastic rock (Arvidson et al., 2014). The limited exposures prohibit firm conclusions regarding its origin, but its morphology and texture are consistent with formation as volcanic ash or distal impact ejecta (Crumpler et al., 2015). Polymict impact breccias of the Shoemaker formation comprise the major lithic type of the Endeavour crater rim on the segments explored by Opportunity and underpin the topographic expressions of the rim segments (Crumpler et al., 2015; Squyres et al., 2012). The Shoemaker formation, the major focus of this communiqué, is discussed in Section 4. A continuous bench of bright rock encircles Cape York (online supplement Fig. L01), partially surrounds the margin of Cape Tribulation and is discernable in High Resolution Imaging Science Experiment (HiRISE) images of other rim segments of Endeavour crater (e.g., Grant et al., 2016). This bench is part of the Grasberg formation, a very-fine-grained clastic deposit that drapes the eroded lower slopes of rim segments (Crumpler et al., 2015). The Grasberg formation is a thin, altered airfall deposit with possibly a weathering cap that is of volcanic or impact origin and might be regional in extent (Crumpler et al., 2015). New analyses of two Grasberg formation rocks are included in Table 1, but we do not discuss them; the composition of this formation is discussed in Mittlefehldt et al. (2018a). Finally, the Burns formation is dominated by sulfate-rich sandstones with a minor component of mudstone (e.g., Edgar et al., 2012; Grotzinger et al., 2005). Most of the sandstones are aeolian in origin, but there are some aqueous facies that bespeak local fluvial reworking and rare mudstones indicate localized deposition in quiet water, possibly a lacustrine setting (Edgar et al., 2012, 2014; Grotzinger et al., 2005, 2006; Hayes et al., 2011). Unconformities separate all formations.

There are several lithic types in the region that do not occur as mappable formations that are covered here under the rubric “dark rocks.” These include dark-rock boulder-float similar to those discussed previously (Mittlefehldt et al., 2018a), two types of scattered, more massive, fine-grained rock that we refer to as blue- and purple-rock erratics based on their appearance in Pancam false color images, and three types of dark rock from Perseverance Valley. Finally, we encountered a dark-rock block – Marquette Island – on the hematite plains roughly 11,800 meters from the Endeavour rim. Marquette Island is interpreted to be an ejecta fragment from the Noachian crust (Arvidson et al., 2011), and has a general compositional similarity to Adirondack-class basalts from Gusev crater but likely contains a higher fraction of light elements (H, C, O) than found for other rocks (Mittlefehldt et al., 2010). Because this might indicate unusual alteration, we discuss it here.

4. Shoemaker Formation

Shoemaker formation rocks are polymict impact breccias which we interpreted as being ejecta from Endeavour crater (Arvidson et al., 2014; Crumpler et al., 2015; Mittlefehldt et al., 2018a; Squyres et al., 2012). However, our later investigations in Marathon and Perseverance Valleys presented geological evidence that some subunits of the Shoemaker formation pre-date the Endeavour impact (Mittlefehldt et al., 2018b, 2019a). We present that evidence in this section and refine our interpretation of the Shoemaker formation. We present our compositional information on Shoemaker formation rock targets and discuss them in relation to our interpretation of subunit origins. Further, we discuss alteration features in the Shoemaker formation from Marathon and Perseverance Valleys, and compositional differences between surfaces and interiors of several rocks. The online supplement contains locator images for all Pancam images shown and rock targets called-out.

4.1 Stratigraphy, Texture, Morphology and Origin of Subunits

The Shoemaker formation is the major rock unit of the rim. It originally formed the continuous ejecta deposit surrounding Endeavour crater, but subsequent degradation has reduced its areal coverage (Grant et al., 2015). It is divided into three members on Cape York (Figs. 15, 17 of Crumpler et al., 2015). The Greeley Haven member is the thickest and uppermost subunit of the Shoemaker formation, and is a coarse, clast-rich polymict breccia with multi-cm-sized dark clasts in a brighter, fine-grained matrix (Fig. 3a) (Arvidson et al., 2014; Crumpler et al., 2015; Mittlefehldt et al., 2018a; Squyres et al., 2012). The Chester Lake member was encountered on the southern tip of Cape York when we began exploring the rim (online supplement Fig. L01) (Crumpler et al., 2015). Copper Cliff is the lowermost member and unconformably overlies the pre-impact Matijevic formation (online supplement Fig. L01) (Crumpler et al., 2015). It is a transitional breccia that shows some textural and compositional characteristics of the underlying Matijevic formation (Arvidson et al., 2014; Crumpler et al., 2015; Mittlefehldt et al., 2018a). Mittlefehldt et al. (2018a) concluded that the Copper Cliff member was formed by mixing Endeavour ejecta with material eroded from the pre-impact paleosurface via a ballistic erosion-sedimentation process (e.g., Hörz et al., 1983; Oberbeck, 1975).

The Shoemaker formation is subdivided into upper and lower subunits on Cape Tribulation, but no attempt was made to correlate them with the three members defined on Cape York. However, most of the breccias on Cape Tribulation discussed in Mittlefehldt et al. (2018a) are morphologically and texturally like the Greeley Haven member on Cape York (e.g., Fig. 3b). These are assigned to the upper Shoemaker subunit on Cape Tribulation (Crumpler et al., 2019, 2020). The area around the Spirit of Saint Louis feature and the floor of Marathon Valley contain breccias that have lower abundances of clasts and typically smaller clasts (Figs. 3d, e), which are mapped as two subunits (lower-1 and lower-2) of the Shoemaker formation (Crumpler et al., 2019; 2020). Previously, we did not recognize subunits of the Shoemaker formation on Cape Tribulation, although we noted that breccias at Cook Haven and at the Hueytown fracture zone showed some similarity to breccias now mapped as lower Shoemaker in Marathon Valley (Fig. 3c) (Mittlefehldt et al., 2018a). A single lower subunit of the Shoemaker formation is also recognized in the lower elevation of Perseverance Valley (Fig. 3f) (Crumpler et al., 2019; 2020).

We now identify the lower Shoemaker formation subunits as distal impact ejecta from one or more pre-Endeavour craters, and thus they are not correlative with the Shoemaker formation on Cape York. The arguments supporting this are based on comparing upper and lower Shoemaker rocks with an analysis of experimental and observational work on impact processes (Oberbeck, 1975) plus studies of terrestrial caters (e.g., Hörz et al., 1983; Mader & Osinski, 2018; Shoemaker, 1963).

As summarized by Oberbeck (1975), ejecta fragments from a crater are launched at differing angles and velocities, but all follow ballistic trajectories. The earliest ejecta fragments are derived from closer to the pre-impact surface, nearer the impact point, and are launched at the highest angles and velocities (Fig. 4). Conversely later ejecta fragments are generally derived from deeper in the target zone, further from the impact point, and are launched at lower angles and velocities. This results in a conical ejecta curtain that sweeps outward, first along with the transient crater margin as the crater grows and then over the pre-impact surface once the final transient crater size is reached. As the ejecta curtain moves outward the largest and slowest fragments are at its base; the fastest and smallest ones at its top. Close to the transient crater rim, fragments impact the surface at shallower angles, lower velocities and fragment sizes are larger on average than is the case for the distal edge of the ejecta deposit (solid arrow – schematic ejecta fragment velocity vectors; Fig. 4 insets). Furthermore, the impacting ejecta fragments cause ballistic erosion and sedimentation on the pre-impact surface that result in mixing pre-impact rock with ejected clasts. This process is more effective at greater distances because of the combined steeper impact angles and higher velocities of the ejecta fragments. The final dregs of energy are dissipated through outward, ground-hugging flow of the mixture of ejecta fragments and eroded bedrock/soil (open arrow – schematic ejecta deposit velocity vectors; Fig. 4 insets). The results are polymict breccias that have larger average clast sizes and lower matrix contents close to the tectonic rim of a large crater than at the distal edge of the ejecta deposit.

Detailed geological work on terrestrial craters, especially the extensive studies of the Bunte Breccia of the Ries Crater, offer specific examples of ejecta deposits that match the synopsis presented by Oberbeck (1975). The Ries Crater is of similar size to Endeavour crater, ~26 km diameter vs. ~22 km, is well-preserved and thus is an excellent terrestrial analog. Hörz et al. (1983) summarized petrologic work done on cores taken at numerous locations at different radial ranges through the Bunte Breccia and noted that there is no systematic vertical trend in the grain sizes of matrix components, nor is there a systematic vertical trend in clast size. The cores are chaotic mixtures of clasts and matrix throughout their length at any given location. Mader & Osinski (2018) similarly noted that the polymict breccias of the ~28 km diameter Mistastin Lake impact structure are poorly sorted, and Shoemaker (1963) described the ejecta surrounding the simple, bowl-shaped, 1.2 km diameter Meteor Crater as consisting of unsorted debris from <1 µm to >30 m in size. Hörz et al. (1983) identified a systematic trend of decreasing average clast size with radial distance from the Ries Crater rim, and Shoemaker (1963) reported decreasing block size and frequency with increasing radial range from Meteor Crater. Hörz et al. (1983) do not specifically state that the clast/matrix ratio decreases with radial range, but this can be inferred from the observations that: (i) the amount of primary crater material in the ejecta decreases with radial range; and (ii) the matrix is >95% derived from ballistic erosion of the local surface. Thus, the geological evidence demonstrates that ejecta deposits are unsorted, chaotic breccias at individual locations that show systematic variations with radial range.

The textures of the upper and lower Shoemaker formation do not match those expected of ejecta from a single impact. We have the best stratigraphic control on Cape Tribulation in the region of Marathon Valley where the two lower subunits occur as the valley floor and around the Spirit of Saint Louis feature, while upper Shoemaker rocks form the bounding ridges (Fig. 5) (Crumpler et al. 2020). In Perseverance Valley the upper Shoemaker similarly overlies the lower Shoemaker (Crumpler et al., 2020). A systematically finer-grained and clast-poor breccia at the base of a coarser-grained, clast-rich breccia is inconsistent with formation as an ejecta deposit from a single impact event. Rather, the textures of the lower Shoemaker subunits are consistent with formation from impacts that were more distant than that which produced the upper Shoemaker.

Hence, the geologic evidence supports an origin of the lower Shoemaker subunits on Cape Tribulation as distal ejecta from one or more impacts that predate Endeavour crater formation. The ridge-forming upper Shoemaker is an ejecta deposit from the Endeavour impact.

On Cape York, the Copper Cliff member of the Shoemaker formation overlies the pre-impact Matijevic formation and was mapped as a transitional breccia (Crumpler et al., 2015). The Copper Cliff member shows some textural and compositional similarities to the Matijevic formation (Crumpler et al., 2015; Mittlefehldt et al, 2018a), which we attributed to ballistic erosion and sedimentation processes as the Endeavour ejecta impacted the pre-impact surface (Mittlefehldt et al., 2018a). Although mapped as a transitional breccia, the Copper Cliff member is nevertheless a coarse breccia, the transitional character being imparted by inclusion of 1-2 mm spherules like those that are present in the Matijevic formation (Arvidson et al., 2014; Crumpler et al., 2015). Thus, the geological evidence does not support a pre-Endeavour origin for the Copper Cliff member, and all Shoemaker formation breccias on Cape York are Endeavour deposits.

4.2 Composition

We have done 138 analyses of Shoemaker formation rocks, including those discussed in Mittlefehldt et al. (2018a). Of these, 29 analyses were done on brushed targets, while 18 were on abraded targets. Some of the latter were cases where the abrasion was of low quality either because the activity faulted-out before completion, or topography of the surface was too great to result in a good abrasion circle at the planned depth. We consider that 13 analyses were on well-abraded targets. The 138 analyses represent 68 different rocks.

We have grouped the Shoemaker formation APXS targets according to geologic map units (Table 1) (Crumpler et al., 2015; 2020). The upper Shoemaker is undivided on Cape Tribulation; their geographic locations are noted on Table 1. A region mapped as Shoemaker lower-1 in Marathon Valley presented spectral evidence for the presence of Fe-Mg smectite in CRISM data (Fox et al., 2016), and four analyses from the region showing the strongest smectite signal are grouped separately. The Parral target is an ~5 cm rock fragment in a region of bedrock fragments on a dark sand substrate. The Zacatecas target from this region consists of mixed small bedrock fragments and dark sand. Both are listed with the upper Shoemaker rocks, but the latter might better be considered a composite soil (see Cabrol et al., 2014), and as discussed below, Parral is plausibly a cobble of lower Shoemaker.

Shoemaker formation rocks are essentially basaltic in composition and are like an estimated mean martian crust composition (Taylor & McLennan, 2009) (Fig. 6). Compositional variations within the suite generally are minor. Although compositions of the breccias from different locations and/or subunits substantially overlap for many elements, there are nevertheless systematic differences for some elements. Thus, on Cape York the average FeO content increases in the sequence Copper Cliff, Greeley Haven, Chester Lake members, and Shoemaker formation rocks have systematically higher Fe/Mn on Cape Tribulation than on Cape

York (Mittlefehldt et al., 2018a). Most of the compositional differences observed among subunits of the Shoemaker formation are in the volatile elements (S, Cl, Br; Fig. 7) that have been labile in the recent Martian environment (see Mittlefehldt et al., 2019b, and references therein), and in the mobile elements (P, Mn, Ni, Zn) that were mobilized by localized alteration events (Arvidson et al., 2016; Jolliff et al., 2019; Mittlefehldt et al., 2018a, 2019b). Table 2 gives the mean compositions plus uncertainties for subunits of the Shoemaker formation. For the three volatile elements the compositional data are averaged. For all other elements, the analyses are normalized to a SO_3-, Cl- and Br-free basis, and the normalized data are averaged. Excluding the volatile elements, the averages of different subunits for most of the elements overlap within uncertainty.

Because variations in composition within the Shoemaker formation are subtle, multivariate statistical techniques offer the best method for revealing compositional associations. We used Agglomerative Hierarchical Cluster Analysis (AHCA) to group observations (APXS targets) by similarities in variables (elements). We used Ward's minimum variance method for defining cluster linkages as it results in little within-cluster distance (synonymous with little internal dissimilarity). We used the Euclidean distance metric, and centroids were determined using the sum of distances. Element/Si mole ratios were used as variables to minimize problems associated with the closure restraint caused by forcing the APXS data to equal 100% (Chayes, 1971), and following Aitchison (1994), we modeled log(element/Si) rather than simple mole ratios. We included most of the rock types formed during or before the Endeavour impact: (i) Shoemaker formation targets; (ii) Matijevic formation matrix, spherule-rich and veneer targets; (iii) dark-rock boulder-float; (iv) blue-rock erratics; (v) basaltic outcrops from Perseverance Valley; (vi) basaltic rocks from the central fracture zone in Perseverance Valley; (vii) dark rocks from Wdowiak Ridge; (viii) boxwork vein targets from the Matijevic fm.; (ix) red-zone rocks from the Marathon Valley region; (x) pitted rocks from Perseverance Valley; and (xi) purple-rock erratics. The latter four groups are generally silica-rich and compositionally distinct from all other rocks along the rim (Fig. 6). We have excluded Matijevic formation, Shoemaker formation and red-zone targets that contained $CaSO_4$ veins from the modeling.

We included soil samples in our AHCA modeling to help evaluate the effects partial soil cover might have on the compositions of untreated surfaces. The types of soils modeled are: (i) dark sand composed of the fine-sand-sized particles that actively saltate in the current environment; (ii) bright soils composed of deposits of airfall dust; and (iii) composite soils composed of mixtures of fine to coarse materials (Cabrol et al., 2014). For the composite soils, we included only those lying on Shoemaker formation substrate as judged by geological maps. For dark-sand and bright-soil targets, we used those from the entire rover traverse. This resulted in 237 analyses being modeled. Table 3 gives the element/Si mole ratios for analyses used in the AHCA modeling.

We excluded the volatile elements S, Cl, and Br from the analyses because, to the extent possible, we wish to focus on the silicate compositions of the rocks. Sulfur and Cl are variable within the suite and are at wt% concentration levels (Table 1; Fig. 7). This can cause targets with very similar silicate compositions to occupy dissimilar clusters if S/Si and Cl/Si are included in the modeling. We included the mobile elements P, Mn, Ni and Zn in the first model run to help evaluate which targets might contain subtle signatures of alteration processes and ran a second model excluding these elements to evaluate the impact of alteration on the rocks.

We forced the calculation to return 20 clusters in order to obtain finer granularity on the results, and merge clusters at higher levels by inspection of the dendrogram and cluster memberships to yield geologically interpretable results. A cluster hierarchy matrix summarizing the distributions of different rock types in the clusters for the first model run is given in Table 4a; the dendrogram is given in Fig. 8. The cluster hierarchy matrix for the second model run is given in Table 4b. The observations axis shows individual analyses and linkages between them grouped in color-coded clusters. The inset shows an expanded view of 16-member cluster 1. Individual observations are joined with other observations (or linked observations) at distances (degrees of dissimilarity) indicated by the cross linkages. The labeled cluster members are the two most similar members of this cluster (linked at the smallest distance). These are two analyses of the abraded Azilda2 target in the Matijevic formation, one done before and one after the abrasion hole was brushed to clear out debris. Cluster 1 is fully defined when all observations are finally joined at the greatest distance (highest degree of dissimilarity) – the linkage at a distance of ~1.11. This level of dissimilarity for cluster 1 was set by our arbitrary requirement that the analysis return 20 clusters.

We discuss the AHCA models at the most dissimilar level and go deeper as needed. Four major clusters are evident in Fig. 8: A, including clusters 1-7 (72 analyses); B, containing clusters 8-11 (40 analyses); C, consisting of clusters 12-15 (91 analyses); and D, composed of clusters 16-20 (34 analyses). Major cluster D links with ABC at a distance of 27.7, more than twice the distance of the A-BC linkage (12.3). Major cluster D includes most analyses (63%) of the four silica-rich lithic types shown in Fig. 6: silica-rich boxwork veins from the Matijevic formation; the red-zone group; pitted rocks from Perseverance Valley; purple-rock erratics. These will be discussed in section 4.3. All analyses of erratic rock Marquette Island are in cluster 15 of major cluster C; this rock is discussed in section 5. For the second AHCA model run, we similarly group the 20 clusters into four major clusters and refer to them as I through IV (Table 4b) for clarity in the discussion. The distance of the last linkage separating major cluster IV from the other is ~12.4, less than half the distance of the ABC-D linkage in the first model run (Fig. 8), which indicates that the mobile elements contribute importantly to the compositional variability.

All soil targets in the first model occupy either cluster 6 or 14 (Table 4a) and most of the soil targets in the second model run are in cluster 11 (Table 4b). All rock targets in these clusters are untreated. Because of this, we consider their compositions to be possibly compromised and they are discounted in the discussion that follows. Six untreated rocks are clustered with soils in both model runs and are especially suspect.

For the first model run, analyses contained in major cluster A include 65% of the Endeavour crater Shoemaker breccias, but none of the pre-Endeavour crater Shoemaker breccias. It includes 57% of the Matijevic formation rocks (excluding the boxwork veins), 20% of the dark basaltic rocks and 18% of the erratic rocks (Table 4a). Analyses contained in major cluster B include 6% of the Endeavour crater Shoemaker formation breccias, 33% of the pre-Endeavour

Shoemaker breccias, the remainder of the Matijevic formation rocks, and none of the dark basaltic or erratic rocks. Major cluster C includes 27% of the Endeavour crater Shoemaker breccias, 64% of the pre-Endeavour Shoemaker breccias, none of the Matijevic formation analyses, 13% of the dark basaltic rocks and 41% of the erratic rocks. Major cluster D includes only 3% of the pre-Endeavour Shoemaker breccias, none of the Matijevic formation analyses, 67% of the dark basaltic rocks and 41% of the erratic rocks. The sole 2 Endeavour crater Shoemaker breccia analysis in major cluster D is the anomalous target Sledge Island1.

There is a substantially different distribution of Endeavour and pre-Endeavour Shoemaker formation breccias between the major clusters; most Endeavour Shoemaker breccias are in major cluster A while most pre-Endeavour Shoemaker breccias are in major cluster C. There is a geographic distinction for clustering amongst Endeavour crater Shoemaker breccias: 97% of those from Cape York are in major cluster A while 68% of those from Cape Tribulation are in major cluster C. This latter fact suggests either that there was a different lithic mixture in the ejecta deposited on Cape York than on Cape Tribulation or that alteration processes on the two rim segments were different. The latter is supported by the second AHCA model run that excluded the more mobile elements. In this model, Endeavour crater Shoemaker breccias from Capes York and Tribulation are all dominantly (86-89%) in major cluster II (Table 4b). We conclude that post-Endeavour alteration processes in the region of Cape York were different in degree or style than those in the neighborhood of Cape Tribulation. We presaged this possibility in Mittlefehldt et al. (2018a) where we noted that there was a systematic difference in Fe/Mn ratios of Shoemaker formation breccias between those on Cape York and on Murray Ridge from Cape Tribulation, and we noted than Mn was mobile during alteration.

When the mobile elements are excluded from the model, pre-Endeavour Shoemaker breccias are mostly in major cluster II with the Endeavour crater Shoemaker breccias (Table 4b). However, the pre-Endeavour Matijevic formation rocks are overwhelmingly in major cluster I. Together, these results suggest that the Shoemaker breccias deposited by the Endeavour impact are mostly composed of lithic materials like the lower Shoemaker, and rocks like the Matijevic formation make up a minor proportion.

There are some textural similarities between the Copper Cliff member of the upper Shoemaker and the Matijevic formation that are not observed for other members of the Shoemaker formation on Cape York (Crumpler et al., 2015). The AHCA modeling we did previously indicated a compositional connection between the Copper Cliff member and the Matijevic formation that was not observed for other members of the Shoemaker formation (Mittlefehldt et al., 2018a). We interpreted the compositional and textural evidence to establish that the Copper Cliff member was formed by ballistic erosion and sedimentation processes (Oberbeck, 1975) as Endeavour ejecta impacted and mixed with rocks on the pre-Endeavour (locally Matijevic formation) surface (Mittlefehldt et al., 2018a). Here we reexamine the possible connection between the Copper Cliff member and the Matijevic formation using our new AHCA results on a larger data set. Our previous AHCA modeling using a different linkage method and simple element/Si mole ratios, not log ratios. Use of the log ratios here will make the results more robust against the closure problem (Aitchison, 1994).

The compositional connection between the Copper Cliff member and the Matijevic formation is generally supported by our present modeling. In the first model which excludes the volatile elements (S, Cl and Br), analyses of the Matijevic matrix (clastic rocks with few spherules) and two analyses of veneer on the Matijevic surface are in cluster 1 as are 63% of the Copper Cliff analyses (Table 4a). No other Shoemaker formation analyses are in cluster 1. The remainder of the Copper Cliff analyses are in cluster 2, along with the other analyses of the veneer. Two upper Shoemaker formation analyses are in cluster 2; anomalous rock Sledge Island1 and Parral, which we argued above is plausibly lower Shoemaker. Analyses of the spherule-rich targets in the Matijevic formation are in cluster 9, part of major cluster B, and thus show no close compositional connection to the Copper Cliff member (or the other Matijevic formation targets for that matter). When the mobile elements P, Mn, Ni and Zn are excluded from the modeling, all matrix and spherule-rich Matijevic targets and three of five of the veneer targets are in clusters 1 and 2, as are 63% of the Copper Cliff member analyses, but only two of upper Shoemaker targets. The new AHCA modeling still indicates a compositional connection between the Copper Cliff member and the underlying Matijevic formation and we conclude that formation by ballistic erosion and sedimentation processes (Oberbeck, 1975) remains a good model for understanding the Copper Cliff member.

We grouped four analyses of two targets (York and Jean Baptiste Deschamps) separately for the purposes of AHCA modeling, and the results show that they are compositionally distinctive. The western end of Marathon Valley is mapped as containing Fe-Mg smectite based on analysis of multiple CRISM images of the region, with a (Fe,Mg)-OH 2.29 μm band depth comparable to those from Mawrth Vallis (Fox et al., 2016). This signal encompasses most of the western valley floor, including most of the lower-1 and lower-2 APXS targets. During operations, a lower-1 outcrop containing the York and Jean Baptiste Deschamps targets was modeled to be a locus of the strongest smectite signal and these two targets are separated as representing a “smectite region” (Table 1). The analyses of these targets are clearly distinguishable from those of other lower-1 targets in the AHCA modeling. The smectite region analyses are the sole members of cluster 9 in major cluster B, while all other analyses of lower-1 targets are in major cluster C (Table 4a) Thus, the smectite region analyses are separated from the other lower-1 analyses at the B-C separation at the third most dissimilar linkage (Fig. 8).

The smectite region rocks are less distinct from other lower-1 targets when the mobile elements are excluded from the AHCA modeling. In this case, the smectite region analyses still occur in a single cluster, but that cluster does include two other lower-1 analyses (Table 4b). Furthermore, 89% of lower-1 analyses are in major cluster II along with the smectite region analyses. This indicates that the smectite region rocks are not especially different in lithic components, but rather, their distinction is more closely tied to the alteration that engendered smectite formation.

4.3 Si-rich Lithic Types and pre-Endeavour Alteration

There are four silica-rich lithic types along Endeavour crater rim: (i) the Lihir/Espérance boxwork veins that crosscut the Matijevic formation on Cape York (Arvidson et al., 2014; Clark et al., 2016; Crumpler et al., 2015); (ii) the red-zone group from the Marathon Valley region; (iii) purple erratic blocks first encountered on a ridge overlooking Marathon Valley; and (iv) pitted rocks from Perseverance Valley. These four rock types share the common characteristic of having higher SiO_2 and lower FeO than Shoemaker or Matijevic formation rocks (Fig. 6a), but for other elements, they can overlap the ranges for these formations and/or show distinct elemental trends between them (Fig. 6). All the boxwork vein analyses are in major cluster B, while all purple and pitted rock targets are in major cluster D (Table 4a; Fig. 8). The red-zone group analyses are distributed amongst major clusters A (27%), B (9%) and D (64%) (Table 4a). When the mobile elements are excluded from the AHCA modeling, major cluster IV contains only silica-rich rocks, including all boxwork vein, purple rock and pitted rock, and 82% of the red-zone group targets (Table 4b).

4.3.1 Boxwork Veins in the Matijevic Formation

The two abraded interiors of the boxwork veins have the highest SiO_2 and Al_2O_3 (Fig. 6c), the lowest FeO, MgO and CaO (Figs. 6a, b, d) and show the cleanest compositional signal of the vein material (Clark et al., 2016). These two analyses have the highest SiO_2 and lowest FeO and CaO of any target analyzed on Meridiani Planum. The boxwork vein compositions are consistent with montmorillonite plus silica having been the dominant phases in the veins (Arvidson et al., 2014; Clark et al., 2016). These veins were formed from hydrothermal solutions that were circumneutral to mildly alkaline in pH (Clark et al., 2016; Mittlefehldt et al., 2018a).

4.3.2 Red-zone Group in Marathon Valley

Unique to the Marathon Valley region (online supplement Fig. L06) are prominent curvilinear features crosscutting outcrop blocks containing rock with distinctive reddish color in Pancam false-color images (Fig. 10a) which we informally call “red zones.” At the head of Marathon Valley is a shallow, ovoid depression ~25×35 m in size – Spirit of Saint Louis (Fig. 1d) – which is partly bounded by a ~10-20 cm wide zone containing red-zone rocks crosscutting Shoemaker lower-2. Some of the outcrop blocks near Spirit of Saint Louis also exhibit compositional similarities to the red zones. Red zones were found within Marathon Valley proper crosscutting both lower-1 and lower-2 subunits. After leaving Marathon Valley on a feature named Spirit Mound (online supplement Fig. L08), we discovered an outcrop of lower-1 subunit bedrock cut by a composite silica-$CaSO_4$ vein-like structure (Fig. 15b) which shows geochemical similarities to red-zone rocks. All these targets are referred to as the red-zone group. Red-zone features were not observed outside the region of Marathon Valley and immediate surroundings, nor in the upper Shoemaker subunit.

Excluding the vein on Spirit Mound, rocks in the cores of red zones consist of discontinuous cm-sized knobs of rock with a hackly, cemented appearance (Fig. 10c). Many of them appear indurated, with clasts and matrix only poorly distinguished. They are distinct from rocks on either side of the red zone which are texturally typical of the Shoemaker lower-1 or lower-2 breccias which they crosscut (Figs. 10b, d).

Red zone rocks have unique compositional characteristics (Fig. 6). Most analyses occupy cluster 18 within major cluster D (Table 4a). The only other analyses in cluster 18 are two on lower-2 target Muffler II. The two red-zone analyses in cluster 3 are targets on Gasconade3 and 4, a red-zone group vein on Spirit Mound. The other two outliers are Thermopylae2 and Private Pierre Cruzatte, which have higher Ni contents (as do Gasconade3 and 4) than the other red-zone group analyses. When the mobile elements are removed from the AHCA analyses, Thermopylae2 and Private Pierre Cruzatte cluster with the other red-zone group analyses, while Gasconade3 and 4 remain separated at the cluster level (Table 4b). Like the boxwork veins, the red-zone group has higher SiO_2 and lower FeO contents compared to Shoemaker fm. breccias (Fig. 6a). Furthermore, red-zone-group compositions follow the MgO-SiO_2 and CaO-SiO_2 trends of the boxwork veins (Figs. 6b, d). One distinction between these two rock types is that the boxwork veins show strong enrichments in Al_2O_3, while the red-zone rocks show more modest enrichments, resulting in distinct Al_2O_3-SiO_2 trends (Fig. 6c). The red-zone group has Al_2O_3, TiO_2 and Cr_2O_3 contents within ranges of Shoemaker lower-1 and lower-2 breccias (Figs. 6c, e, f).

For the red zone around Spirit of Saint Louis we did three analyses each of red-zone rocks and the host rock on either side of the red zone (Fig. 10a). Compared only to these adjacent breccias, the red-zone rocks have enrichments in Al, Si, Ti, Cr and Ge (Fig. 11a). Potassium contents are also higher than those of the nearby breccias but overlap the uncertainty envelope of the mean host rock. Phosphorus, Ca and Zn overlap the composition of the mean host rock, while the other elements are depleted relative to it. Considering only the red-zone target with the highest SiO_2 content, Private William Bratton (Fig. 11a inset), Al, Si and Cr are well-resolved from the host rock, while the uncertainties on K and Ti overlap the uncertainty envelope on the host rock composition. Some bedrock blocks near the Spirit of Saint Louis feature have higher Al_2O_3 and SiO_2 contents indicating red-zone-style alteration extended beyond the narrow, visually defined red zones. Rocks on either side of the red zone and patches within it have Pancam spectra which more closely resemble that of red hematite, indicating the presence of crystalline ferric oxides within these rocks (Farrand et al., 2016).

Some rocks from the Spirit of Saint Louis region have elevated Ge contents. The highest Ge contents are observed for red-zone-group rocks (Table 5). Germanium concentrations for Private William Bratton from the red zone proper (853 µg/g) and Thermopylae2 from a nearby outcrop block that has red-zone-group compositional characteristics (855 µg/g) are the highest concentrations measured on Mars (cf., ~650 µg/g in the Garden City vein cluster crosscutting Murray formation sandstones in Gale crater; Berger et al., 2017).

Germanium is mobilized in hydrothermal fluids, and hydrothermally altered seafloor basalts on Earth show modest enrichments of a few µg/g in Ge (e.g., Escoube et al., 2015). In terrestrial hydrothermal deposits, Ge substitutes in Fe-oxyhydroxides, sulfides or sulfosalts (Bernstein, 1985). There is no correlation between Ge and either Fe or S for the rocks around Spirit of Saint Louis, indicating that Fe-oxyhydroxides or S-bearing phases are not significant hosts for Ge. At Gale crater, measurements made by the Curiosity rover APXS instrument show that there is a broad positive correlation between Zn and Ge (Berger et al., 2017). In the Spirit of Saint Louis region Zn and Ge are anti-correlated, indicating a different mechanism for Ge enrichment than pertained at Gale crater.

Germanium concentrations in the region of Spirit of Saint Louis are roughly correlated with Al_2O_3 and SiO_2 (Fig. 11b). Tetravalent Ge and Si have similar chemical properties, and Ge substitutes for Si in minerals (e.g., see He et al., 2019). Hence, Ge is most likely substituted in the silica phase in the red zones. The highest Ge contents are ~20× the general background values (Fig. 11a) indicating the Ge enrichment could not have resulted from passive concentration as more soluble elements were leached away; Ge must have precipitated from solutions. This in turn suggests that at least a portion of the silica is a precipitate. Alumina, Ti and Cr are also concentrated in the red-zone rocks, and these elements can be conserved during hydrothermal alteration. A possible scenario for the red-zone-group rocks in the vicinity of Spirit of Saint Louis is fluxing of hydrothermal fluids through fractures and nearby porous bedrock in the region which resulted in localized alteration and leaching of the more soluble elements at high water/rock, followed by precipitation of Ge-bearing silica. Hydrothermal solutions in equilibrium with Ge-bearing silicates have higher Si and Ge concentrations and Ge/Si ratios at higher temperatures (Pokrovski & Schott, 1998). Thus, simple cooling of solutions during waning stages of hydrothermal activity could result in precipitation of Ge-rich silica.

The rocks in the Spirit of Saint Louis region show enrichments in Ge, but other bedrock and red-zone-group targets from the Marathon Valley region do not have detectable Ge (detection limit roughly 30 µg/g, but dependent on target composition and analytical conditions) (Fig. 11b). This might suggest that there were differences in fluid compositions and/or properties (temperature, pH, etc.) at this location. However, red-zone rocks with identical enrichments in Al_2O_3 and SiO_2 and depletions in FeO have Ge contents that differ by a factor 30 or more (Fig. 11b). Any differences in fluid compositions and/or properties would have to be such that the major elements were not affected. For example, fluid composition could have been affected by earlier mineral precipitation, and in terrestrial systems, the Ge/Si of fluids can be increased by this process (Escoube et al., 2015; Mortlock et al., 1993). This is unlikely to explain high- and low-Ge red-zone rocks with similar SiO_2 contents as early precipitation of silica is commonly invoked to explain such fluids (Escoube et al., 2015; Mortlock et al., 1993). An alternate hypothesis is that the bedrock below Spirit of Saint Louis is atypically rich in Ge, but this merely pushes the cause of Ge enrichment beyond our ability to test. With the observations at hand, we cannot come to firm conclusions regarding the difference in Ge geochemistry in the lower Shoemaker formation units in the Marathon Valley region.

4.3.3 Purple Rocks in the Marathon Valley Region

Purple rocks are erratic boulders scattered on a ridge overlooking the northeast side of Marathon Valley and on the valley floor at the base of the ridge. They are identified by unique purplish color in Pancam false-color composites (753, 535 and 432 nm) and a fine-grained, almost aphanitic texture. The five analyses of this lithic type represent three different rocks. Their silica contents are only marginally greater than those of Shoemaker formation breccias, but their Al_2O_3 contents are much higher (Fig. 6c); two analyses of target Sergeant Nathaniel Pryor are the highest Al_2O_3 contents measured on Meridiani Planum. Compared to the boxwork veins and red-zone group, the purple rocks have very low MgO and Cr_2O_3, Ni below the detection limit, and widely varying TiO_2 (Table 1, Figs, 6b, e, f). These elemental distributions are very different from the alteration signatures exhibited by the boxwork veins and red-zone group.

The silica- and alumina-rich compositions of the purple rocks could represent evolved igneous compositions, but the case is not clear. On a total alkalis-silica diagram often used to classify martian igneous rocks, they fall in the field of basaltic andesite. Igneous fractionation from basaltic to intermediate compositions show generally increasing Al_2O_3 with SiO_2, and decreasing MgO, CaO, Cr_2O_3 and Ni (for example, the tholeiite to icelandite series at the Torfajökull volcanic complex, Macdonald et al., 1990). Dark-rock boulder-float and rocks from Wdowiak Ridge are potential pre-Endeavour basaltic rocks (Mittlefehldt et al., 2018a), and the blue rocks are basaltic in composition. Elemental trends between these rock types and the purple rocks (Fig. 6) are consistent with an igneous fractionation sequence. However, the wide range in TiO_2 contents with little change in MgO or Cr_2O_3 is inconsistent with simple igneous fractionation; a strong anticorrelation would be expected.

4.3.4 Pitted Rocks in Perseverance Valley

We encountered deeply pitted rocks in a linear outcrop in the central portion of Perseverance Valley. These rocks, referred to here as pitted rocks, are thought to occupy a fracture zone, possibly a fault trace, within the valley (Crumpler et al., 2020). They have a fine-grained granular texture, lack visible clasts and contain mm-sized pits of uncertain origin (Tait et al., 2019). Dark, fine-grained granular material is present within some pits which appears to be dark sand, but some pits contain orangish-red (in false color) fine-grained fillings texturally reminiscent of zeolites filling vesicles in altered basalt. These fillings have deep 535 nm absorption bands indicative of abundant nanophase ferric oxides. Other pits have light-toned rims. Light-toned coatings or rinds on parts of some pitted rocks give spectral evidence of alteration (Farrand et al., 2019; Tait et al., 2019).

The five analyses of pitted rocks represent two different rocks and show varied compositions. The three analyses with the lowest SiO_2 (targets Allende and Nazas) are in cluster 19 along with the purple rocks (Table 4a). The other pitted rock analyses (target Tomé) are in cluster 20. Target Nazas was centered on a pit filled with fine-grained, acicular crystals to capture the composition of alteration material and yielded a silica content intermediate between Allende and Tomé. The Tomé analyses have the highest SiO_2 contents of any target from Marathon and Perseverance Valleys and rival the highest SiO_2 contents measured for the boxwork veins in the Matijevic formation (Fig. 6). Unlike the boxwork veins, the pitted rocks do not show a positive correlation between Al_2O_3 and SiO_2 (Fig. 6c).

The similarity between Allende and the purple rocks suggest that this pitted rock could be an evolved magmatic composition. The low MgO, FeO and Cr_2O_3 contents (Figs. 6a, b, f) and Ni below detection all support this. However, the morphology and location of the pitted rocks as a linear feature in a probable fault trace are not that of volcanic unit. The formation mechanism for these rocks is uncertain (see Tait et al., 2019). They could be pseudotachylyte formed in the fracture either by impact or tectonic processes (Reimold, 1995). Pseudotachylite is a cataclastic rock but the pitted rocks to not appear to be. The pitted rocks are juxtaposed with dark basaltic rock in the fracture zone (Crumpler et al., 2020) and clasts of dark basalt in the dark-melt matrix might have been difficult to distinguish in the rover images. The silica-rich Tomé targets cannot be more evolved magmatic compositions than Allende because there is no substantial depletion in them of MgO, FeO and Cr_2O_3 compared to Allende. An alternative hypothesis is that Tomé is an altered composition of rock that might initially have been like Allende.

4.3.5 Evaluation of Alteration in Si-rich Rocks

Chemical alteration diagrams are used to document compositional changes in terrestrial rocks caused by alteration and weathering. Figure 12a is a portion of an Al_2O_3, ($CaO^*+Na_2O+K_2O$), and (FeO_T+MgO) (A-CNK-FM) diagram (Nesbit & Wilson, 1992), and Fig. 12b is a portion of a modified weathering intensity scale (WIS) diagram (Meunier et al., 2013). These diagrams were devised to evaluate compositional changes occurring in rock during soil formation. In the A-CNK-FM diagram, CaO* is measured CaO minus that contained in apatite and carbonate (Nesbit & Wilson, 1992). We assumed all P_2O_5 is in apatite and had to ignore calcite because CO_2 is not determined by the APXS. In the modified WIS diagram we treat all iron as FeO because we have no measure of the ferric/ferrous ratio for the rocks. In Fig. 12a, pristine basaltic to intermediate igneous rocks will plot between the feldspar-olivine join and the field for pyroxenes, as is observed for martian mafic rocks (blue rocks from the Endeavour crater rim, and Adirondack-, Backstay- and Algonquin-class rocks from Gusev crater). On both diagrams, magmatic differentiation will cause rock compositions to move from the field for mafic rocks in the general direction towards the purple rocks. This is illustrated by a suite of tholeiites through icelandites from the Torfajökull volcanic complex (Macdonald et al., 1990). Low-temperature alteration on Earth (pedogenesis) of a range of primary rocks drives compositions into the Al_2O_3 side of Fig. 12a and away from the Na+K+2Ca apex of Fig. 12b, as illustrated by alteration for Monaro basalts from New South Wales, Australia (curved arrows) (Eggleton et al., 1987). On Mars, alteration under low water/rock, acidic conditions in which olivine is preferentially dissolved with the R^{2+} cations leached away would change pristine martian basalt compositions directly away from the $MgO+FeO_T$ (+MnO) apexes (blue arrows) (Hurowitz & McLennan, 2007).

The four silica-rich rock types from the Endeavour crater rim show differing trends on the alteration diagrams resulting in differing interpretations. The clearest signature for alteration is shown by the boxwork veins crosscutting the Matijevic formation. Compositions of the two abraded targets fall near or within the field of terrestrial montmorillonites (Fig. 12) (Wolters et al., 2009), consistent with the interpretation of Clark et al. (2016). Clark et al. (2016) calculated a pure vein composition for the Espérance vein by removing the instrument response to a small amount of veneer material that was in the APXS field of view. The resulting composition plots well within the fields for montmorillonite in Fig. 12. these analyses by removing aFive analyses by sister rover Spirit of rock Independence from Gusev crater are shown for comparison as this rock is thought to contain an alteration component close in composition to montmorillonite (Clark et al, 2007). The rock shows clear evidence for alteration, but the signature for montmorillonite is not as clearly expressed as for the boxwork veins. The red-zone group shows less dramatic evidence for alteration on these diagrams, however, tie lines joining the host rock composition for Private William Bratton with that red-zone target (white arrows) diverge from vectors expected for alteration under low water/rock, acidic conditions (blue dashed arrows). This, plus the arguments given in section 4.3.2 for coprecipitation of Si and Ge, indicates that compositions of red-zone group rocks are not derived by simple passive enrichment as ferromagnesian cations released by olivine dissolution are leached away.

The purple rocks show conflicting evidence regarding whether they are altered compositions and if so, how they might have been altered. These rocks have compositions broadly consistent with their being intermediate melts from a basalt fractionation sequence, especially the two analyses of Bashful II which have the lowest Al_2O_3 contents (Fig. 6c). The two purple rock analyses with highest Al_2O_3 (Sergeant Nathaniel Pryor) have CIPW norms that are marginally corundum normative (one is; one is not). Corundum-normative compositions indicate rock compositions that have been significantly altered from those of pristine magmatic rocks (see discussions in Ming et al., 2006; Mittlefehldt et al., 2019b). The textures of purple rocks are consistent with a fine-grained, quenched melt. Taken together, the evidence suggests the purple rocks are slightly altered intermediate magmatic rocks. However, we cannot rule out an origin as fragments of impact melt of slightly altered target rock with a mixed composition like that of intermediate magmatic rocks. The purple rocks do not contain clasts which commonly occur in impact melts, but this does not preclude an impact-melt origin. Observations of flow features in impact-melt deposits in lunar craters indicate relatively fluid flow for extended periods after the impact event for some (Bray et al., 2010). The morphology of some impact-melt deposits indicates low viscosities, and therefore, low clast contents (Bray et al., 2010; Stopar et al., 2014). Thus, an origin as fragments of an old ponded impact-melt sheet remains viable for the purple rocks.

The pitted rock Allende mimics the purple rocks on the alteration diagrams, while the Nazas and two Tomé targets show clear evidence of the effects of alteration. The Allende analyses are fully consistent with a pristine intermediate magmatic composition. It is not corundum normative, and, ignoring the ubiquitous SO_3, Cl and Br, shows no compositional evidence for alteration. As is the case for the purple rocks, an impact melt origin is viable, specifically as pseudotacylite. The Nazas analysis was targeted on a pit largely filled with reddish orange (in false color) acicular alteration material (Fig. 13), and its composition has excess Al and a deficit in Na+K+2Ca compared to the Bashful II analyses. These characteristics and the texture are consistent with formation as a pit filling formed through alteration under relatively high water/rock. Tomé is marginally on the Al-rich side of the feldspar-olivine join in Fig. 12a and plots with Nazas on Fig. 12b, indicating an altered composition, consistent with Pancam spectral evidence (Farrand et al., 2019; Tait et al., 2019).

4.4 Sulfate-rich Rocks and Post-Endeavour Alteration

We have previously documented episodes of sulfate-dominated alteration at several locations along the Endeavour crater rim hosted in the Matijevic, Shoemaker (upper) and Grasberg formations (Arvidson et al., 2014, 2016; Crumpler et al., 2015; Mittlefehldt et al., 2018a; Squyres et al., 2012). Except for alteration in the Cook Haven region (Arvidson et al., 2016), the sulfates are dominantly $CaSO_4$ in crosscutting veins (Fig. 14a). Relatively coarse

$CaSO_4$ veins occur in upper Shoemaker outcrops on Cape Tribulation (Mittlefehldt et al., 2018a) and in the Grasberg formation which drapes over the lower reaches of the upper Shoemaker (Crumpler et al., 2015; Squyres et al., 2012). These observations document a period of $CaSO_4$ precipitation from dilute solutions after formation of Endeavour crater and likely after deposition of at least a portion of the Burns formation of sulfate-rich sandstones (Mittlefehldt et al., 2018a). The thin $CaSO_4$ veins crosscutting the Matijevic formation (Arvidson et al., 2014) represent an earlier, pre-Endeavour-impact period of sulfate precipitation, based on superposition relationships. The veins are truncated by alteration veneers that were formed on an eroded surface (unconformity) between the Matijevic and Shoemaker formations (Mittlefehldt et al., 2018a).

In the Cook Haven region, sulfates were found as coatings on rock fragments overturned by Opportunity's wheels; these are dominated by Mg-sulfates (Arvidson et al., 2016). Cook Haven lies in a gentle depression on Murray Ridge where highly fractured outcrops are exposed. The region is thought to be within a fracture zone transecting the Endeavour crater rim (Arvidson et al., 2016). The rock coatings on Pinnacle Island and Stuart Island and the disturbed soil Anchor Point show positive correlations between Mg and S, but not Ca and S (Figs. 14a, b). These rock coatings include the highest measured SO_3 contents on Meridiani Planum. They are also rich in MnO (Fig. 14c); Pinnacle and Stuart Islands have the highest MnO contents measured on Meridiani Planum and Ni is positively correlated with MnO (Arvidson et al., 2016). The high Mn contents are identified from Pancam 13-filter spectra as arising from one or more Mn oxides (Arvidson et al., 2016). Further, the rock coatings on Pinnacle Island have high P_2O_5 contents; the second and third highest on Meridiani Planum (Arvidson et al., 2016). The compositions and mineralogies of the coatings reflect precipitation of phases from solutions formed through alteration of basaltic composition protoliths (Arvidson et al., 2016).

A S-rich region associated with fractures through Shoemaker lower-1 bedrock was found in Marathon Valley (Fig. 15a). The bedrock includes a red-zone-group vein adjacent to the S-rich region. Regolith in the fractures shows some compositional similarities to the altered rocks and soils at Cook Haven. The two soil targets E Cann and Joseph Field show a positive correlation between Mg and S, but not between Ca and S (Fig. 14a, b), but unlike the Cook Haven rock coatings, E Cann and Joseph Field do not show elevated MnO (Fig. 14c) or P_2O_5. The high MnO content of rock coatings on Pinnacle and Stuart Islands is considered to have been caused by late oxidation of solutions prompting precipitation of Mn oxides (Arvidson et al., 2016). The compositional signature of E Cann and Joseph Field is consistent with a similar formation mechanism as that of the Cook Haven rock coating, minus the oxidation/precipitation of Mn oxides and P enrichment.

The similar colored targets in the vicinity of E Cann and Joseph Field had Pancam 13f spectra with a shallow absorption band centered between 803 and 864 nm (the Pancam R3 and R4 bands). This absorption was comparable, albeit weaker in depth, and with a steeper blue to red slope and concomitant diminishment of reflectance in the 673 nm (L3) band, as those observed in spectra associated with light-toned, disturbed, sulfur-rich soils observed by the Spirit rover in the Columbia Hills of Gusev crater (Fig. 16) (Farrand et al., 2016; Johnson et al., 2007).

Opportunity traveled eastward after leaving Marathon Valley towards the interior of Endeavour crater to investigate the small knob Spirit Mound which we thought might expose Matijevic formation outcrops. Mapping showed that bedrock at Spirit Mound was Shoemaker lower-1 (Crumpler et al., 2020) that included a bright-vein-complex named Gasconade (Fig. 15b). We did two APXS measurements each of the vein interior and edge (Fig. 15c). The edge samples, Gasconade3 and Gasconade4, clustered with the red-zone group in our early AHCA modeling and we include them with this group here. However, although these targets are Si-rich like the red-zone group, they are Al-poor compared to that group (Fig. 6c). The limited data on hand do not allow us to determine the mechanism of SiO_2 enrichment. Because the Si-rich sample is hosted in pre-Endeavour bedrock and has compositional signatures most similar to other altered rocks that are pre-Endeavour, we interpret this as a pre-Endeavour alteration. The interior samples are sulfate-rich, and tie lines between the silica-rich and sulfate-rich samples indicate $CaSO_4$ dominates (Fig. 14 a, b). As discussed above, $CaSO_4$ veins are common in post-Endeavour rocks suggesting that Gasconade and 2 might have been precipitated much later from solutions following an older vein system. However, $CaSO_4$ veins are also present in the Matijevic formation and are pre-Endeavour. Thus, the timing of formation of the Gasconade $CaSO_4$ veins relative to the Endeavour impact is indeterminant.

The results of compositional measurements of alteration materials along the crater rim demonstrate that alteration in the pre-Endeavour basement commonly resulted in precipitation of silica ± alumina with some $CaSO_4$ precipitation, and that this reflects alteration by circumneutral solutions (Clark et al., 2016). In contrast, post-Endeavour alteration was dominantly a sulfate-forming process. We suggest that the Mg-sulfate alteration observed at Cook Haven and Marathon Valley likely was a response to hydrothermal solutions flowing through fractures in the bedrock closely associated in time with the impact event. The crosscutting $CaSO_4$ veins in upper Shoemaker and Grasberg formations represent a much later episode of sulfate precipitation that occurred after Burns formation sulfate-sands were being deposited at Meridiani Planum (Mittlefehldt et al., 2018a).

4.5 Surface vs. Interior Composition

We have investigated five Shoemaker formation targets where we analyzed untreated, brushed and abraded targets to get information on compositions of the interiors, possible coatings, and differences in composition between interiors and brushed surfaces to evaluate possible surface-alteration zones: Private Robert Frazer; Pierre Pinaut; Private John Potts; Aguas Calientes; and Salisbury. Private Robert Frazer is from an outcrop situated on the northern side of Marathon Valley, east of a short ridge that forms part of the northern wall of the valley, while Pierre Pinaut is from an outcrop near the southern margin of Marathon Valley, approximately 50 m southwest of Private Robert Frazer. These targets are on outcrops of Shoemaker lower-1. Private John Potts is from a Shoemaker lower-2 outcrop located along the southern margin of Marathon Valley near Opportunity's egress point from the valley. It is about 60 m due east of Private Robert Frazer and ~90 m northeast of Pierre Pinaut. Aguas Calientes is from a lower Shoemaker outcrop block situated in the middle of Perseverance Valley roughly at the furthest point into the valley explored by Opportunity. Salisbury is from the Chester Lake member of the

Shoemaker formation located on the southeastern end of Cape York. This outcrop was discussed by Squyres et al. (2012) where it was referred to as Chester Lake.

We normalized interior compositions to the cleanest brushed surface compositions for each target, and to the extent possible, compare brushed with interior compositions taken at identical APXS coordinates. Two abrasion activities were done on each of the rocks. We discuss the results for each abrasion for Private John Potts, Aguas Calientes and Salisbury. For Private Robert Frazer, the initial grind resulted in a partial abrasion circle, and APXS analyses on the brushed surface were not co-located with the post-abrasion spot. The analysis after the initial abrasion is not discussed. For Pierre Pinaut, the first grinding operation on did not significantly abrade the surface. The APXS results after the first abrasion were considered the cleanest surface analysis and used for normalizations for this target. The analysis campaigns resulted in eight interior-exterior pairs for the various lower Shoemaker targets, and two for Salisbury.

A qualitative synopsis of the interior/exterior results is given in Table 6 where a 3σ uncertainty level is used to identify elements in interior compositions that are greater than, less than, or equal to the brushed surface analyses. Silica is the most abundant element in Shoemaker formation breccias, and variations in Si within the suite are relatively small. At the 3σ level, Si mass-ratios are greater in the interiors than the exteriors in about half the targets, and equal to them in the other half. The closure restraint on major element analyses can cause false correlations (Chayes, 1971). To avoid false conclusions, we have evaluated only Si-normalized mole-ratios.

Quantitative comparisons of interiors to exteriors using Si-normalized mole-ratios (hereafter, ratios) show several commonalities among the lower Shoemaker breccias (Fig. 17a). Magnesium ratios are greater in all ten interiors, while Ca and Cl are lower in all, demonstrating unambiguous evidence for systematic compositional differences between interiors and cleaned surfaces. Sulfur ratios are lower in the Pierre Pinaut and Aguas Calientes targets except for one of the three Pierre Pinaut targets where it is slightly lower but within 3σ of the brushed analysis. Sulfur ratios are higher in Robert Frazer and Private John Potts interiors. The Br ratios (not shown) of Private Robert Frazier and Aguas Calientes are higher in the interiors, but otherwise are equivalent to the brushed targets within uncertainty. If we relax the confidence level to 2σ, Zn ratios are lower in the interiors of seven targets and are never higher in the interiors.

The common depletions in Ca and Cl in the interiors relative to brushed surfaces suggests that these elements were mobilized out of the shallow interiors and onto surfaces. In general, addition of Ca and Cl in a mole ratio of 1:2 to interior compositions can replicate the Ca/Si and Cl/Si ratios of the brushed surfaces (Fig. 17b). Only small amounts of Ca-Cl salt would need to be added; roughly 0.75-1.5 wt% if the salt is $CaCl_2$, more if it is a perchlorate. The Private John Potts and two of the Pierre Pinaut brushed surfaces have excess Ca over the simple model of Ca-Cl-salt addition. Unfortunately, there is no definitive explanation for these three brushed surface compositions, although mobilization of additional Ca salts could be the cause. The interior/exterior differences support a scenario in which Ca salts, dominated by Cl-bearing salts, have been wicked to the surfaces of rocks by small amounts of water.

The cause for higher Mg ratios in interiors is difficult to explain because there is no measured anion that could suggest mobilization of specific Mg salts in all cases. The abraded targets of Private Robert Frazer and Private John Potts have coupled enrichments of Mg and S, and removal of $MgSO_4$ from the surface targets could explain the higher MgO contents of the interior targets. For the other targets all measured anions excluding Br are lower in the interiors, but Br is at too low a concentration to balance variations in Mg content. This implies that the anion in a Mg salt is a light element not detected by the APXS, with carbonate being a plausible candidate. Magnesium carbonate is detected elsewhere on Mars and is especially prevalent in Nili Fossae where it is associated with olivine-rich units (e.g., Ehlmann et al, 2008; Niles et al., 2013). Magnesium-rich carbonate formation occurs during alteration of olivine to serpentine (e.g., Brown et al., 2010; Viviano et al., 2013). Magnesium-rich carbonate was detected by sister rover Spirit in Gusev crater as an alteration phase in the Comanche Spur outcrop, but this carbonate was calculated to contain a significant siderite component (Morris et al., 2010). There is no systematic difference for Fe between interior and surface analyses and thus any carbonate deposited in the interiors does not contain a significant siderite component.

The increase in Mg/Si in the interiors implies differential mobility of Mg relative to Si but the mechanism cannot be uniquely determined. The increase in Mg/Si could indicate either loss of Si from the surface or deposition of Mg just below the surface, but the latter is more plausible. A possible scenario to explain the common Mg, Ca and Cl differences between surfaces and ~1 mm depth in the Shoemaker breccias is as follows:

- Thin films of water periodically form on rock surfaces when atmospheric conditions allow, which the penetrate the interior by capillary action.
- Soluble alteration products within the rock are taken into solution.
- As water evaporates from the surface, the least soluble salts precipitate in voids in the rock, gradually filling cracks.
- The most soluble salts, such as $CaCl_2$ or $Ca(ClO_4)_2$, are concentrated on the surface as the last of the water evaporates.

The occurrence of a similar interior/surface compositional pattern for Shoemaker formation breccias from Cape York, Marathon Valley and Perseverance Valley demonstrates that it is a regional process that likely is relatively young. Rocks in Marathon and Perseverance Valleys show “rock tails” – small aligned linear ridges of matrix material emanating from clasts standing above the general outcrop surface – which are interpreted as abrasion shadows formed as saltating sand planes down outcrop surfaces (e.g., Sullivan et al., 2005). The rock tails are often several mm in width and of comparable height (Fig. 9). The amount of surface removed from the outcrop is thus at least of the same order as the typical depth of abrasion (1-2 mm) and indicates that formation of the Ca-Cl-rich crust is keeping pace with the abrasive removal of the outcrop surface. Golombek et al. (2006) have estimated denudation rates on Meridiani Planum during the Amazonian to be 10^{-2} to 10^{-3} m/Myr. If this rate applies to Marathon and Perseverance Valleys, then only 200,000 to 2,000,000 years is required to strip off 2 mm of rock surface. Higher rates of erosion (by one to two orders of magnitude) are associated with the degradation of small craters via sand abrasion and infill (Golombek et al., 2014), which would erode rock tails in 2,000 to 20,000 years. Thus, a strong case can be made that the Ca-Cl-rich crusts are being periodically renewed in very recent times.

5. Marquette Island

Marquette Island is an ~30×30 cm, wedge-shaped block standing on end on the hematite plains roughly 11,800 meters from the Endeavour crater rim (Fig. 18a). The side of first approach (front side) is dust covered, but the top is relatively dust free. We investigated brushed and abraded targets on the front side and an untreated target on the top. The top surface shows an irregular, granular morphology with lineations roughly parallel to the flat front side (Fig. 18b). The MI image of the untreated top surface shows angular-blocky to rounded grains in a fine-grained matrix (Fig. 18c). The MI image from the abrasion hole shows clasts of differing brightness, some darker than the matrix, some brighter (Fig. 18d). The larger clast-supported grains are poorly sorted, with no preferred orientation. There is no evidence for sedimentary structures or layering. There are instances of what appear to be semi-arcuate structures (Fig. 18d), which suggests the rock may contain what might have been glassy shards; the semi-arcuate structures are not common. The rock appears well lithified. Bright veins ~100 µm by ~2-3 mm are present (Fig. 18c), suggesting localized alteration. Some regions show possible igneous texture, confounding the textural interpretation of Marquette Island. The texture is not highly diagnostic of a process or origin but is grossly like the target Seminole on the Columbia Hills in Gusev crater. Yingst et al. (2007) considered Seminole to be part of a tephra sequence, while Crumpler et al. (2011) also included impact ejecta and epiclastic origins as possible modes of formation for clastic rocks on Columbia Hills, including Seminole.

The Mössbauer spectrometer was still active for the investigation of Marquette Island, and two targets were investigated. Because the APXS compositions were very similar, the Mössbauer data for the targets were combined and reduced as a single spectrum. The major iron-bearing minerals are olivine (70% of the Fe), pyroxene (24%) and nanophase ferric oxide (6%). This gives $Fe_{oliv}/(Fe_{oliv}+Fe_{pyx}) = 0.72$, and Fe^{3+}/Σ_{Fe} is 0.06. The nanophase ferric oxide is plausibly contained in dust coatings, and there is no indication of Fe-bearing alteration phases. This is consistent with results expected of a very fresh magmatic rock or a breccia composed of such rocks.

Seven APXS measurements were made on Marquette Island, one on an untreated target on the top side, two on brushed spots on the front side, and four analyses in an abrasion hole on the front side; we concentrate here on the abraded targets. Marquette Island is compositionally distinct from all other materials analyzed by Opportunity; all analyses are members of cluster 15 in the first AHCA model with only a single interloper of another rock type (Fig. 8; Table 4a), and are the sole residents of cluster 13 when the mobile elements are excluded (Table 4b). Marquette Island is lower in SiO_2 and TiO_2, and higher in MgO and Cr_2O_3 than Shoemaker formation breccias, the Matijevic formation or average Mars crust (Fig. 6). The closest compositional match to Marquette Island among materials studied by the MER mission are Adirondack-class basalts from Gusev crater but Marquette Island has higher MgO and lower CaO than the those.

The APXS spectra of Marquette Island includes scatter peaks that can be used to calculate excesses in light elements (Z < 11) in them compared to other samples of broadly similar composition. For geological samples, H, O and C are the most likely light elements. The scatter peaks arise from elastic (Rayleigh) and inelastic (Compton) scattering of Pu L_α X-rays emitted from the ^{244}Cm source. Rayleigh and Compton scattering cross sections have different Z dependencies for the X-rays. The fitted Compton/Rayleigh intensity ratio can be compared to a theoretically derived ratio based on measured oxide concentrations; if the two are identical, low Z elements are not present at significant quantities (see Campbell et al., 2008). An additional assumption is that the sample is homogeneous. The scatter peaks are sensitive to the overall composition of the sample at greater depth than sampled by the APXS for major elements. Therefore, a different composition at greater depth could cause differences in Compton/Rayleigh ratios that mimic a composition with excesses in Z < 11 elements.

The Compton/Rayleigh scatter peak ratio for individual Marquette Island spectra are compared to several spectra on basaltic rocks and soils that are closest in composition to Marquette Island from Meridiani Planum and Gusev crater (Fig. 19). The mean ratio for the Marquette Island spectra is well-resolved from that of the other basaltic composition targets. The Compton/Rayleigh ratios from the four abraded targets are not significantly different from those of the brushed and untreated targets indicating that an artifact of a heterogeneously layered surface can be ruled out. The scatter-peak data indicate an excess of light elements equivalent to ~15% excess oxygen in Marquette Island compared to other similar martian basaltic compositions.

Of the plausible light elements, additional O alone can be ruled out because the Mössbauer spectra show that the Fe_2O_3 content is negligible and there are no other multivalent major elements that could be at higher oxidation state than normal. Hydrogen (OH^- and/or H_2O) and CO_2 are possible candidates. (We exclude the possibility of abundant organic compounds or elemental C.) The ~15 wt% equivalent oxygen translates to ~14 wt% OH^-, ~13 wt% H_2O or ~5.5 wt% CO_2. We cannot determine which phase(s) might be present, but any carbonate or H-bearing phase cannot contain Mössbauer-detectable amounts of Fe. Regardless, despite the low ferric iron content that argues for a pristine rock, Marquette Island is either altered, or composed of near-pristine igneous clastic materials cemented by volatile-bearing phases such as magnesite, calcite, kieserite, etc. Marquette Island might be like Peace from Gusev crater: a clastic rock bound by a cementing agent (Squyres et al., 2006b). Peace was the weakest rock abraded in Gusev crater based on the specific grind energies calculated from the abrasion activity (1.4 J/mm^3 vs. 2.5-44.8 for other rocks, Thomson et al., 2013), and is much lower than the value for Marquette Island (11.5 J/mm^3). Peace is posited to be comprised of basaltic grains cemented by Mg- and Ca-sulfates (Ming et al., 2006). The greater strength and low-Z element content of Marquette Island indicates that this rock is plausibly a carbonate-cemented clastic rock of basaltic sand.

We conclude that Marquette Island is an ejecta block lying on the Burns formation indicating that the source crater for it is penecontemporaneous with, or postdates, deposition of the Burns sulfate sandstones. (If the former is correct, then Marquette Island is a lag boulder that was exhumed from the Burns formation.) Two nearby craters penetrate the Burns formation and excavated the underlying Noachian units. Iazu Crater is 6.8 km in diameter and located roughly

25 km south of Endeavour crater, and exposes a section of Burns formation overlying a lower section of altered basaltic composition crust (Powell et al., 2017). Bopolu Crater is 19 km in diameter and situated roughly 65 km southwest of Endeavour crater, and exposes a section of Meridiani plains rocks above the Noachian basement (Grant et al., 2016). Marquette Island plausibly is a fragment of the Noachian basement from one of these craters.

6. Nature of the Subdued Cratered Unit

The geologic map of Meridiani Planum by Hynek and Di Achille (2017) shows an expanse of the Noachian subdued cratered unit 35-55 km south of the region explored by Opportunity (Fig. 2). They interpret this unit to be composed of volcanic deposits including lava and pyroclastic flows, impact breccias, impact-melt sheets, and erosional deposits formed via fluvio-lacustrine and aeolian processes. The area immediately surrounding Opportunity for several tens to a hundred km or more in every direction is the Hesperian hematite unit (Hynek & Di Achille, 2017), which Opportunity observations show is a hematite-spherule lag deposit plus aeolian ripples that is from a few cm up to about a meter thick (Soderblom et al., 2004; Sullivan et al., 2005). The hematite spherules are weathered out of the Burns formation and thus it is probable that this formation immediately underlies the hematite unit everywhere within the map region (Fig. 2).

The Noachian/Hesperian Meridiani upper etched unit directly overlies the subdued cratered unit or the Noachian cratered unit along most of its southern, eastern and northern exposures (Fig. 2) (Hynek & Di Achille, 2017). This implies that the lower and middle Meridiani etched plains units could be absent at the Opportunity field site. Hynek and Di Achille (2017) concluded that the upper etched unit was formed as aeolian and/or volcanic deposits that were cemented by groundwater activity. The upper most few meters of this unit consists of the Burns formation, which is mostly sulfate-rich sandstones with a small amount of mudstone (Edgar et al., 2012; Grotzinger et al., 2005). The sandstones are mostly aeolian in origin, but some facies indicate localized fluvial reworking and deposition in a lacustrine setting is possible for some (Edgar et al., 2012, 2014; Grotzinger et al., 2005, 2006; Hayes et al., 2011). The fact that the hematite unit is absent over the Meridiani upper etched unit west, north and east of the area explored by Opportunity implies that classic Burns formation containing hematite concretions might not be present in these areas. This could be because the diagenetic processes that form the hematite spherules (McLennan et al., 2005) did not occur in those regions, because the Meridiani upper etched unit there is distinct from the Burns formation, or because the Burns formation and hematite unit have been eroded away.

Supporting evidence that the Burns formation directly overlies the subdued cratered unit in the region explored by Opportunity comes from studies of Bopolu and Iazu Craters just south and southwest of Endeavour crater (Fig. 2). Bopolu Crater lies inside ancient Miyamoto crater and is younger than Endeavour crater; it postdates deposition and some erosional stripping of the Meridiani plains units that partially fill Miyamoto crater (Grant et al., 2016). The crater wall exposes a Noachian surface directly overlain by layered sulfates of the Meridiani plains (Grant et al., 2016). The Noachian surface represents the floor of Miyamoto crater at the time the layered sulfates were deposited. Iazu Crater lies closer to Endeavour crater and shows a similar stratigraphy in its walls. Layered, hydrated-sulfate- and hematite-bearing rocks – Burns formation – directly overly basaltic composition rocks (spectral determinations of low- and high-Ca pyroxene) that contain smectite (Powell et al., 2017).

The subdued cratered unit at Endeavour crater is represented by the Matijevic formation and the lower units of the Shoemaker formation. These were target rocks at the Endeavour impact site in the region of the western rim. The Matijevic formation is of uncertain origin because the limited exposure on Cape York and lack of diagnostic structures or textures did not allow for firm conclusions. This formation is composed of fine-grained clastic rocks that could be an air fall deposit of volcaniclastic or impact origin (Crumpler et al., 2015). In contrast, the lower units of the Shoemaker formation are polymict impact breccias based on textures, and the small clast size and low clast to matrix ratio indicates that they represent distal ejecta from one or more impacts. The pitted rocks and dark basaltic rocks in Perseverance Valley are also part of the pre-Endeavour basement. Because the pitted rocks are within a narrow fracture zone, their mode of formation cannot be determined (Tait et al., 2019). The dark rocks that cap Wdowiak Ridge are likely moderately altered volcanic rocks on an exposed, uplifted block of the pre-impact surface (Mittlefehldt et al., 2018a). Thus, ground observations by Opportunity are consistent with mapping from orbit on the types of materials that compose the subdued cratered unit and give a more detailed look at the origin of some components of the unit.

Depending on the timing of the Endeavour impact, the upper Shoemaker may also be part of the subdued cratered unit. Grant et al. (2016) concluded that the Endeavour rim was degraded in part by fluvial processes and this is also indicated by modeling of Endeavour crater degradation (Hughes et al., 2019). Fluvial erosional and depositional processes were important in modifying subdued cratered unit surfaces, but not on the overlying Noachian cratered unit (Hynek & Di Achille, 2017).

The very-fine-grained Grasberg formation is of uncertain stratigraphy. It is an airfall deposit that drapes the lower slopes of the eroded Endeavour rim (Crumpler et al., 2015) and thus likely postdates the period of fluvial erosion that degraded the Endeavour rim. It almost certainly predates deposition of the Burns formation at Endeavour crater (Crumpler et al., 2015; Mittlefehldt et al., 2018a). Crumpler et al. (2015) suggested that the Grasberg formation could be part of a widespread, possibly global, unit, and likened it to the Medusae Fossae Formation. How it might fit into the stratigraphy mapped by Hynek and Di Achille (2017) is unclear.

7. Conclusions

The Shoemaker formation stratigraphy, particularly well-exposed at Marathon Valley, shows two types polymict impact breccia. Upper units are clast-rich with coarser clasts, while lower units are clast-poor with smaller clasts (Crumpler et al., 2020). Studies of impact breccias at terrestrial craters show that vertical size-sorting is not present in ejecta deposits, but that sorting does occur with radial distance from crater rims, with more distal ejecta having a smaller average clast size, and a higher matrix content (Hörz et al., 1983; Oberbeck, 1975). The Shoemaker formation stratigraphy with clast-rich and clast-poor units is thus inconsistent with deposition as a single ejecta deposit from an impact. We conclude that the lower units are more distal ejecta from one or more earlier impacts, and the upper units are ejecta from Endeavour crater. The lower units, plus the Matijevic formation exposed on Cape York, represent part of the pre-Endeavour geology, which we equate with being subunits of the Noachian subdued cratered unit (Hynek & Di Achille, 2017). The lower Shoemaker units represent at least two depositions of distal impact ejecta and attest to the vibrancy of impact processes in the Noachian. The Matijevic formation, considered correlative with the lower Shoemaker units (Crumpler et al., 2020), could also be distal impact ejecta or it could be a volcaniclastic deposit (Crumpler et al., 2015). The Matijevic formation is compositionally distinct from the Shoemaker formation (Crumpler et al., 2015; Mittlefehldt et al., 2018a) and attests to the lithic diversity of the subdued crater unit.

Statistical modeling of compositions sans volatile (S, Cl and Br) and mobile (P, Mn, Ni and Zn) elements show that the upper and lower subunits of the Shoemaker formation are for the most part indistinguishable. This indicates that lithic material like the lower Shoemaker formation is the major component of the upper Shoemaker. An exception is the Copper Cliff member on Cape York which contains a significant component of the underlying Matijevic formation. This indicates that a ballistic erosion-sedimentation process was important in deposition of the Copper Cliff member (Mittlefehldt et al., 2018a). Modeling that includes the mobile elements shows that Shoemaker formation rocks from Cape York can be distinguished from those on Cape Tribulation. This suggests general differences in style and/or degree of alteration between the two rim segments (cf., Mittlefehldt et al., 2018a).

Unique to the pre-Endeavour rocks is alteration involving enrichments in Si and Al in vein-like structures that crosscut outcrops, and formation of smectite. Boxwork veins cutting the Matijevic formation were formed as mixtures of montmorillonite and silica produced by moderate-temperature alteration of bedrock by circumneutral to mildly alkaline fluids under high water/rock conditions (Clark et al., 2016). Red-zone group rocks form curvilinear traces cutting lower Shoemaker formation bedrock and are enriched in Si, Al, and sometimes Ge, compared to host bedrock. The Ge and at least some of the silica was formed by precipitation from hydrothermal fluids, indicating alteration under high water/rock. Ferric smectite was observed from orbit in a small region on Cape York and in Marathon Valley. The former is in dark veneers on Matijevic formation outcrops (Arvidson et al., 2014), while the latter is hosted in the lower-1 and lower-2 units of the Shoemaker formation. Association of ferric smectite in the Noachian basement is also indicated by observations of smectite-bearing basaltic-composition rock in the walls of Iazu Crater (Powell et al., 2017) and the floor of Miyamoto crater (Wiseman et al., 2008).

Post-Endeavour alteration is dominated by sulfate formation. Fracture zones in the crater rim include regions of alteration that produced Mg-sulfates as a dominant phase. This plausibly occurred as heated groundwaters circulated through the newly formed fractures and thus was closely associated in time with the impact (e.g., Arvidson et al., 2016), or could have occurred at some much later time, for example during the period of fluvial modification of the crater. Ca-sulfate vein formation also occurred, some pre-Endeavour and some much later. Coarse $CaSO_4$-veins in the Grasberg formation and those in the upper Shoemaker formation near the current ridge crest were formed only after the Endeavour rim had been substantially degraded, and likely after deposition of the Burns formation (Arvidson et al., 2014; Crumpler et al., 2015; Mittlefehldt et al., 2018a). However, some Ca-sulfate veins were formed during pre-Endeavour times, as demonstrated by veins crosscutting the Matijevic formation (Arvidson et al., 2014; Crumpler et al., 2015; Mittlefehldt et al., 2018a). The Ca-sulfate component of the Gasconade composite vein might also be pre-Endeavour.

Endeavour crater is Noachian in age, and thus, the upper Shoemaker unit might also be part of the subdued cratered unit. The degradation of Endeavour crater rim took place when surface waters were actively modifying surface morphology (Hughes et al., 2019), which is characteristic of the subdued crater unit (Hynek & Di Achille, 2017). However, the differences in alteration styles recorded in the upper Shoemaker vs. lower Shoemaker and Matijevic formation indicate that the former was deposited after a substantial time gap.

Comparison of compositions of brushed rock surfaces and abraded interiors show systematic differences in Mg content and coupled differences in Ca and Cl that occur over depths as little as 1-2 mm. These are interpreted as arising from mobilization of near-surface salts by transient thin films of water followed by precipitation at different depths close to and on the surface. The rock surfaces are undergoing wind erosion as demonstrated by wind tails of mm-scale height formed behind erosion-resistant clasts. Estimates of erosion rates on Meridiani Planum indicate that 2 mm of outcrop surface can be removed within 2 million years; possibly much less than this (Golombek et al., 2006; 2014). Thus, Ca-Cl-salt deposition on surfaces must be renewed on this timescale, indicating that salt mobilization by transient water has occurred very recently, and could be ongoing.

Acknowledgements-Rover operations described in this paper were conducted at the Jet Propulsion Laboratory, California Institute of Technology, under a contract with NASA. We thank the members of the MER project who enabled daily science observations at the Opportunity landing site. The senior author was supported by NASA through the Mars Exploration Rover Participating Scientist Program, and Planetary Science Research Programs. All data used in this article are listed in the references, tables, and supplements. [Data tables 1 through 6 will be hosted in a data repository. We are currently seeking a host for the data.] Data for APXS integrations on all rock and soil targets acquired by Opportunity are available on the NASA Planetary Data System website: http://pds-geosciences.wustl.edu/.

References

Aitchison, J. (1994). Principles of compositional data analysis. In: *Multivariate analysis and its applications*. Anderson, T. W., Fang, K. T., & Olkin, I. (eds.) Institute of Mathematical Statistics, Lecture Notes Monograph Series 24, Hayward, CA, 73-81.

Andrews-Hanna, J. C., & Lewis, K. W. (2011). Early Mars hydrology: 2. Hydrological evolution in the Noachian and Hesperian epochs. *Journal of Geophysical Research: Planets*, *116*(E2), E02007. doi:10.1029/2010JE003709

Andrews-Hanna, J. C., Phillips, R. J., & Zuber, M. T. (2007). Meridiani Planum and the global hydrology of Mars. *Nature*, *446*(7132), 163-166. doi:10.1038/nature05594

Arvidson, R. E., Ashley, J. W., Bell, J. F., Chojnacki, M., Cohen, J., Economou, T. E., et al. (2011). *Opportunity* Mars Rover mission: Overview and selected results from Purgatory ripple to traverses to Endeavour crater. *Journal of Geophysical Research: Planets*, *116*(E7), E00F15. doi:10.1029/2010JE003746

Arvidson, R. E., Squyres, S. W., Bell, J. F., Catalano, J. G., Clark, B. C., Crumpler, L. S., et al. (2014). Ancient Aqueous Environments at Endeavour crater, Mars. *Science*, *343*(6169). doi:10.1126/science.1248097

Arvidson, R. E., Squyres, S. W., Morris, R. V., Knoll, A. H., Gellert, R., Clark, B. C., et al. (2016). High concentrations of manganese and sulfur in deposits on Murray Ridge, Endeavour crater, Mars. *American Mineralogist*, *101*(6), 1389-1405. doi:10.2138/am-2016-5599

Bell III, J. F., Squyres, S. W., Herkenhoff, K. E., Maki, J. N., Arneson, H. M., Brown, D., et al. (2003). Mars exploration rover Athena panoramic camera (Pancam) investigation. *Journal of Geophysical Research: Planets (1991–2012)*, *108*(E12). doi:10.1029/2003JE002070

Berger, J. A., Schmidt, M. E., Gellert, R., Boyd, N. I., Desouza, E. D., Flemming, R. L., et al. (2017). Zinc and germanium in the sedimentary rocks of Gale crater on Mars indicate hydrothermal enrichment followed by diagenetic fractionation. *Journal of Geophysical Research: Planets*, *122*(8), 1747-1772.

Bernstein, L. R. (1985). Germanium geochemistry and mineralogy. *Geochimica et Cosmochimica Acta*, *49*(11), 2409-2422.

Bray, V. J., Tornabene, L. L., Keszthelyi, L. P., McEwen, A. S., Hawke, B. R., Giguere, T. A., et al. (2010). New insight into lunar impact melt mobility from the LRO camera. *Geophysical Research Letters*, *37*(21).

Brown, A. J., Hook, S. J., Baldridge, A. M., Crowley, J. K., Bridges, N. T., Thomson, B. J., et al. (2010). Hydrothermal formation of clay-carbonate alteration assemblages in the Nili Fossae region of Mars. *Earth and Planetary Science Letters*, *297*(1-2), 174-182.

Cabrol, N. A., Herkenhoff, K., Knoll, A. H., Farmer, J., Arvidson, R., Grin, E., et al. (2014). Sands at Gusev crater, Mars. *Journal of Geophysical Research: Planets*, 119(5), 941-967.

Campbell, J. L., Gellert, R., Lee, M., Mallett, C. L., Maxwell, J. A., & O'Meara, J. M. (2008). Quantitative in situ determination of hydration of bright high−sulfate Martian soils. *Journal of Geophysical Research: Planets*, *113*(E6).

Chayes, F. (1971). *Ratio correlation: a manual for students of petrology and geochemistry*. 99 pp., University of Chicago Press, Chicago.

Clark, B. C., Arvidson, R. E., Gellert, R., Morris, R. V., Ming, D. W., Richter, L., et al. (2007). Evidence for montmorillonite or its compositional equivalent in Columbia Hills, Mars. *Journal of Geophysical Research: Planets* 112, E06S01. https://doi.org/10.1029/2006JE002756

Clark, B. C., Morris, R. V., Herkenhoff, K. E., Farrand, W. H., Gellert, R., Jolliff, B. L., et al. (2016). Esperance: Multiple episodes of aqueous alteration involving fracture fills and coatings at Matijevic Hill, Mars. *American Mineralogist*, *101*(7), 1515-1526.

Crumpler, L. S., Arvidson, R. E., Squyres, S. W., McCoy, T., Yingst, A., Ruff, S., et al. (2011). Field reconnaissance geologic mapping of the Columbia Hills, Mars, based on Mars Exploration Rover Spirit and MRO HiRISE observations. *Journal of Geophysical Research: Planets*, *116*(E7).

Crumpler, L. S., Arvidson, R. E., Bell, J., Clark, B. C., Cohen, B. A., Farrand, W. H., et al. (2015). Context of ancient aqueous environments on Mars from in situ geologic mapping at Endeavour crater. *Journal of Geophysical Research: Planets*, *120*(3), 2014JE004699. doi:10.1002/2014JE004699

Crumpler, L. S., Arvidson, R. E., Mittlefehldt, D. W., Grant, J. A., Farrand, W. H., & the Athena Science Team (2019). In Situ Mapping of the Structural and Stratigraphic Complexities of Endeavour crater's Rim. Paper presented at 50th Lunar and Planetary Science Conference, Abstract #1179, Houston, TX, USA.

Crumpler, L. S., Arvidson, R. E., Mittlefehldt, D. W., Grant, J. A., & Farrand, W. H. (2020). Results from the first geologic traverse on the topographic rim of a complex impact crater, Endeavour Crater, Mars. *Geology*, *48(3)*, 252-257. (2020). https://doi.org/10.1130/G46903.1

Edgar, L. A., J. P. Grotzinger, A. G. Hayes, D. M. Rubin, S. W. Squyres, J. F. Bell, et al. (2012). Stratigraphic architecture of bedrock reference section, Victoria crater, Meridiani Planum, Mars. *Sedimentary Geology of Mars, SEPM Special Publication*, *102*, 195-209.

Edgar, L. A., Grotzinger, J. P., Bell III, J. F., & Hurowitz, J. A. (2014). Hypotheses for the origin of fine-grained sedimentary rocks at Santa Maria crater, Meridiani Planum. *Icarus*, *234*, 36-44.

Eggleton, R. A., Foudoulis, C., & Varkevisser, D. (1987). Weathering of basalt: Changes in rock chemistry and mineralogy. *Clays and Clay Minerals, 35*(3), 161-169.

Ehlmann, B. L., Mustard, J. F., Murchie, S. L., Poulet, F., Bishop, J. L., Brown, A. J., et al. (2008). Orbital identification of carbonate-bearing rocks on Mars. *Science*, *322*(5909), 1828-1832.

Escoube, R., Rouxel, O. J., Edwards, K., Glazer, B., & Donard, O. F. (2015). Coupled Ge/Si and Ge isotope ratios as geochemical tracers of seafloor hydrothermal systems: case studies at Loihi Seamount and East Pacific Rise 9 50′ N. *Geochimica et Cosmochimica Acta*, *167*, 93-112.

Farrand, W. H., Johnson, J. R., Bell, J. F. III & Mittlefehldt, D. W. (2016). VNIR Multispectral Observations of Rocks at Spirit of St. Louis Crater and Marathon Valley on the Rim of Endeavour crater Made by the Opportunity Rover Pancam. Paper presented at 47th Lunar and Planetary Science Conference, Abstract #1983, Houston, TX, USA.

Farrand, W. H., Johnson, J. R., Bell, J. F. III, Mittlefehldt, D. W., Schröder, C., Tait, A., Arvidson, R. E. & Crumpler, L. C. (2019). Spectral Variability Among Rocks and Soils in Perseverance Valley, Mars as Observed by the Opportunity Pancam. Paper presented at 50th Lunar and Planetary Science Conference, Abstract #2403, Houston, TX, USA.

Fox, V. K., Arvidson, R. E., Guinness, E. A., McLennan, S. M., Catalano, J. G., Murchie, S. L., & Powell, K. E. (2016). Smectite deposits in Marathon Valley, Endeavour crater, Mars, identified using CRISM hyperspectral reflectance data. *Geophysical Research Letters*, 43, 4885-4892. doi:10.1002/2016GL069108

Gellert, R., Rieder, R., Brückner, J., Clark, B. C., Dreibus, G., Klingelhöfer, G., et al. (2006). Alpha Particle X-Ray Spectrometer (APXS): Results from Gusev crater and calibration report. *Journal of Geophysical Research: Planets*, *111*(E2), E02S05. doi:10.1029/2005JE002555

Golombek, M. P., Grant, J. A., Crumpler, L. S., Greeley, R., Arvidson, R. E., Bell III, J. F., et al. (2006). Erosion rates at the Mars Exploration Rover landing sites and long‐term climate change on Mars. *Journal of Geophysical Research: Planets (1991–2012)*, *111*(E12).

Golombek, M. P., Warner, N. H., Ganti, V., Lamb, M. P., Parker, T. J., Fergason, R. L., & Sullivan, R. (2014). Small crater modification on Meridiani Planum and implications for erosion rates and climate change on Mars. *Journal of Geophysical Research: Planets 119*(12), 2522-2547. doi:10.1002/2014JE004658

Gorevan, S. P., Myrick, T., Davis, K., Chau, J. J., Bartlett, P., Mukherjee, S., et al. (2003). Rock abrasion tool: Mars exploration rover mission. *Journal of Geophysical Research: Planets (1991–2012)*, *108*(E12).

Grant, J. A., Crumpler, L. S., Parker, T. J., Golombek, M. P., Wilson, S. A., & Mittlefehldt, D. W. (2015). Degradation of Endeavour crater, Mars. Paper presented at 46th Lunar and Planetary Science Conference, Abstract #2017, Houston, TX, USA.

Grant, J. A., Parker, T. J., Crumpler, L. S., Wilson, S. A., Golombek, M. P., & Mittlefehldt, D. W. (2016). The degradational history of Endeavour crater, Mars. *Icarus, 280,* 22-36. doi:http://dx.doi.org/10.1016/j.icarus.2015.08.019

Grotzinger, J. P., Arvidson, R. E., Bell III, J. F., Calvin, W., Clark, B. C., Fike, D. A., et al. (2005). Stratigraphy and sedimentology of a dry to wet eolian depositional system, Burns formation, Meridiani Planum, Mars. *Earth and Planetary Science Letters*, *240*(1), 11-72. doi:ttps://doi.org/10.1016/j.epsl.2005.09.039

Grotzinger, J., Bell III, J., Herkenhoff, K., Johnson, J., Knoll, A., McCartney, E., et al. (2006). Sedimentary textures formed by aqueous processes, Erebus crater, Meridiani Planum, Mars. *Geology*, *34*(12), 1085-1088. doi:10.1130/g22985a.1

Hayes, A. G., Grotzinger, J. P., Edgar, L. A., Squyres, S. W., Watters, W. A., & Sohl−Dickstein, J. (2011). Reconstruction of eolian bed forms and paleocurrents from cross−bedded strata at Victoria Crater, Meridiani Planum, Mars. *Journal of Geophysical Research: Planets*, *116*(E7).

He, D., Lee, C. T. A., Yu, X., & Farner, M. (2019). Ge/Si partitioning in igneous systems: Constraints from laser ablation ICP−MS measurements on natural samples. *Geochemistry, Geophysics, Geosystems*, *20*(10), 4472-4486.

Herkenhoff, K. E., Squyres, S. W., Bell, J. F., Maki, J. N., Arneson, H. M., Bertelsen, P., et al. (2003). Athena Microscopic Imager investigation. *Journal of Geophysical Research: Planets (1991–2012)*, *108*(E12).

Hörz, F., R. Ostertag, & D. A. Rainey (1983). Bunte Breccia of the Ries: Continuous deposits of large impact craters. *Reviews of Geophysics*, *21*(8), 1667-1725. doi:10.1029/RG021i008p01667

Hughes, M. N., Arvidson, R. E., Grant, J. A., Wilson, S. A., Howard, A. D., & Golombek, M. P. (2019). Degradation of Endeavour crater based on orbital and rover−based observations in combination with landscape evolution modeling. *Journal of Geophysical Research: Planets*, *124*(6), 1472-1494. doi:10.1029/2019je005949

Hurowitz, J. A., & McLennan, S. M. (2007). A~ 3.5 Ga record of water-limited, acidic weathering conditions on Mars. *Earth and Planetary Science Letters*, *260*(3-4), 432-443.

Hynek, B. M., & Di Achille, G. (2017). *Geologic map of Meridiani Planum, Mars*. (Scientific Investigations Map 3356). Washington, DC: U.S. Geological Survey. https://doi.org/10.3133/sim3356

Hynek, B. M., & Phillips, R. J. (2008). The stratigraphy of Meridiani Planum, Mars, and implications for the layered deposits' origin. *Earth and Planetary Science Letters*, *274*(1–2), 214-220. doi:https://doi.org/10.1016/j.epsl.2008.07.025

Hynek, B. M., Arvidson, R. E. & Phillips, R. J. (2002). Geologic setting and origin of Terra Meridiani hematite deposit on Mars. *Journal of Geophysical Research: Planets*, *107*(E10), 5088, doi:10.1029/2002je001891

Johnson, J. R., Bell III, J. F., Cloutis, E., Staid, M., Farrand, W. H., McCoy, T., et al. (2007). Mineralogic constraints on sulfur−rich soils from Pancam spectra at Gusev crater, Mars. *Geophysical Research Letters*, *34*(13), L13202. doi:10.1029/2007GL029894

Jolliff, B. L., Mittlefehldt, D. W., Farrand, W. H., Knoll, A. H., McLennan, S. M., & Gellert, R. (2019). Mars Exploration Rover Opportunity: Water and other volatiles on ancient Mars. In

J. Filiberto, S. P. Schwenzer (Eds.), *Volatiles in the Martian Crust* (pp. 285-328). Amsterdam, Netherlands: Elsevier. doi:https://doi.org/10.1016/B978-0-12-804191-8.00010-6.

Klingelhöfer, G., Morris, R. V., Bernhardt, B., Rodionov, D., de Souza Jr, P. A., Squyres, S. W., et al. (2003). Athena MIMOS II Mössbauer spectrometer investigation. *Journal of Geophysical Research: Planets (1991–2012)*, *108*(E12). doi:10.1029/2003JE002138

Macdonald, R., McGarvie, D. W., Pinkerton, H., Smith, R. L., & Palacz, A. (1990). Petrogenetic evolution of the Torfajökull Volcanic Complex, Iceland I. Relationship between the magma types. *Journal of Petrology*, *31*(2), 429-459.

Mader, M. M., & Osinski, G. R. (2018). Impactites of the Mistastin Lake impact structure: Insights into impact ejecta emplacement. *Meteoritics & Planetary Science*, *53*(12), 2492-2518.

Maki, J. N., Bell, J. F., Herkenhoff, K. E., Squyres, S. W., Kiely, A., Klimesh, M., et al. (2003). Mars Exploration Rover engineering cameras. *Journal of Geophysical Research: Planets*, *108*(E12).

McLennan, S. M., Bell III, J. F., Calvin, W. M., Christensen, P. R., Clark, B. D., De Souza, P. A., et al. (2005). Provenance and diagenesis of the evaporite-bearing Burns formation, Meridiani Planum, Mars. *Earth and Planetary Science Letters*, *240*(1), 95-121.

Meunier, A., Caner, L., Hubert, F., El Albani, A., & Prêt, D. (2013). The weathering intensity scale (WIS): an alternative approach of the chemical index of alteration (CIA). *American Journal of Science*, *313*(2), 113-143.

Ming, D. W., Mittlefehldt, D. W., Morris, R. V., Golden, D. C., Gellert, R., Yen, A., et al. (2006). Geochemical and mineralogical indicators for aqueous processes in the Columbia Hills of Gusev Crater, Mars. *Journal of Geophysical Research: Planets* 111, E02S12. https://doi.org/10.1029/2005JE002560

Mittlefehldt, D. W., Gellert, R., Herkenhoff, K. E., Morris, R. V., Clark, B. C., Cohen, B. A., et al. (2010). Marquette Island: A distinct mafic lithology discovered by Opportunity. Paper presented at 41st Lunar and Planetary Science Conference, Abstract #2109, Houston, TX, USA.

Mittlefehldt, D. W., Gellert, R., Ming, D. W., Yen, A. S., Clark, B. C., Morris, R. V., et al. (2018a). Diverse lithologies and alteration events on the rim of Noachian-aged Endeavour crater, Meridiani Planum, Mars: In situ compositional evidence. *Journal of Geophysical Research: Planets*, 123(5), 1255-1306. doi:10.1002/2017JE005474

Mittlefehldt, D. W., Crumpler, L. S., Grant, J. A., Arvidson, R. E., & Farrand W. H. (2018b). Noachian-aged pre-impact lithology exposed in Endeavour crater rim: Mars Exploration Rover Opportunity observations. Paper presented at 2018 Geological Society of America Annual Meeting.

Mittlefehldt, D. W., Arvidson, R. E., Crumpler, L. S., Farrand, W. H., Gellert, R., Grant, J. A., et al. (2019a). Geochemistry of Noachian bedrock and alteration events, Endeavour crater, Mars. Paper presented at 50th Lunar and Planetary Science Conference, Abstract #1100, Houston, TX, USA.

Mittlefehldt, D. W., R. Gellert, D. W. Ming, & A. S. Yen (2019b). Alteration processes in Gusev crater, Mars: Volatile/mobile element contents of rocks and soils determined by the Spirit Rover. In J. Filiberto, S. P. Schwenzer (Eds.), *Volatiles in the Martian Crust* (pp. 329-368). Amsterdam, Netherlands: Elsevier. doi:https://doi.org/10.1016/B978-0-12-804191-8.00011-8

Morris, R.V., Ruff, S.W., Gellert, R., Ming, D.W., Arvidson, R.E., Clark, B.C., et al. (2010). Identification of carbonate-rich outcrops on Mars by the Spirit rover. *Science*, *329*(5990), 421-424. doi:10.1126/science.1189667

Mortlock, R. A., Froelich, P. N., Feely, R. A., Massoth, G. J., Butterfield, D. A., & Lupton, J. E. (1993). Silica and germanium in Pacific Ocean hydrothermal vents and plumes. *Earth and Planetary Science Letters*, *119*(3), 365-378.

Nesbitt, H. W., & Wilson, R. E. (1992). Recent chemical weathering of basalts. *American Journal of science*, *292*(10), 740-777.

Newsom, H. E., Barber, C. A., Hare, T. M., Schelble, R. T., Sutherland, V. A., & Feldman, W. C. (2003). Paleolakes and impact basins in southern Arabia Terra, including Meridiani Planum: Implications for the formation of hematite deposits on Mars. *Journal of Geophysical Research: Planets*, *108*(E12). doi:10.1029/2002JE001993

Newsom, H.E., Lanza, N.L., Ollila, A.M., Wiseman, S.M., Roush, T.L., Marzo, G.A., et al. (2010). Inverted channel deposits on the floor of Miyamoto crater, Mars. *Icarus*, *205*(1), 64-72.

Niles, P. B., Catling, D. C., Berger, G., Chassefière, E., Ehlmann, B. L., Michalski, J. R., et al. (2013). Geochemistry of carbonates on Mars: implications for climate history and nature of aqueous environments. *Space Science Reviews*, *174*(1), 301-328.

Oberbeck, V. R. (1975). The role of ballistic erosion and sedimentation in lunar stratigraphy. Reviews of Geophysics, 13(2), 337-362. doi:doi:10.1029/RG013i002p00337

Parker, T. J., Golombek, M. P., Calef, F. J., & Hare, T. M. (2012). High-resolution basemaps for localization, mission planning, and geologic mapping at Meridiani Planum and Gale crater. Paper presented at 43rd Lunar and Planetary Science Conference, Abstract #2535, Houston, TX, USA.

Pokrovski, G. S., & Schott, J. (1998). Thermodynamic properties of aqueous Ge (IV) hydroxide complexes from 25 to 350 C: implications for the behavior of germanium and the Ge/Si ratio in hydrothermal fluids. *Geochimica et Cosmochimica Acta*, *62*(9), 1631-1642.

Powell, K. E., Arvidson, R. E., Zanetti, M., Guinness, E. A., & Murchie, S. L. (2017). The structural, stratigraphic, and paleoenvironmental record exposed on the rim and walls of Iazu Crater, Mars. Journal of Geophysical Research: Planets, 122(5), 1138-1156.

Reimold, W. U. (1995). Pseudotachylite in impact structures—generation by friction melting and shock brecciation?: A review and discussion. *Earth-Science Reviews*, *39*(3-4), 247-265.

Rieder, R., Gellert, R., Brückner, J., Klingelhöfer, G., Dreibus, G., Yen, A., & Squyres, S. W. (2003). The new Athena alpha particle X−ray spectrometer for the Mars Exploration Rovers, *Journal of Geophysical Research: Planets (1991–2012)*, *108*(E12).

Shoemaker, E. M. (1963). Impact mechanics at Meteor Crater, Arizona. In B. M. Middlehurst, G. P. Kuiper (Eds.), *The Moon, Meteorites and Comets*. (pp. 301-336). Chicago, IL, USA: University of Chicago Press.

Soderblom, L. A., Anderson, R. C., Arvidson, R. E., Bell, J. F., Cabrol, N. A., Calvin, W., et al. (2004). Soils of Eagle crater and Meridiani Planum at the Opportunity rover landing site. *Science*, *306*(5702), 1723-1726.

Squyres, S. W., & Knoll, A. H. (2005). Sedimentary rocks at Meridiani Planum: Origin, diagenesis, and implications for life on Mars. *Earth and Planetary Science Letters*, *240*(1), 1-10. doi:https://doi.org/10.1016/j.epsl.2005.09.038

Squyres, S. W., Arvidson, R. E., Baumgartner, E. T., Bell, J. F., Christensen, P. R., Gorevan, S., et al. (2003). Athena Mars rover science investigation. *Journal of Geophysical Research: Planets (1991–2012)*, *108*(E12).

Squyres, S. W., Arvidson, R. E., Bollen, D., Bell III, J. F., Brueckner, J., Cabrol, N. A., et al. (2006a). Overview of the *Opportunity* Mars Exploration Rover mission to Meridiani Planum: Eagle crater to Purgatory ripple. *Journal of Geophysical Research: Planets, 111*(E12), E12S12. doi:10.1029/2006je002771

Squyres, S. W., Arvidson, R. E., Blaney, D. L., Clark, B. C., Crumpler, L., Farrand, W. H., et al. (2006b). Rocks of the Columbia hills. *Journal of Geophysical Research: Planets*, *111*(E2).

Squyres, S. W., Arvidson, R. E., Bell, J. F., Calef, F., Clark, B. C., Cohen, B. A., et al. (2012). Ancient impact and aqueous processes at Endeavour crater, Mars. *Science*, *336*(6081), 570-576. doi:10.1126/science.1220476

Stopar, J. D., Hawke, B. R., Robinson, M. S., Denevi, B. W., Giguere, T. A., & Koeber, S. D. (2014). Occurrence and mechanisms of impact melt emplacement at small lunar craters. *Icarus*, *243*, 337-357.

Sullivan, R., Banfield, D., Bell, J. F., Calvin, W., Fike, D., Golombek, M., et al. (2005). Aeolian processes at the Mars Exploration Rover Meridiani Planum landing site. *Nature*, *436*(7047), 58-61.

Tait, A. W., Schröder, C., Farrand, W. H., Ashley, J. W., Cohen, B. A., Gellert, R., et al. (2019). Exploring origins of pitted/vesicular rocks in Perseverance Valley, Endeavour crater. Paper presented at 50th Lunar and Planetary Science Conference, Abstract #2327, Houston, TX, USA.

Taylor, S. R., & McLennan, S. M. (2009). *Planetary Crusts: Their Composition, Origin and Evolution*. Cambridge, UK: Cambridge University Press.

Thomson, B. J., Bridges, N. T., Cohen, J., Hurowitz, J. A., Lennon, A., Paulsen, G., & Zacny, K. (2013). Estimating rock compressive strength from Rock Abrasion Tool (RAT) grinds. *Journal of Geophysical Research: Planets*, *118*(6), 1233-1244. doi:10.1002/jgre.20061

Viviano, C. E., Moersch, J. E., & McSween, H. Y. (2013). Implications for early hydrothermal environments on Mars through the spectral evidence for carbonation and chloritization reactions in the Nili Fossae region. *Journal of Geophysical Research: Planets*, *118*(9), 1858-1872.

Wiseman, S. M., Arvidson, R. E., Andrews−Hanna, J. C., Clark, R. N., Lanza, N. L., Des Marais, D., et al. (2008). Phyllosilicate and sulfate-hematite deposits within Miyamoto crater in southern Sinus Meridiani, Mars. *Geophysical Research Letters*, *35*(19), L19204. doi:10.1029/2008GL035363

Wolters, F., Lagaly, G., Kahr, G., Nueeshch, R., & Emmerich, K. (2009). A comprehensive characterization of dioctahedral smectites. *Clays and Clay Minerals*, *57*(1), 115-133.

Wray, J. J., Noe Dobrea, E. Z., Arvidson, R. E., Wiseman, S. M., Squyres, S. W., McEwen, A. S., et al. (2009). Phyllosilicates and sulfates at Endeavour crater, Meridiani Planum, Mars. *Geophysical Research Letters*, *36*(21), L21201. doi:10.1029/2009gl040734

Yingst, R. A., Schmidt, M. E., Herkenhoff, K. E., Mittlefehldt, D. W., & the Athena Science Team (2007). Linking Home Plate and Algonquin class rocks through microtextural analysis: Evidence for hydrovolcanism in the inner basin of Columbia Hills, Gusev crater. Paper presented at 7th International Conference on Mars, Abstract #3296, Houston, TX, USA.

Tables (in Excel file; to be hosted on data repository)

Table 1. APXS data table.

Table 2. Average compositions of Shoemaker formation subunits.

Table 3. Element/Si mole ratios and cluster membership for targets used in Agglomerative Hierarchical Cluster Analysis.

Table 4a. Cluster hierarchy matrix from Agglomerative Hierarchical Cluster Analysis, excluding volatile elements (S, Cl, Br).

Table 4b. Cluster hierarchy matrix from Agglomerative Hierarchical Cluster Analysis, excluding volatile elements and mobile elements (P, Mn, Ni, Zn).

Table 5. Germanium concentrations for rocks in the Spirit of Saint Louis region.

Table 6. Qualitative synopsis of interior/exterior ratios for Shoemaker formation rocks.

Figure Captions

Figure 1. (a) High Resolution Imaging Science Experiment-based mosaic showing Endeavour crater. (b) Cape York. (c) The Cape Tribulation portion of the western rim showing the locations of Marathon and Perseverance Valleys. (d) Expanded view of Marathon Valley and Spirit of Saint Louis region. (e) Expanded view of Perseverance Valley region. Rover track shown in white. Images from HiRISE-based mosaic of Endeavour crater base map (Parker et al., 2012).

Figure 2. Portions of the geological map of Meridiani Planum showing the relationships between the Noachian subdued cratered unit, the Noachian/Hesperian upper etched unit and the Hesperian hematite unit in the vicinity of the Opportunity traverse. The legend shows geologic units discussed here with the rover-based units identified. Modified from Hynek & Di Achille (2017).

Figure 3. Pancam false-color images showing examples of macrotextures of Shoemaker formation outcrops: (a) Boesmanskop and Komati (clast), Greeley Haven member on Cape York (Sol 2795); (b) Moreton Island, upper Shoemaker formation on Murray Ridge, Cape Tribulation (Sol 3494); (c) Cape Elizabeth (outcrop block), upper Shoemaker, and Pinnacle Island (lose rock) in Cook Haven, Cape Tribulation (Sol 3540); (d) Thermopylae, lower-2 Shoemaker at Spirit of Saint Louis, Cape Tribulation (Sol 3998); (e) Smectite-rich outcrop, lower-1 Shoemaker in Marathon Valley (Sol 4419); (f) Mesilla, lower Shoemaker in Perseverance Valley (Sol 4880). False color rendered using Pancam left-eye filters 2, 5, and 7 centered on 753, 535, and 432 nm (hereafter L257). Scale bars are ~10 cm at the locations shown. The locations of these rocks can be found in online supplementary Figs. L02 through L04 and L09.

Figure 4. Schematic diagram of ejecta emplacement outside a complex crater, after Oberbeck (1975). Insets show the area at the base of the ejecta curtain at three different times; solid arrows show schematic vectors of ejecta fragment motion; open arrows show schematic vectors of ejecta deposit motion. α - ejection angle; V – ejection velocity.

Figure 5. Pancam false-color image (Gibraltar II panorama, L257) showing the contact between the upper and lower units of the Shoemaker formation in Marathon Valley. Images acquired between Sols 4446-4453. The location of this image can be found in online supplementary Fig. L07.

Figure 6. Element vs. SiO_2 diagrams for Endeavour crater rim rocks, normalized to a SO_3-, Cl- and Br-free basis. Anomalous targets are Sledge Island and Sarcobatus Clast 2; see text. Labeled points in (c) are: A – Allende; G – Gasconade; N – Nazas; T – Tomé. Dotted field encloses the abraded targets of Marquette Island. White field labeled b is abraded targets of Adirondack-class basalts from Gusev crater. Locations of Allende, Nazas and Tomé (pitted rocks) can be found in online supplementary Fig. L10; that of Gasconade in Fig. L06; and those of Sledge Island and Sarcobatus Clast 2 in Fig. L03.

Figure 7. Plot of SO_3 vs. Cl for Endeavour crater rim rocks.

Figure 8. Dendrogram of Agglomerative Hierarchical Cluster Analysis (AHCA) of Endeavour crater rim rocks and soils. Inset shows expanded view of cluster 1; see text for explanation.

Figure 9. Individual MI frames of Parral (Sol 4809), Waverly (Sol 4656) and Mesilla (Sol 4900) documenting the distinct texture of Parral compared to the upper Shoemaker target Waverly but like that of lower Shoemaker Mesilla. Clasts in Waverly (dark) are more abundant and up to 18 mm in size, while those in Parral (heads of wind tails) are fewer and smaller (largest ~3 mm across). Images are 31 mm across. The location of Parral and Mesilla can be found in online supplementary Fig. L10; that of Waverly in Fig. L08.

Figure 10. (a) Portion of a Pancam false-color mosaic (Sol 4033, L257) of red zone bordering north side of Spirit of Saint Louis with APXS/MI targets identified: B – Private William Bratton; C – Private Pierre Cruzatte; D – John Dame; R – Ryan NYP. (b) – (d) MI images of three of the APXS targets. Scale bar in (a) is ~25 cm at the location shown. MI images are 31 mm across. The location of these images can be found in online supplementary Fig. L05.

Figure 11. Element enrichments and depletions of red-zone rocks. (a) Comparison of red zone on the border of Spirit of Saint Louis with host bedrock on either side; inset shows details for enriched elements. (b) Ge vs. SiO_2 for rocks around Spirit of Saint Louis compared to similar rocks from Marathon Valley. Boxes on abscissa represent approximate detection limits for Ge, which encompass most analyses from Marathon Valley.

Figure 12. Alteration diagrams for Endeavour crater rim rock types, after (a) Nesbit and Wilson (1992) and (b) Meunier et al. (2013). Blue arrows show expected change for alteration under low water/rock in which olivine dissolves (Hurowitz & McLennan, 2007). White arrow joins host bedrock with red-zone rock from Spirit of Saint Louis (see Fig. 10). Curved arrows show alteration changes in Monaro basalts (Eggleton et al., 1987). Labeled pitted rock symbols are: A – Allende; N – Nazas; T – Tomé. Independence-class rocks from Gusev crater shown for comparison.

Figure 13. Images of pitted Nazas target from Perseverance Valley. (a) Portion of Pancam false-color image (Sol5042, L257) highlighting pit filled with reddish-orange alteration material. (b) Portion of Microscopic Imager image (Sol 5053) of the pit showing texture of the alteration material. The location of (a) can be found in online supplementary Fig. L09.

Figure 14. Element vs. SO_3 diagrams for altered rocks and soils from the Endeavour crater rim. Red circles enclose Si-rich red-zone-group targets from Gasconade, which also includes $CaSO_4$-rich components (red dashed tie lines).

Figure 15. (a) Pancam false-color image (Sol 4404, L257) of the wheel scuff exposing altered soils in a fracture in Shoemaker lower-1 showing locations of APXS targets. The line of red pebbles is a red zone transecting the outcrop. (b) Pancam false-color image (Sol 4504, L257) of the Gasconade vein complex (cyan arrows) cross cutting Shoemaker lower-1 on Spirit Mound; region of (c) indicated. (c) Pancam false-color image (Sol 4505, L257) of a portion of the Gasconade vein complex showing locations of APXS targets; $CaSO_4$-rich Gasconade and Gasconade 2, and Si-rich Gasconade3 and Gasconade 4. The location of (a) can be found in online supplementary Fig. L07; that of (b) and (c) in Fig. L08.

Figure 16. Comparison of Pancam spectra from light-toned soil exposed by Spirit rover scuff at the Arad target (MER-A Sol 721) and the yellow pebble Private Joseph Field at Opportunity's E

Cann scuff area (MER-B Sol 4379) (Fig. 15a). Each has a broad absorption centered between 803 and 864 nm attributed to Fe sulfate mineral(s). R* is relative reflectance; standard deviations are shown when larger than the symbol size.

Figure 17. (a) Molar element/Si in abraded interiors normalized to brushed surfaces for select elements. (b) Molar Cl/Si vs. Ca/Si for abraded and brushed targets, with the effect of adding 0.75 or 1.5 wt% $CaCl_2$ to interior compositions shown (see text).

Figure 18. (a) Pancam false-color image (Sol 2063, L257) of the front, dusty side of Marquette Island. The front face is roughly 30×30 cm in size. (b) Pancam false-color image (Sol 2089, L257) of the relatively dust-free top of Marquette Island. Peck Bay brush circle (front face, arrow) is 45 mm in diameter. (c) MI image of the hackly top surface of Marquette Island. Arrow points out thin, possible alteration vein. Image is 31 mm across. (d) Portion of an MI image of the abrasion hole showing clastic texture. Arrow points out arcuate, possible glass shard. Image is 15.5 mm across.

Figure 19. Compton/Rayleigh scatter peak ratio for Marquette Island analyses compared to those of compositionally similar basalts.

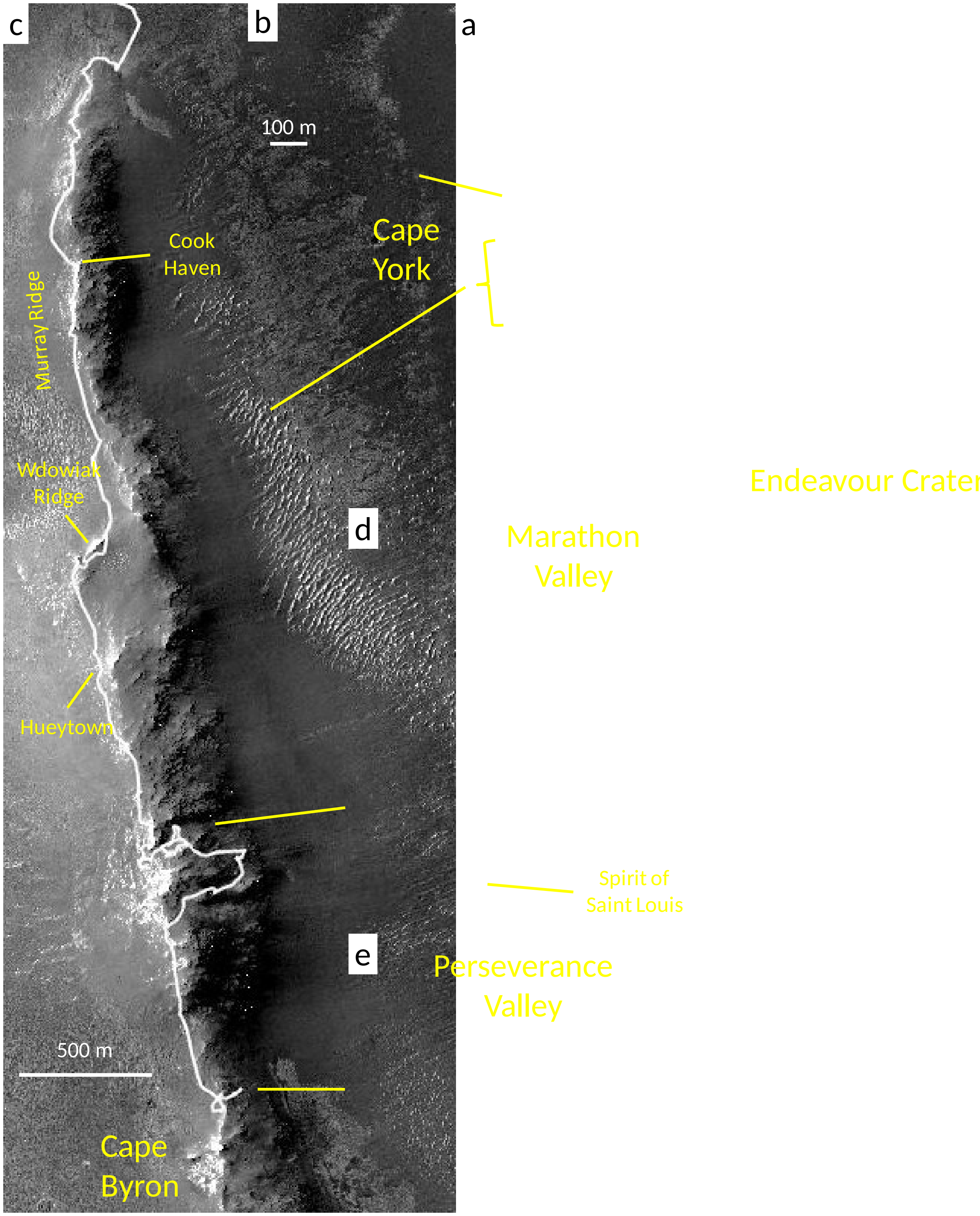
c
b
a
100 m
Cape
York
Cook
Haven
Murray Ridge
Wdowiak
Ridge
d
Endeavour Crater
Marathon
Valley
Hueytown
Spirit of
Saint Louis
e
Perseverance
Valley
500 m
Cape
Byron

Figure 1.

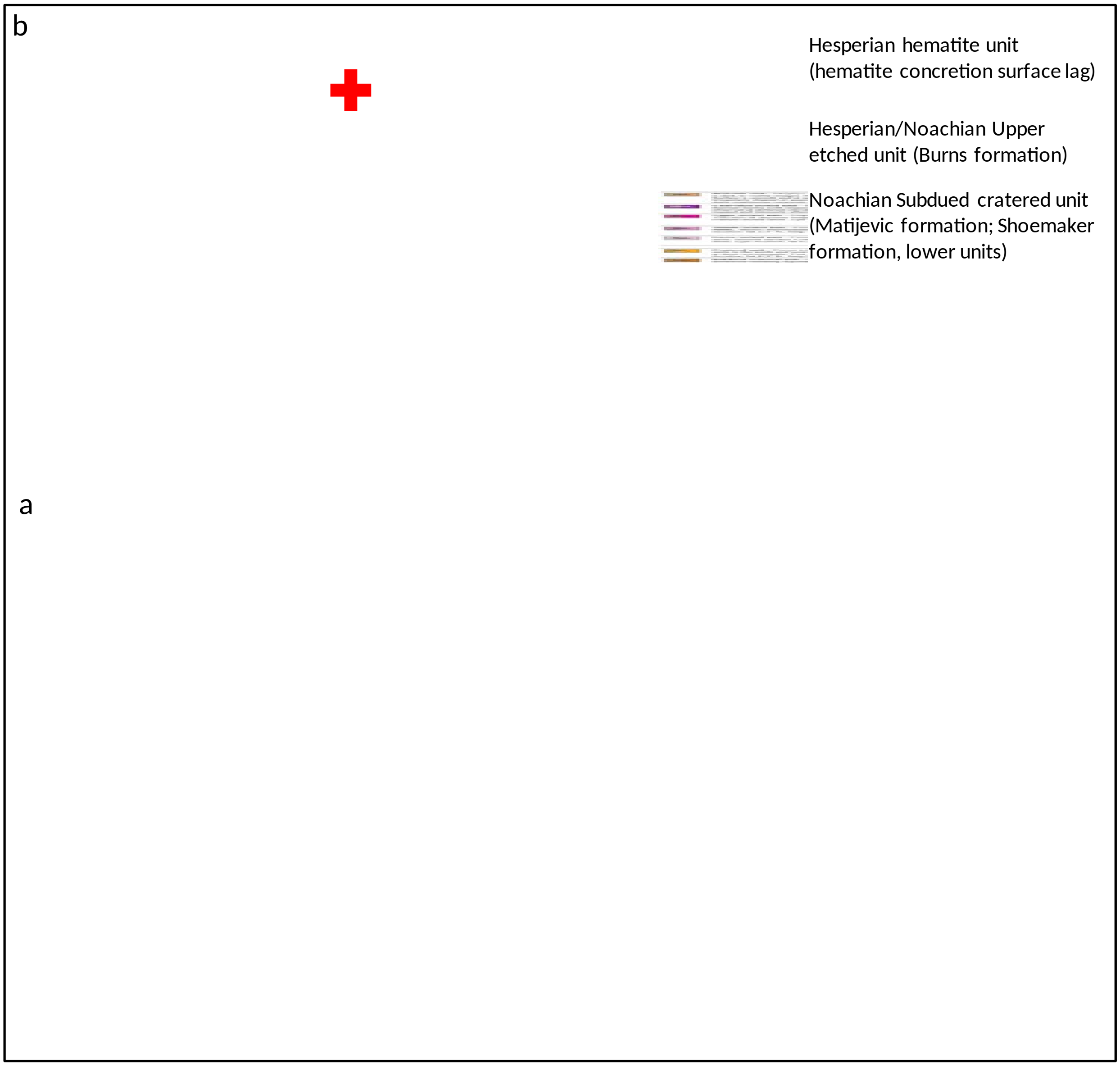
b
Hesperian hematite unit
(hematite concretion surface lag)
Hesperian/Noachian Upper
etched unit (Burns formation)
Noachian Subdued cratered unit
(Matijevic formation; Shoemaker
formation, lower units)
a

Figure 2.

a b c

d e

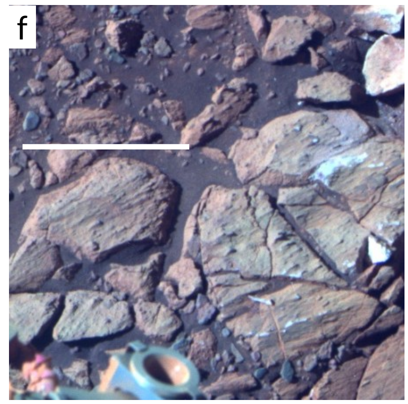

Figure 3.

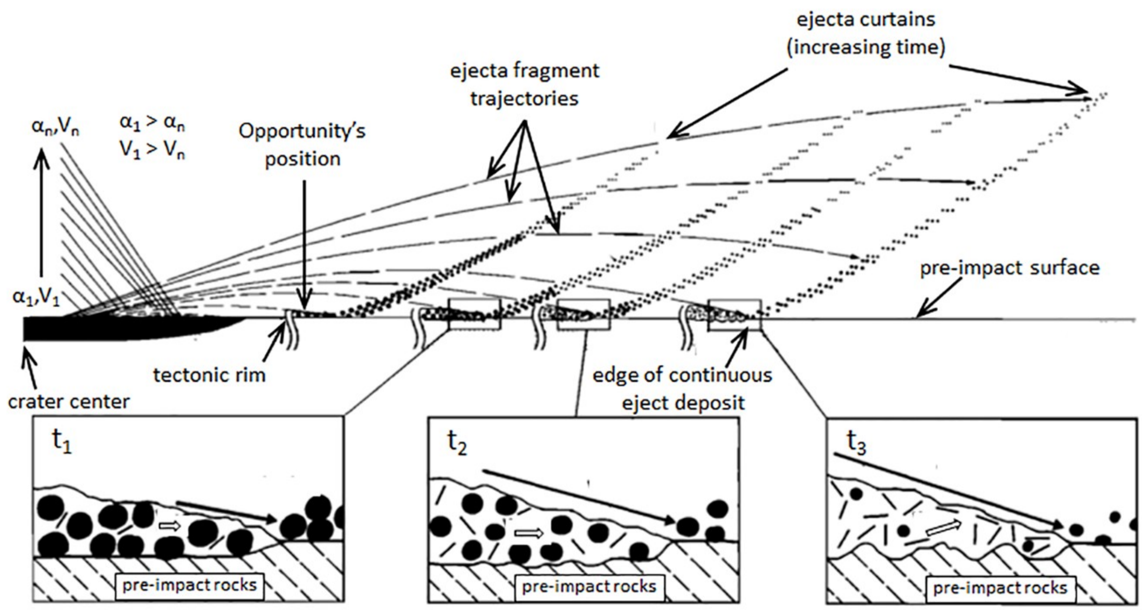
ejecta curtains
(increasing time)
ejecta fragment
trajectories
α_n,V_n
$\alpha_1 > \alpha_n$
$V_1 > V_n$
Opportunity's
position
pre-impact surface
α_1,V_1
tectonic rim
crater center
edge of continuous
eject deposit
t_1
pre-impact rocks
t_2
pre-impact rocks
t_3
pre-impact rocks

Figure 4.

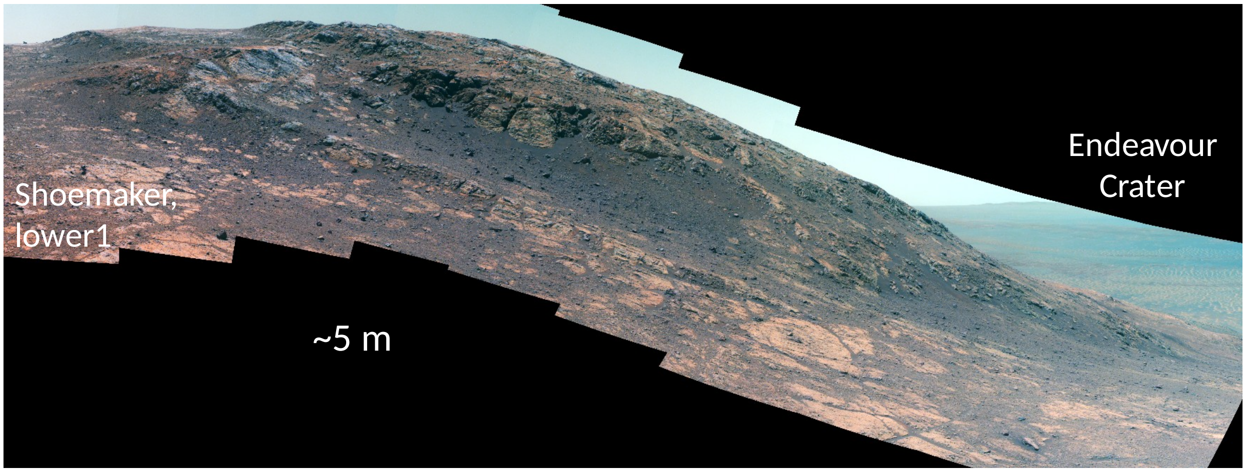

Figure 5.

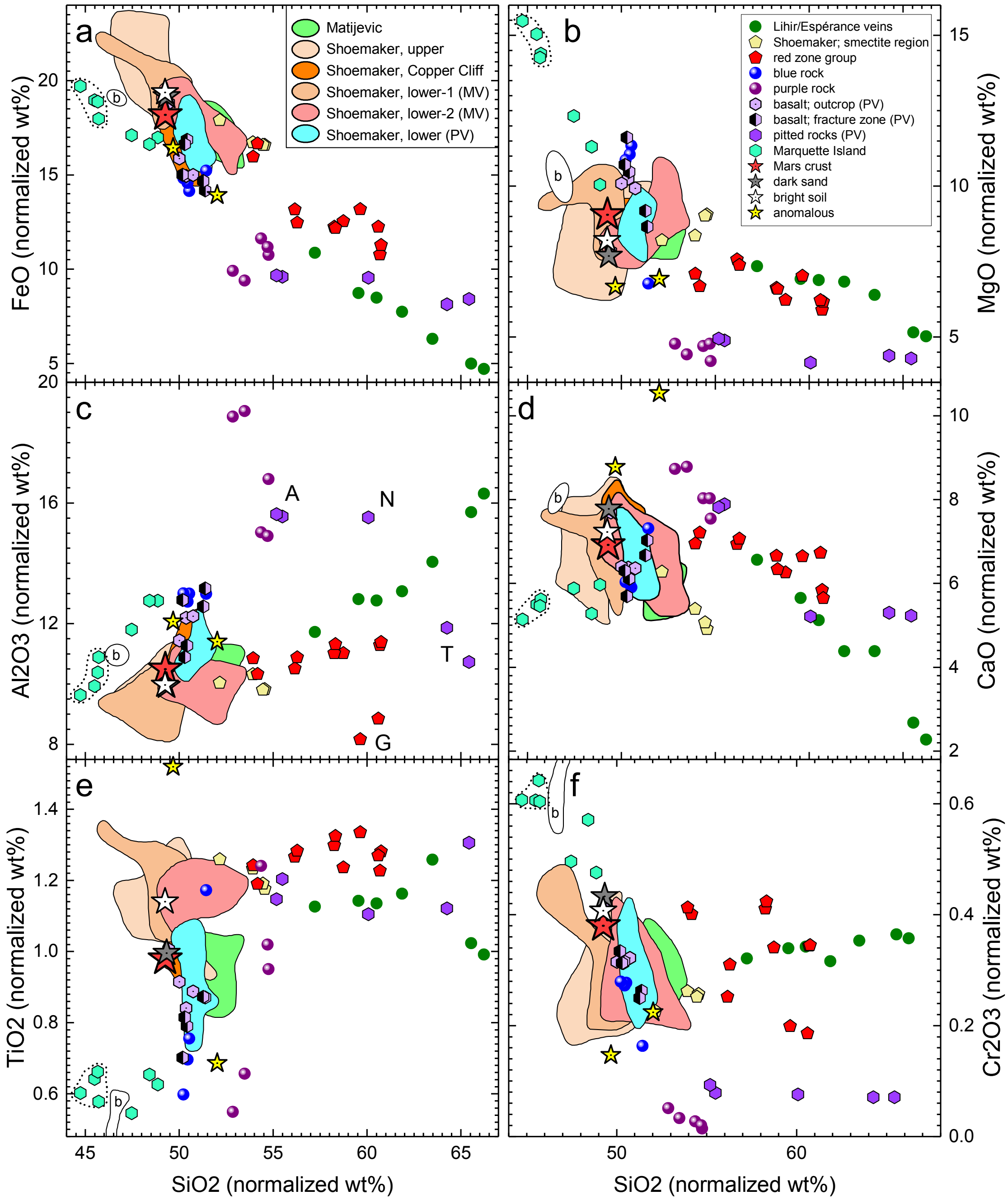

1551

1552 Figure 6.

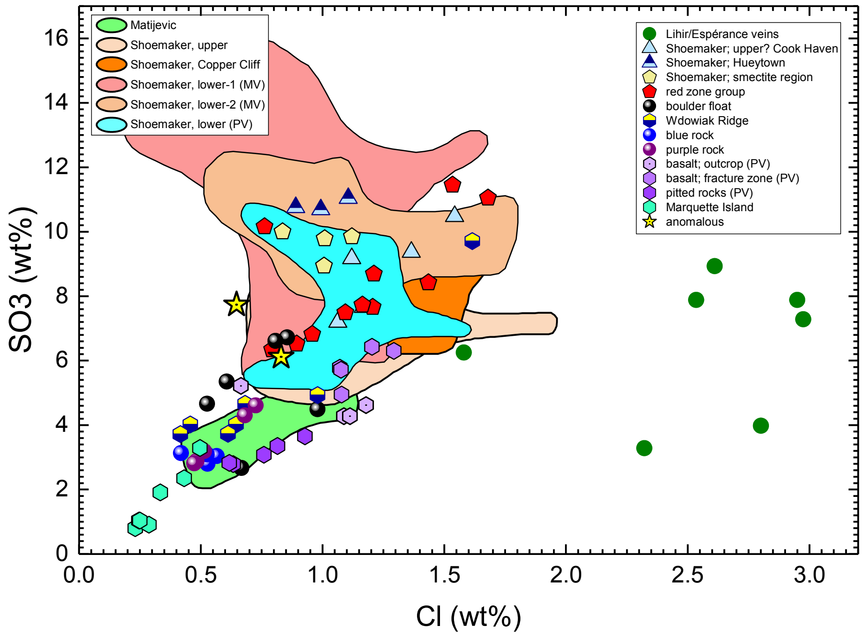

1553

1554 Figure 7.

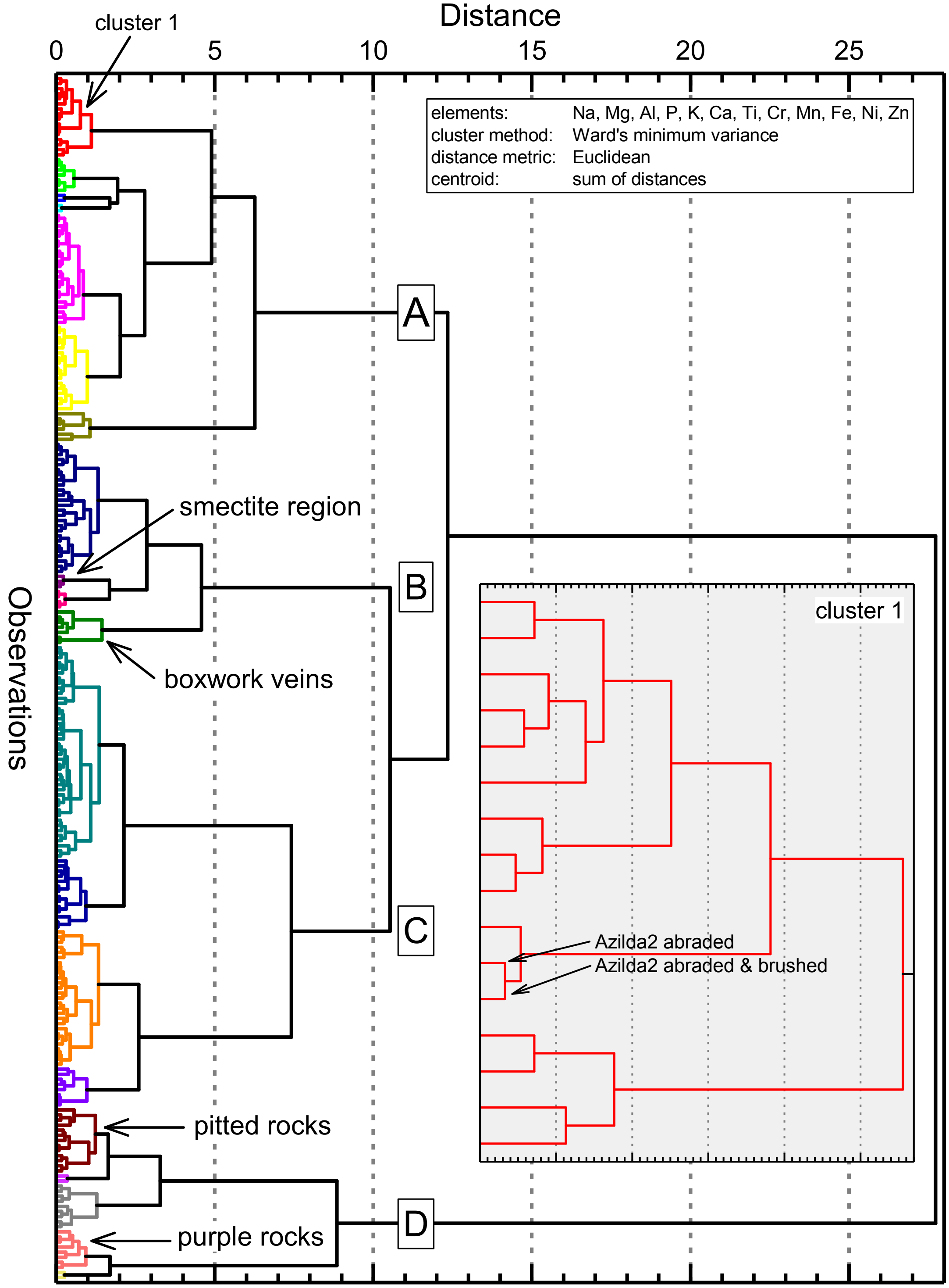
Distance
cluster 1
0
5
10
15
20
25
elements: Na, Mg, Al, P, K, Ca, Ti, Cr, Mn, Fe, Ni, Zn
cluster method: Ward's minimum variance
distance metric: Euclidean
centroid: sum of distances
A
B
C
D
smectite region
boxwork veins
pitted rocks
purple rocks
Observations
cluster 1
Azilda2 abraded
Azilda2 abraded & brushed

Figure 8.

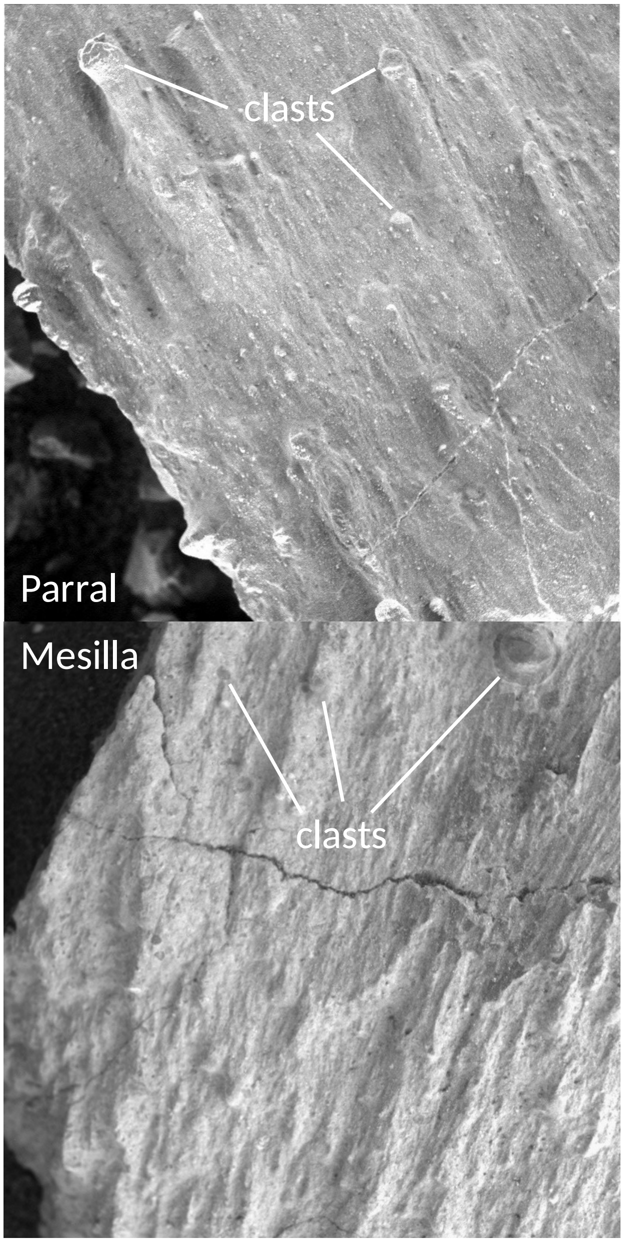

Figure 9.

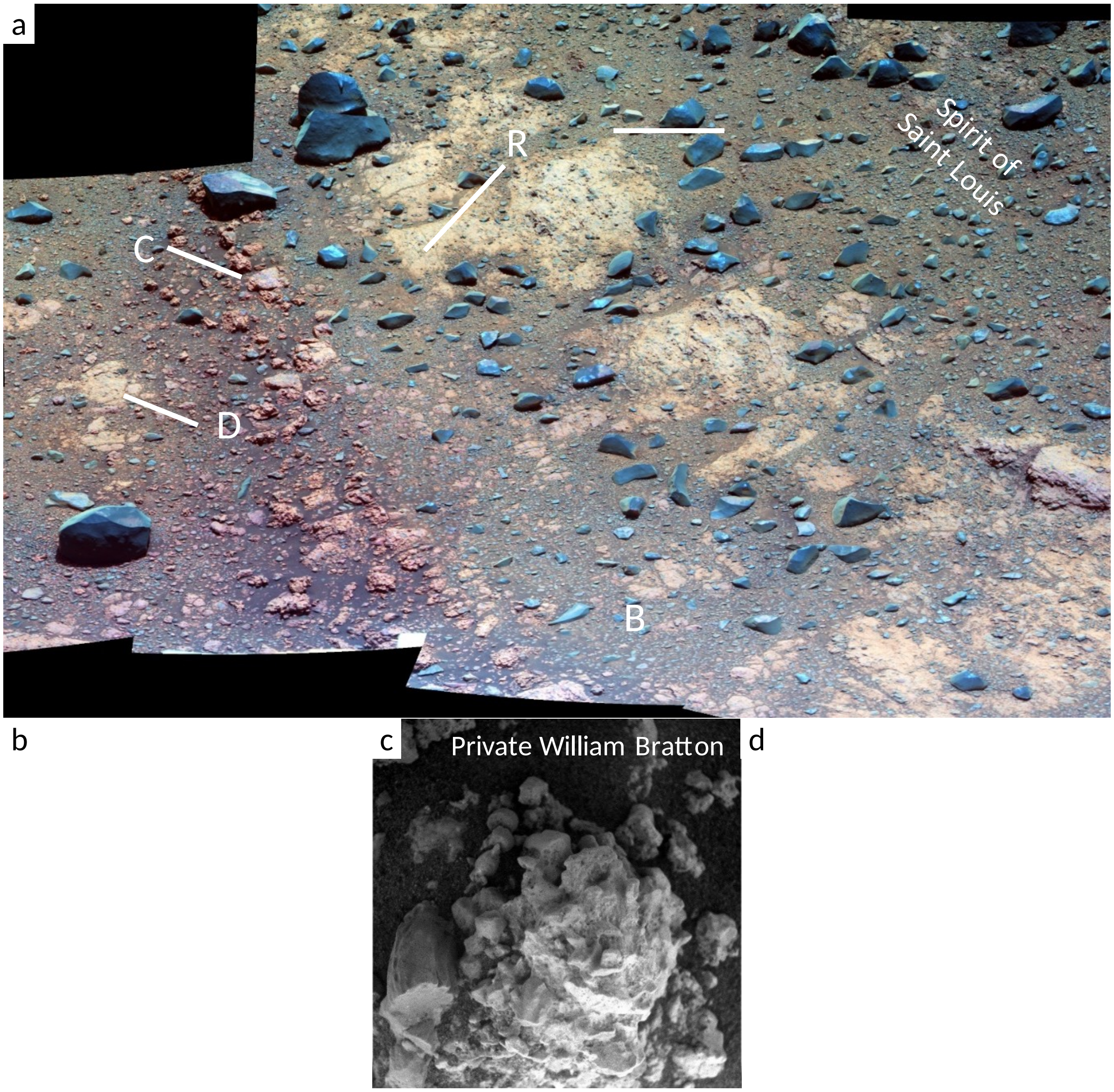

Figure 10.

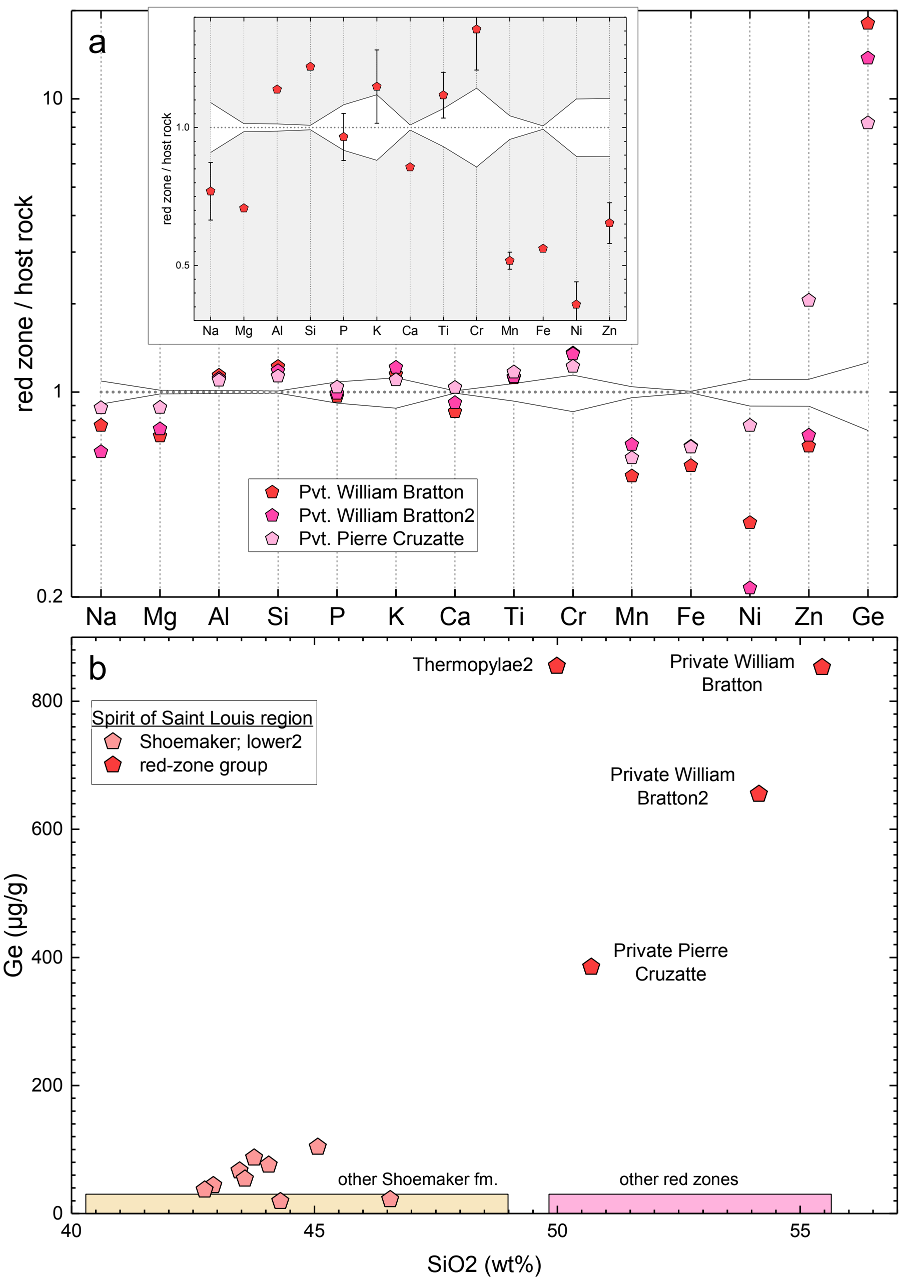
a
b
red zone / host rock
Na
Mg
Al
Si
P
K
Ca
Ti
Cr
Mn
Fe
Ni
Zn
Ge
Pvt. William Bratton
Pvt. William Bratton2
Pvt. Pierre Cruzatte
Thermopylae2
Private William Bratton
Private William Bratton2
Private Pierre Cruzatte
Spirit of Saint Louis region
Shoemaker; lower2
red-zone group
other Shoemaker fm.
other red zones
Ge (µg/g)
SiO2 (wt%)

Figure 11.

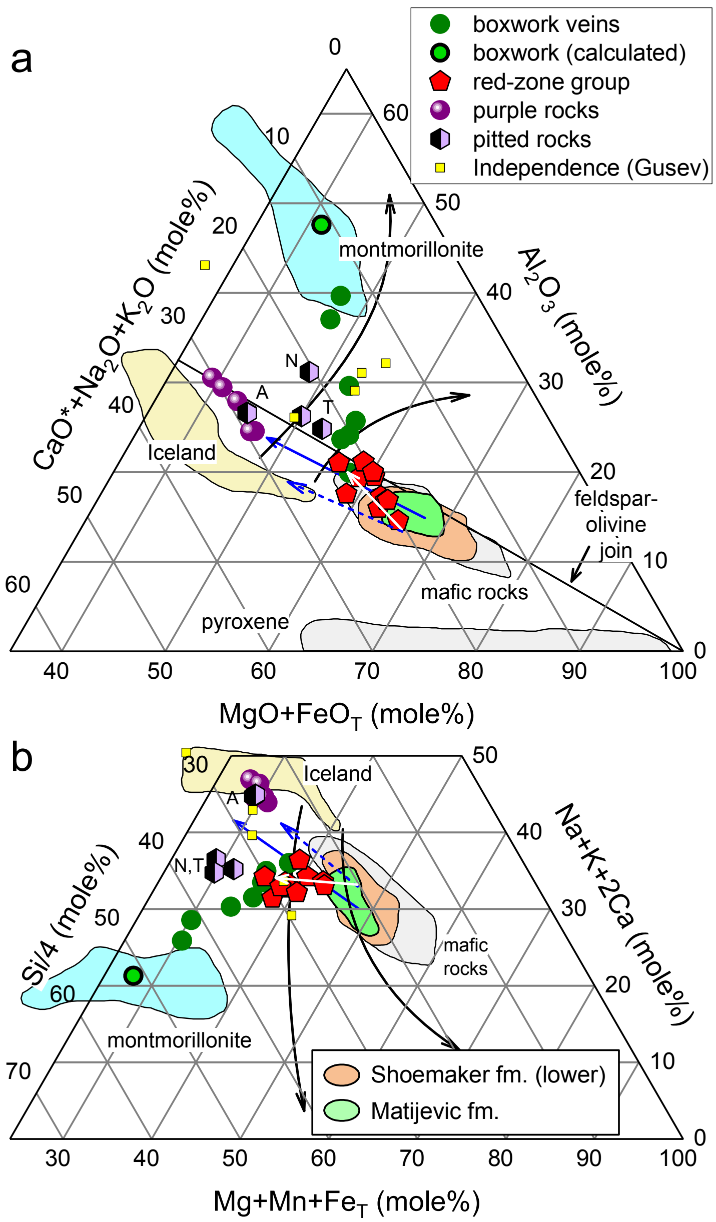

1563

1564 Figure 12.

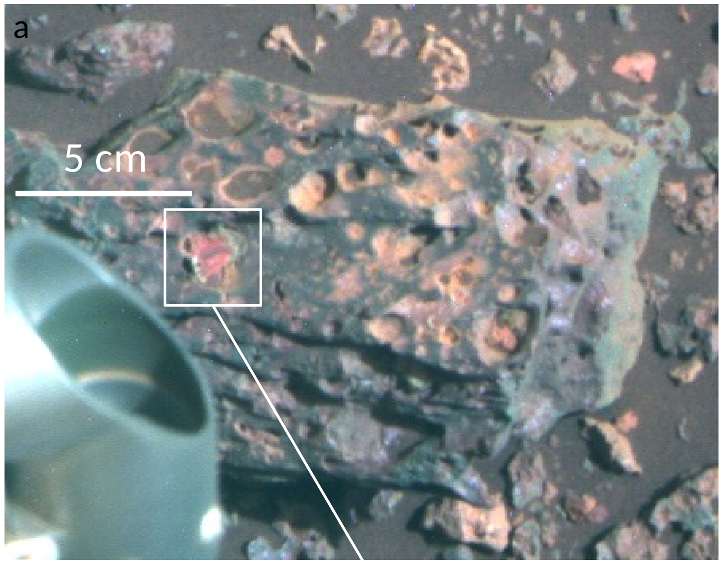

b

Figure 13.

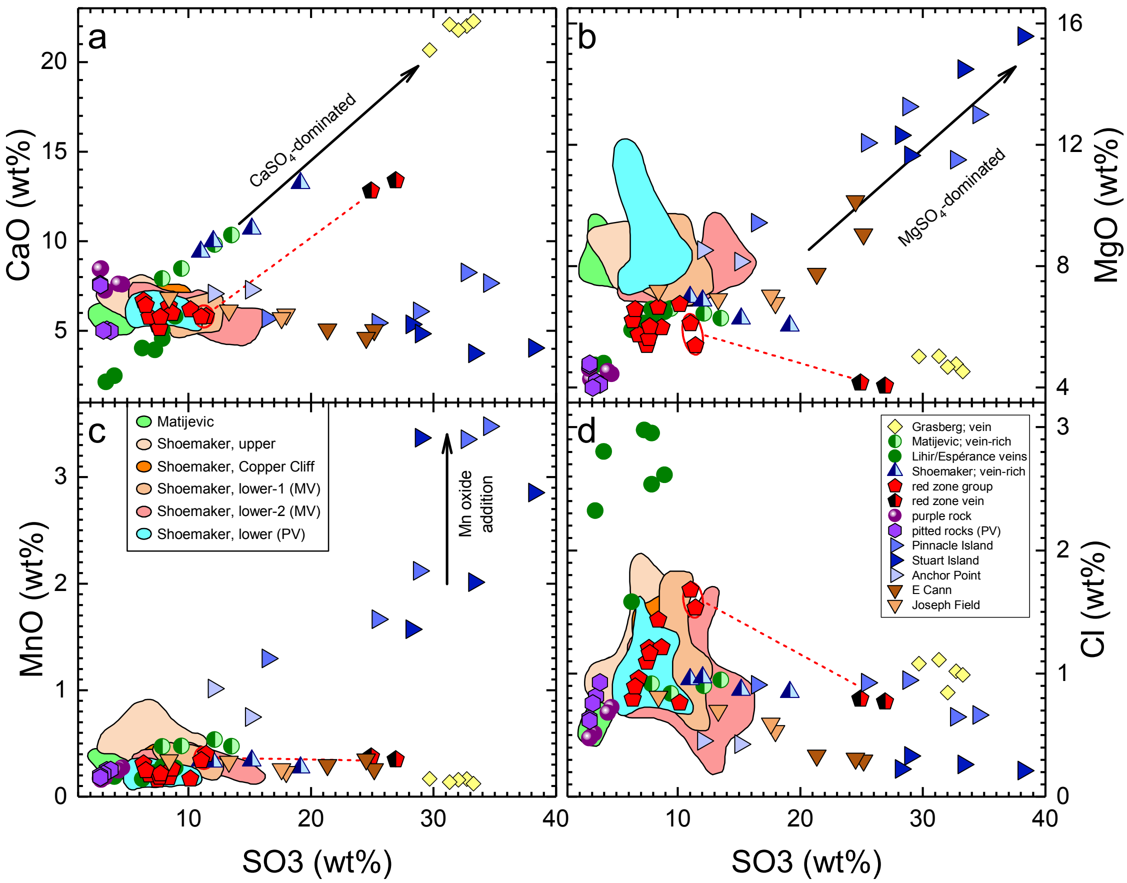
a
b
c
d
CaO (wt%)
MgO (wt%)
MnO (wt%)
Cl (wt%)
SO3 (wt%)
SO3 (wt%)
CaSO4-dominated
MgSO4-dominated
Mn oxide addition
Matijevic
Shoemaker, upper
Shoemaker, Copper Cliff
Shoemaker, lower-1 (MV)
Shoemaker, lower-2 (MV)
Shoemaker, lower (PV)
Grasberg; vein
Matijevic; vein-rich
Lihir/Espérance veins
Shoemaker; vein-rich
red zone group
red zone vein
purple rock
pitted rocks (PV)
Pinnacle Island
Stuart Island
Anchor Point
E Cann
Joseph Field

Figure 14.

a

c

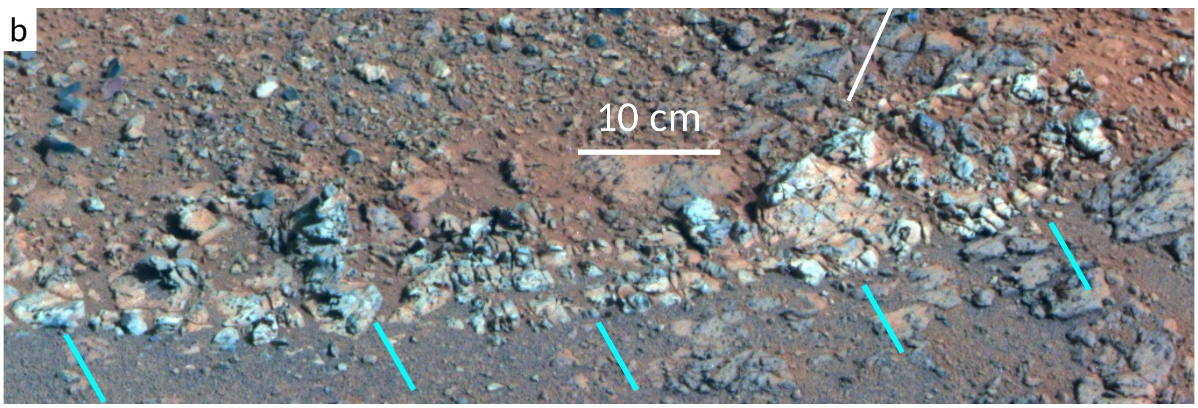

Figure 15.

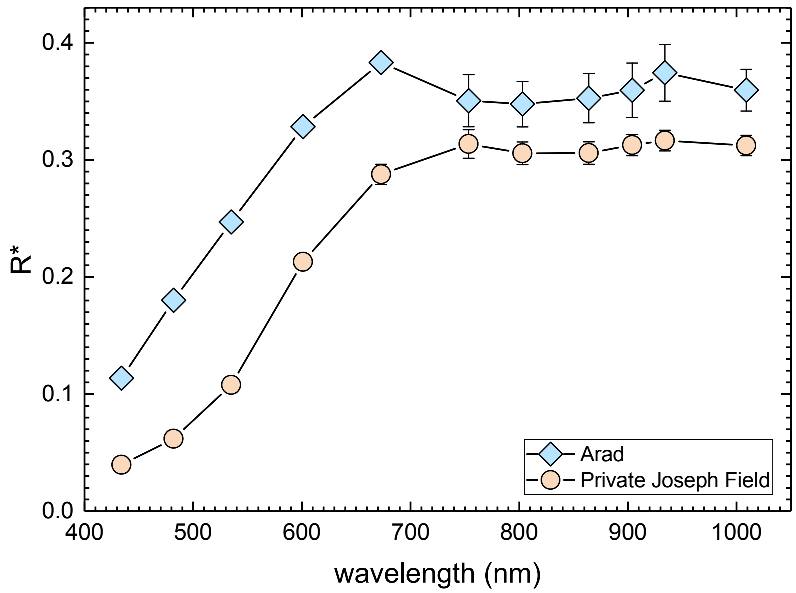
0.4
0.3
0.2
0.1
0.0
R*
400
500
600
700
800
900
1000
wavelength (nm)
Arad
Private Joseph Field

Figure 16.

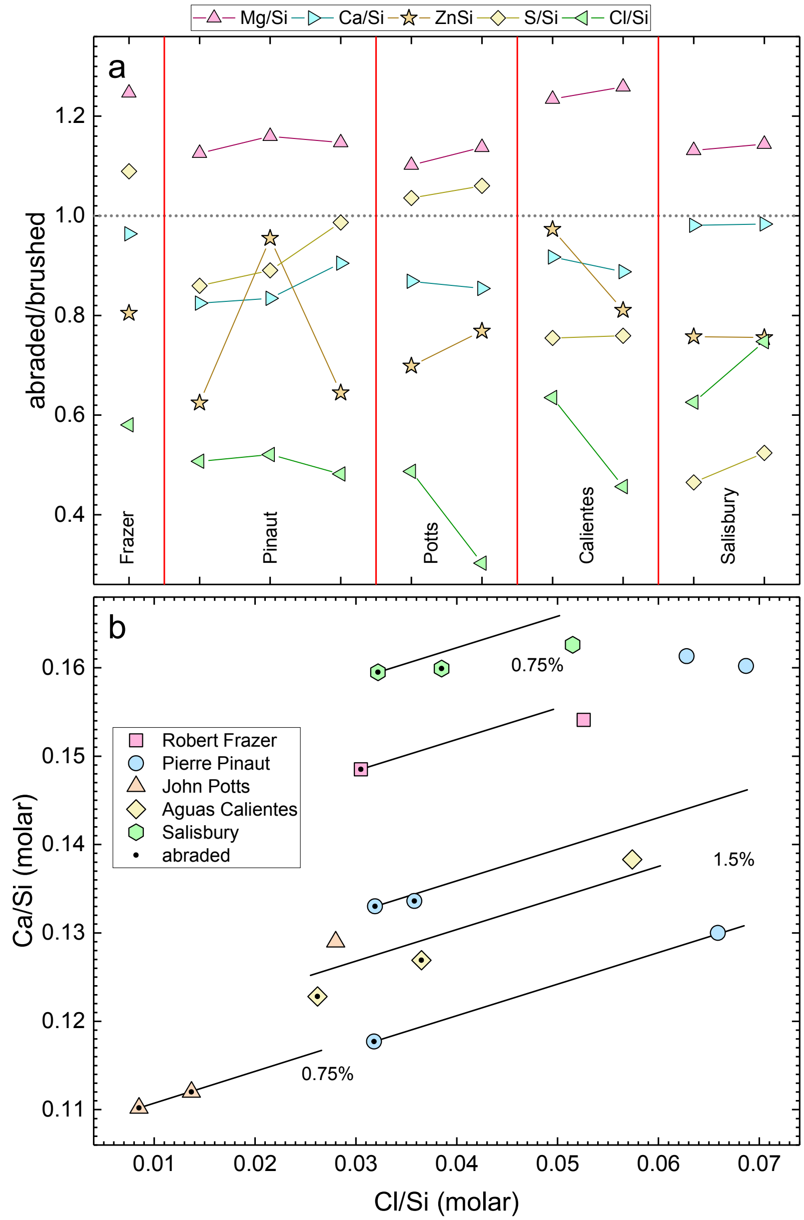

Mg/Si
Ca/Si
ZnSi
S/Si
Cl/Si
a
abraded/brushed
1.2
1.0
0.8
0.6
0.4
Frazer
Pinaut
Potts
Calientes
Salisbury
b
Ca/Si (molar)
0.16
0.15
0.14
0.13
0.12
0.11
0.75%
1.5%
0.75%
Robert Frazer
Pierre Pinaut
John Potts
Aguas Calientes
Salisbury
abraded
0.01
0.02
0.03
0.04
0.05
0.06
0.07
Cl/Si (molar)

Figure 17.

a b

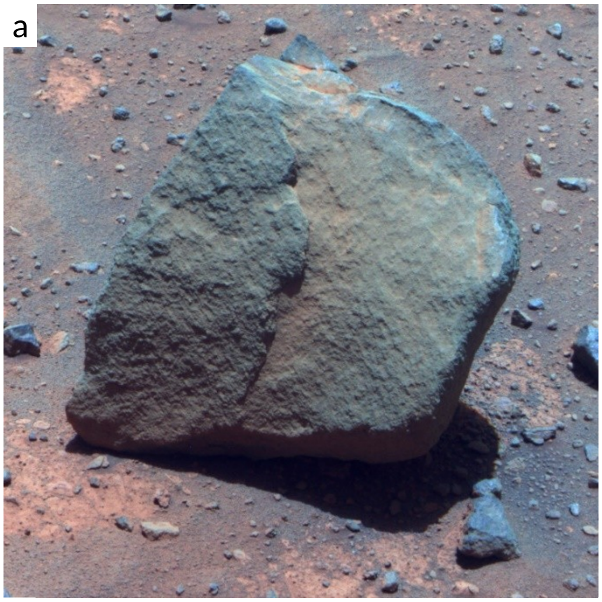

c d

Figure 18

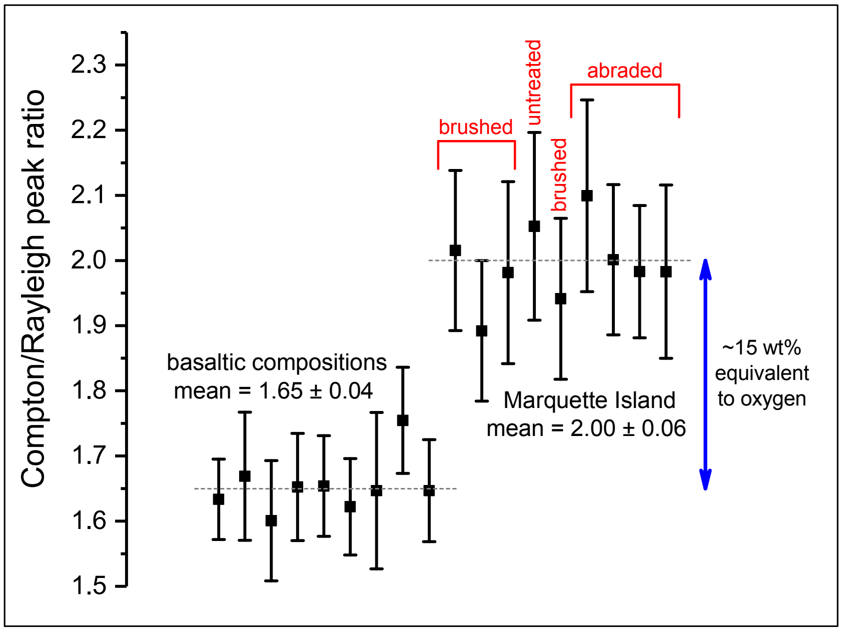
Compton/Rayleigh peak ratio
2.3
2.2
2.1
2.0
1.9
1.8
1.7
1.6
1.5
basaltic compositions
mean = 1.65 ± 0.04
brushed
untreated
brushed
abraded
Marquette Island
mean = 2.00 ± 0.06
~15 wt%
equivalent
to oxygen

Figure 19.

Geology and Geochemistry of Noachian Bedrock and Alteration Events, Meridiani Planum, Mars: MER Opportunity Observations - Supplementary Locator Maps

David W. Mittlefehldt[1], Ralf Gellert[2], Scott vanBommel[2,3], Raymond E. Arvidson[3], James W. Ashley[4], Benton C. Clark[5], Larry S. Crumpler[6], William H. Farrand[5], Matthew P. Golombek[4], John A. Grant[7], Richard V. Morris[1], Christian Schröder[8]

[1]Mail code XI3, Astromaterials Research Office, NASA/Johnson Space Center, Houston, Texas 77058, USA.

[2]Department of Physics, University of Guelph, Guelph, ON N1G2W1, Canada.

[3]Department of Earth and Planetary Sciences, Washington University in Saint Louis, Saint Louis, Missouri 63130, USA.

[4]Jet Propulsion Laboratory, California Institute of Technology, Pasadena, California 91109, USA.

[5]Space Science Institute, 4765 Walnut St., Suite B, Boulder, Colorado 80301, USA.

[6]New Mexico Museum of Natural History and Science, 1801 Mountain Rd NW, Albuquerque, New Mexico 87104, USA.

[7]Smithsonian Institution, NASM CEPS, 6th at Independence Ave. SW, Washington, DC 20560, USA.

[8]Biological and Environmental Sciences, University of Stirling, Stirling FK9 4LA, Scotland, UK.

Journal of Geophysical Research: Planets
submitted: 31 March 2021

This supplement includes locator images for targets discussed in the paper. Figures L01-L10 include locations of Pancam images, named targets, locations of some specific rock types and formal and informal geographic names.

Figures L12-L21 include locations for APXS targets from Table 1 identified by Sol and rock/soil type. Rock types are simplified from the text. The Shoemaker formation is broken into upper and lower. The latter includes lower-1 and lower-2 from Marathon Valley, and lower from Perseverance Valley. Shoemaker upper includes those from Cape Tribulation and the three members identified on Cape York. The Matijevic formation includes the matrix, spherule-rich and veneer targets. Basaltic rocks in Perseverance Valley includes those from inside and outside the fracture zone. Grasberg formation targets are shown for completeness. Composite soils are shown, but not the dark sand and bright soil.

Base map images taken from HiRISE-based mosaic of Endeavour crater (Parker et al., 2012). Rover track shown in white.

Reference:

Parker, T. J., Golombek, M. P., Calef, F. J., & Hare, T. M. (2012). High-resolution basemaps for localization, mission planning, and geologic mapping at Meridiani Planum and Gale crater. Paper presented at 43rd Lunar and Planetary Science Conference, Abstract #2535, Houston, TX, USA.

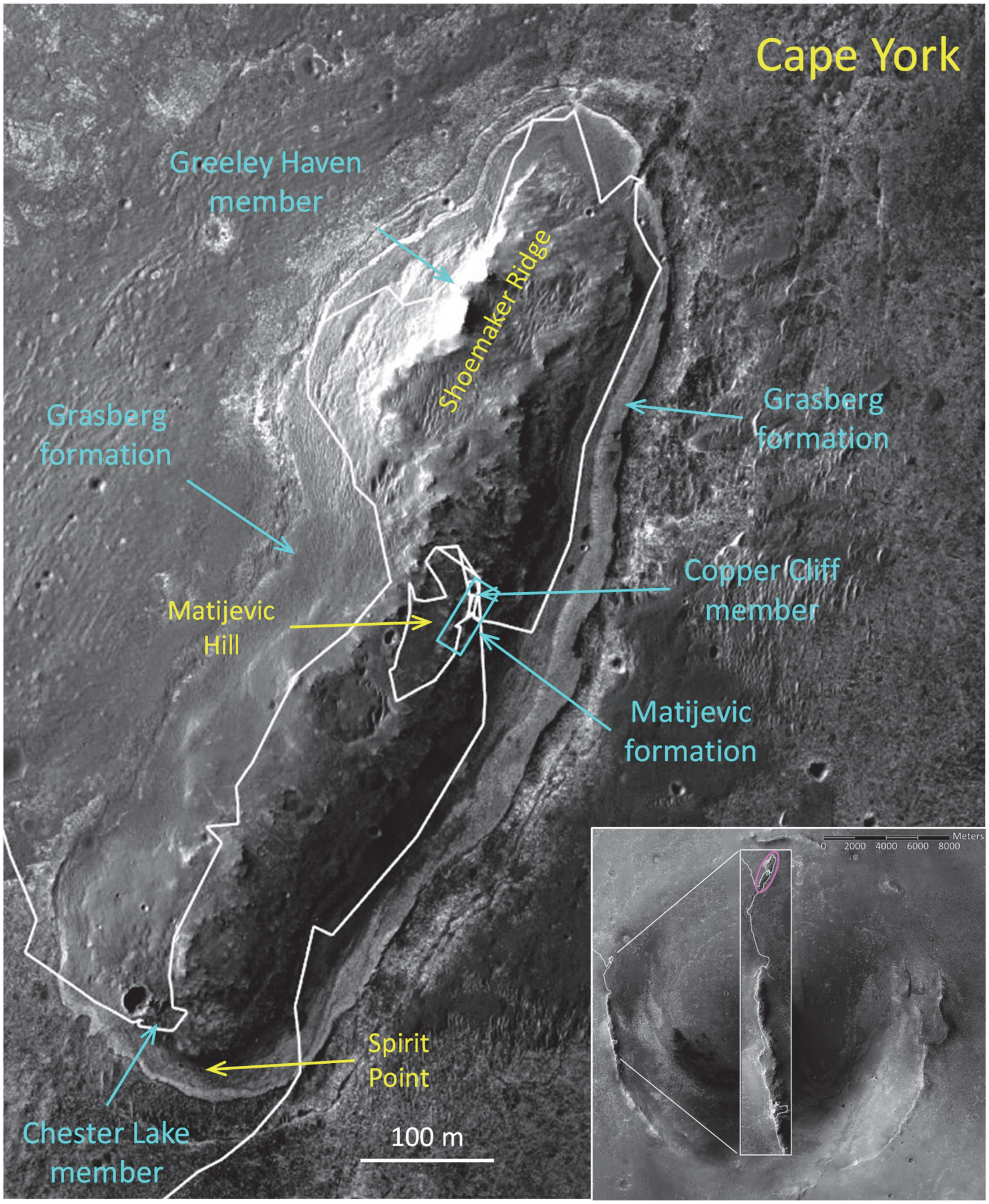

Figure L01. Locator image for Cape York features highlighting the appearance of the Grasberg formation as a surrounding bench, the general location of the Matijevic formation (box), and the locations where the Copper Cliff, Chester Lake and Greely Haven members of the Shoemaker formation were defined. Rover track shown in white. Images from HiRISE-based mosaic of Endeavour Crater (inset).

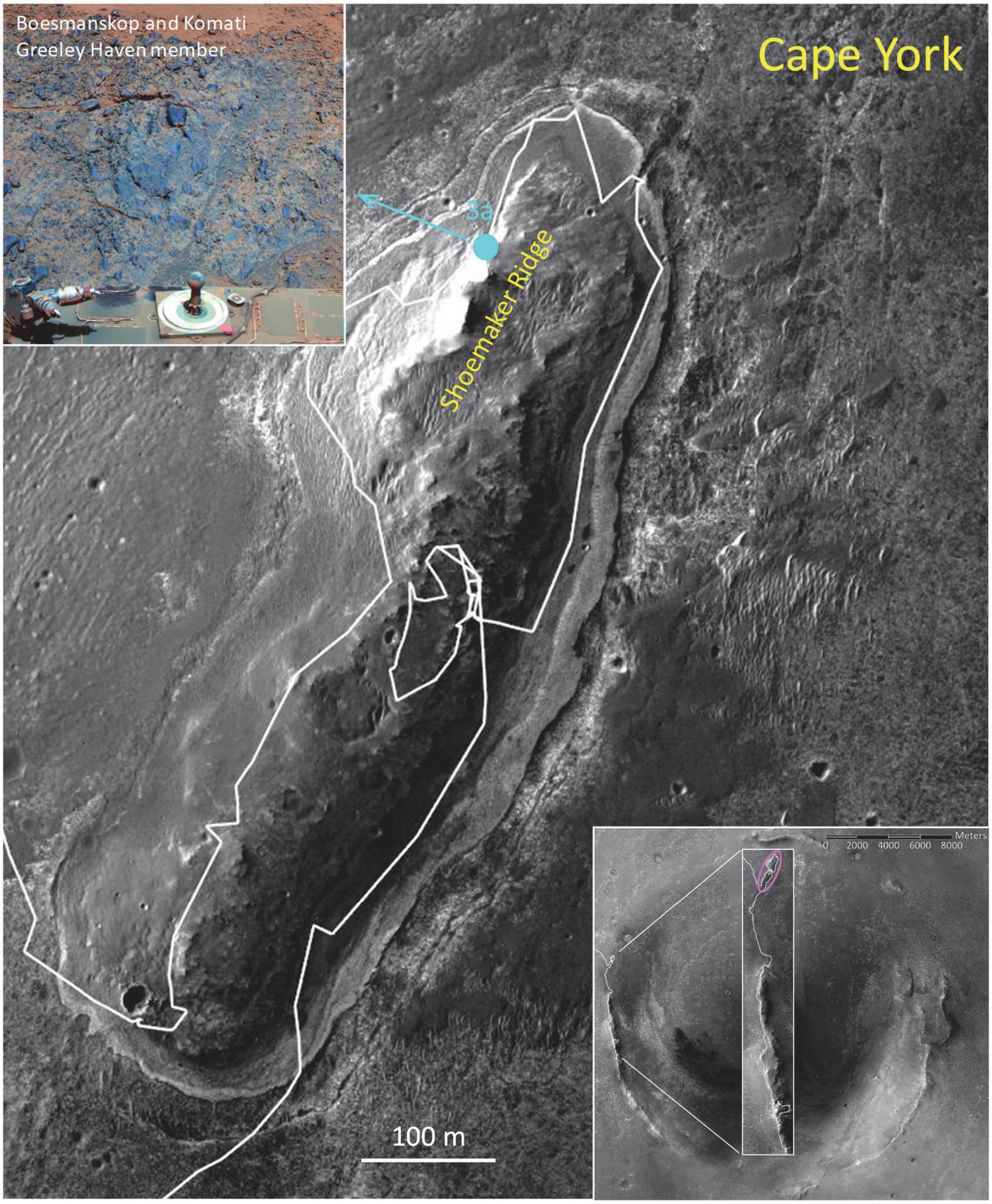

Figure L02. Locator image for Cape York showing the location of Fig. 3a (inset, upper left) from the paper. Rover track shown in white. Images from HiRISE-based mosaic of Endeavour Crater (inset, lower right).

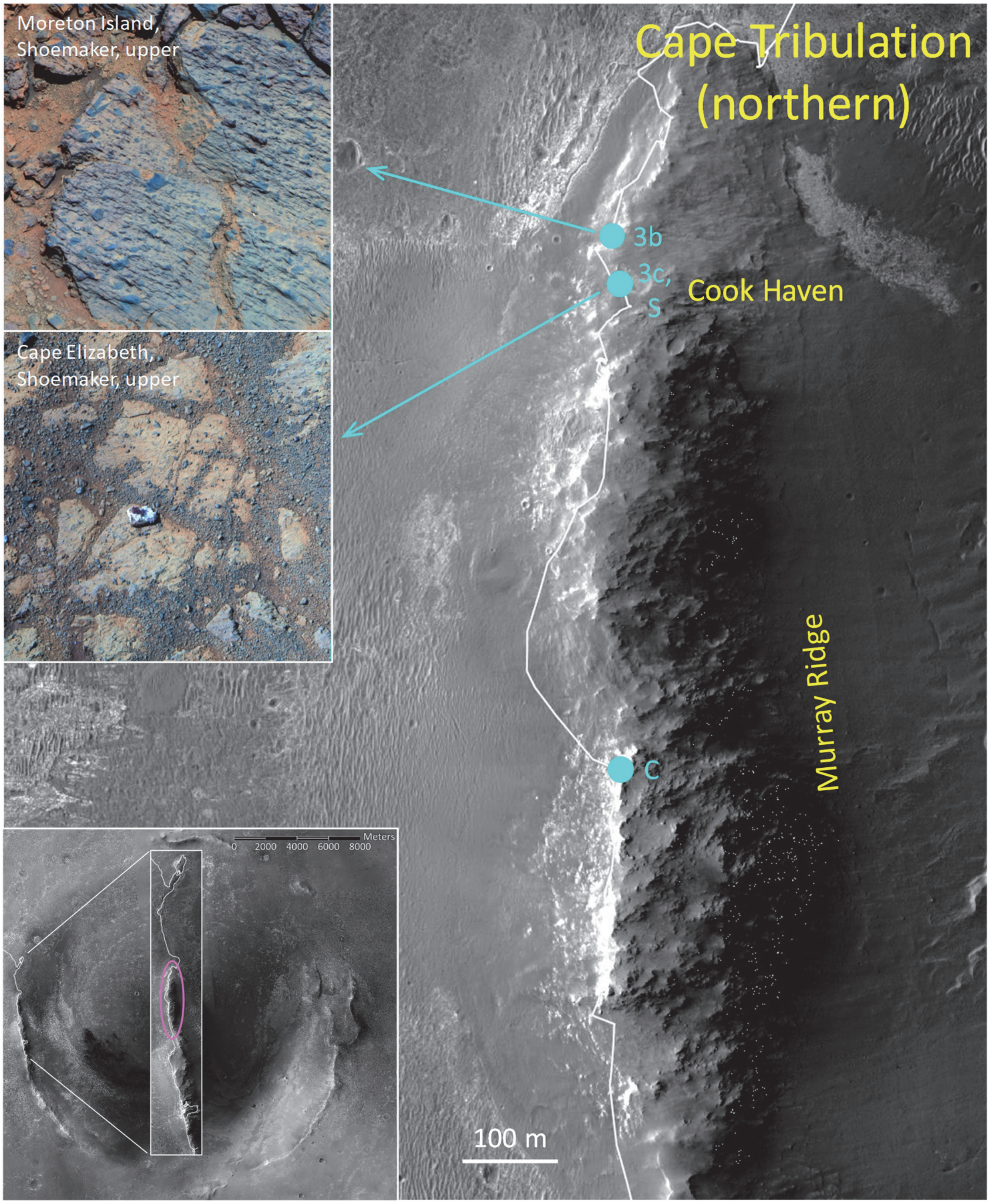

Figure L03. Locator image for the Murray Ridge region on Cape Tribulation showing the locations of Figs. 3b (inset, upper left) and 3c (inset, center left) from the paper. Also shown are locations of upper Shoemaker targets Sledge Island (S) at Cook Haven and Sarcobatus Clast 2 (C). Rover track shown in white. Images from HiRISE-based mosaic of Endeavour Crater (inset, lower left).

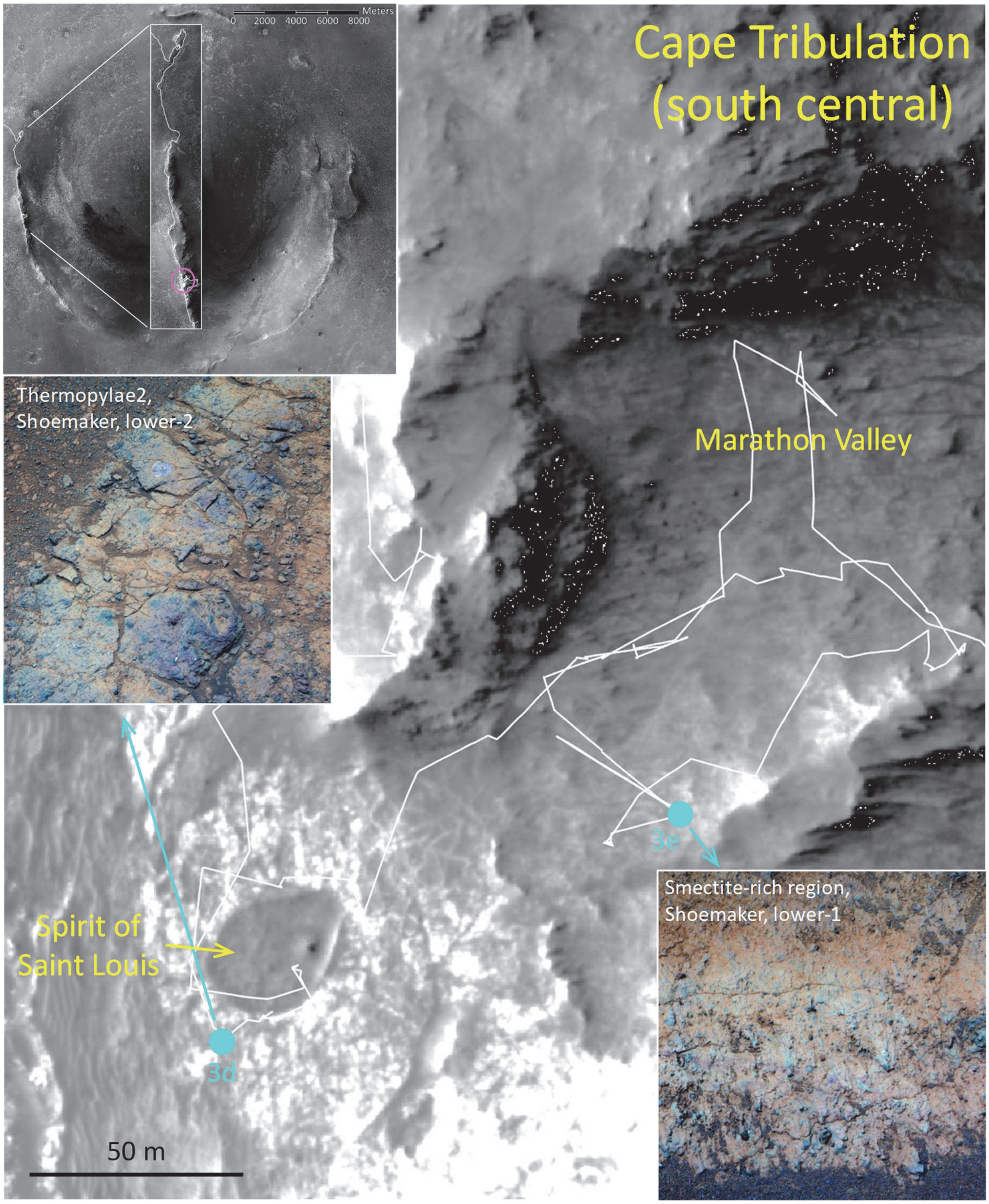

Figure L04. Locator image for the Marathon Valley region on Cape Tribulation showing the locations of Figs. 3d (inset, center left) and 3e (inset, lower right) from the paper. Rover track shown in white. Images from HiRISE-based mosaic of Endeavour Crater (inset, upper left).

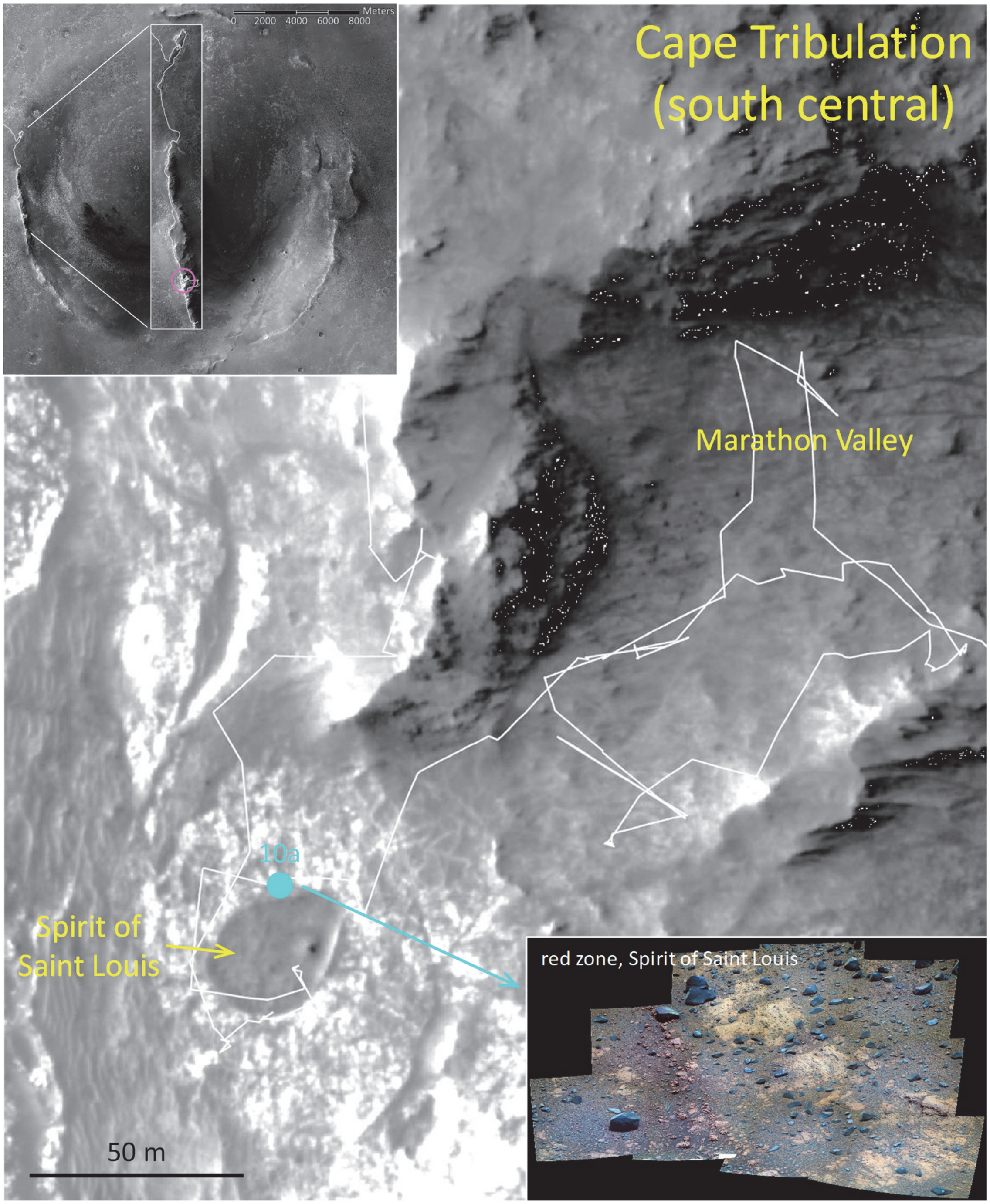

Figure L05. Locator image for the Marathon Valley region on Cape Tribulation showing the locations of Fig. 10A (inset, lower left) from the paper. Rover track shown in white. Images from HiRISE-based mosaic of Endeavour Crater (inset, upper left).

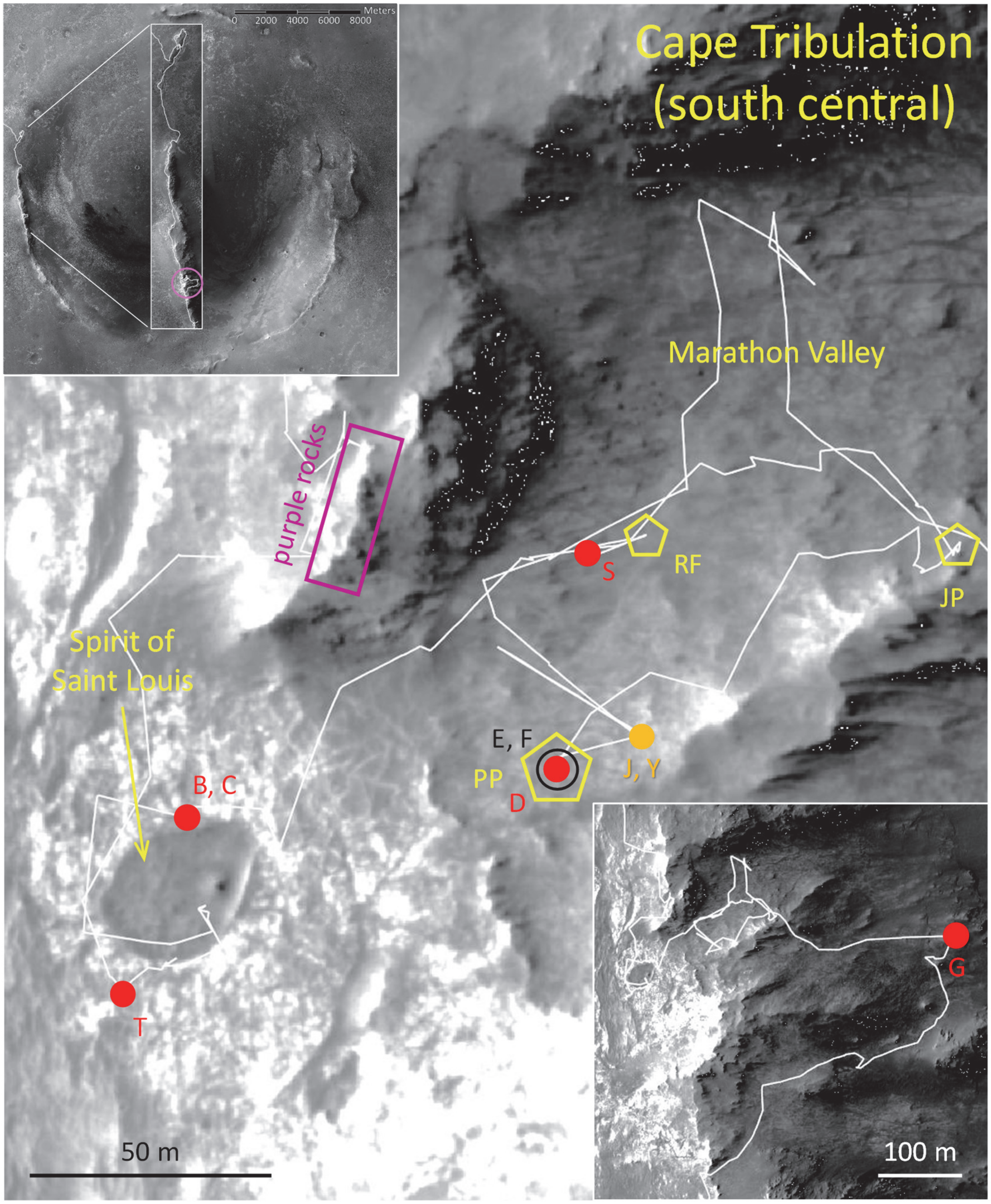

Figure L06. Locator image for the Marathon Valley region on Cape Tribulation showing the locations of red-zone group targets (red spots), the brushed and abraded target sets (yellow pentagons), sulfate-altered soil (black circle), purple rocks (box) and targets from the smectite region (gold spot). Abbreviations: B – Private William Bratton; C – Private Pierre Cruzatte; D – George Drouillard; G – Gasconade; S – Private Silas Goodrich; T – Thermopylae2; JP – Private John Potts; PP – Pierre Pinaut; RF – Private Robert Frazer; E – E Cann; F – Private Joseph Field; J – Jean Baptiste Deschamps; Y – York. Rover track shown in white. Images from HiRISE-based mosaic of Endeavour Crater (inset, upper left).

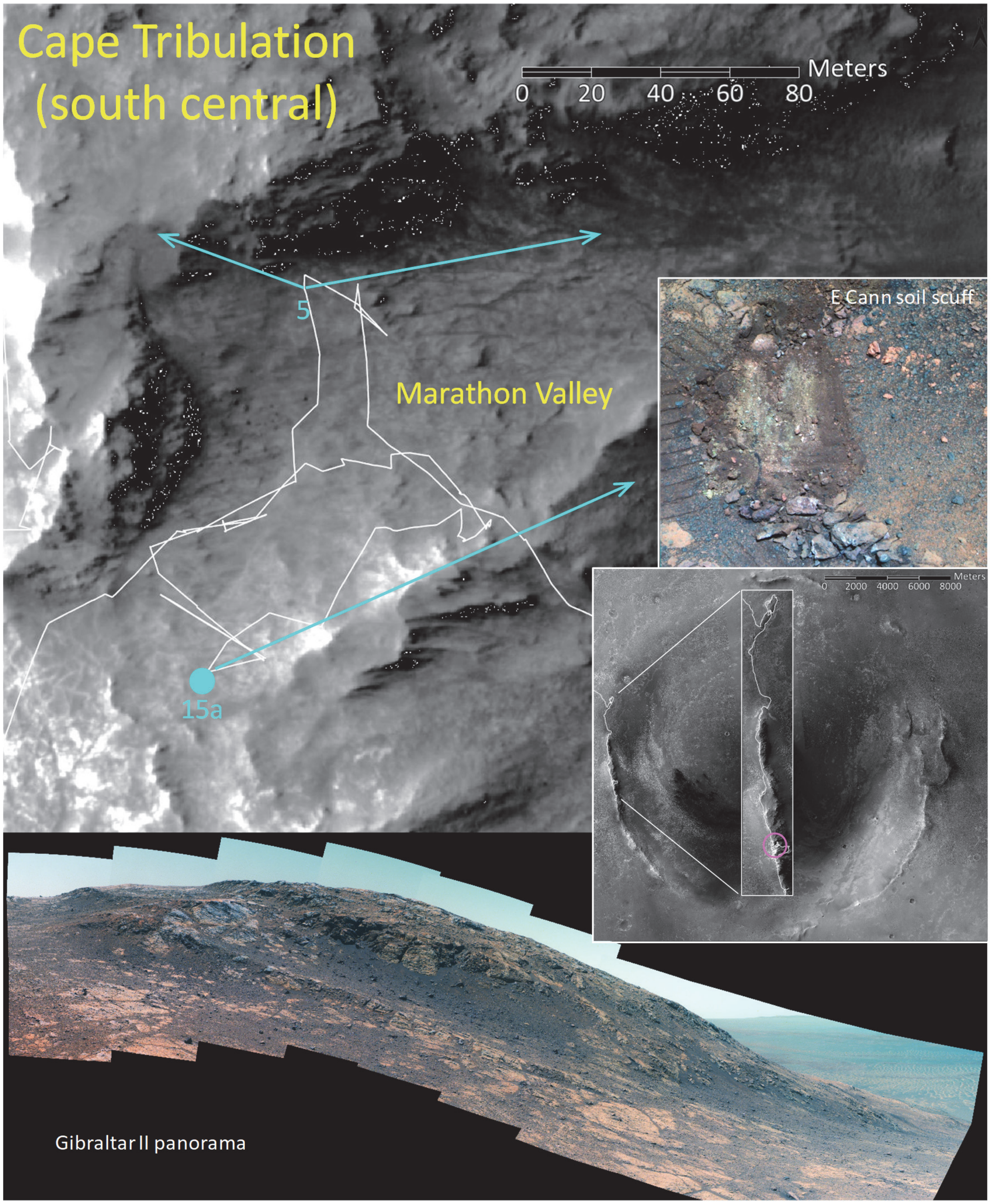

Figure L07. Locator image for the Marathon Valley region on Cape Tribulation showing the approximate view of the Gibraltar II panorama shown in Fig. 5 (below), and 15a (inset, right, upper) from the paper. Rover track shown in white. Images from HiRISE-based mosaic of Endeavour Crater (inset, right, lower).

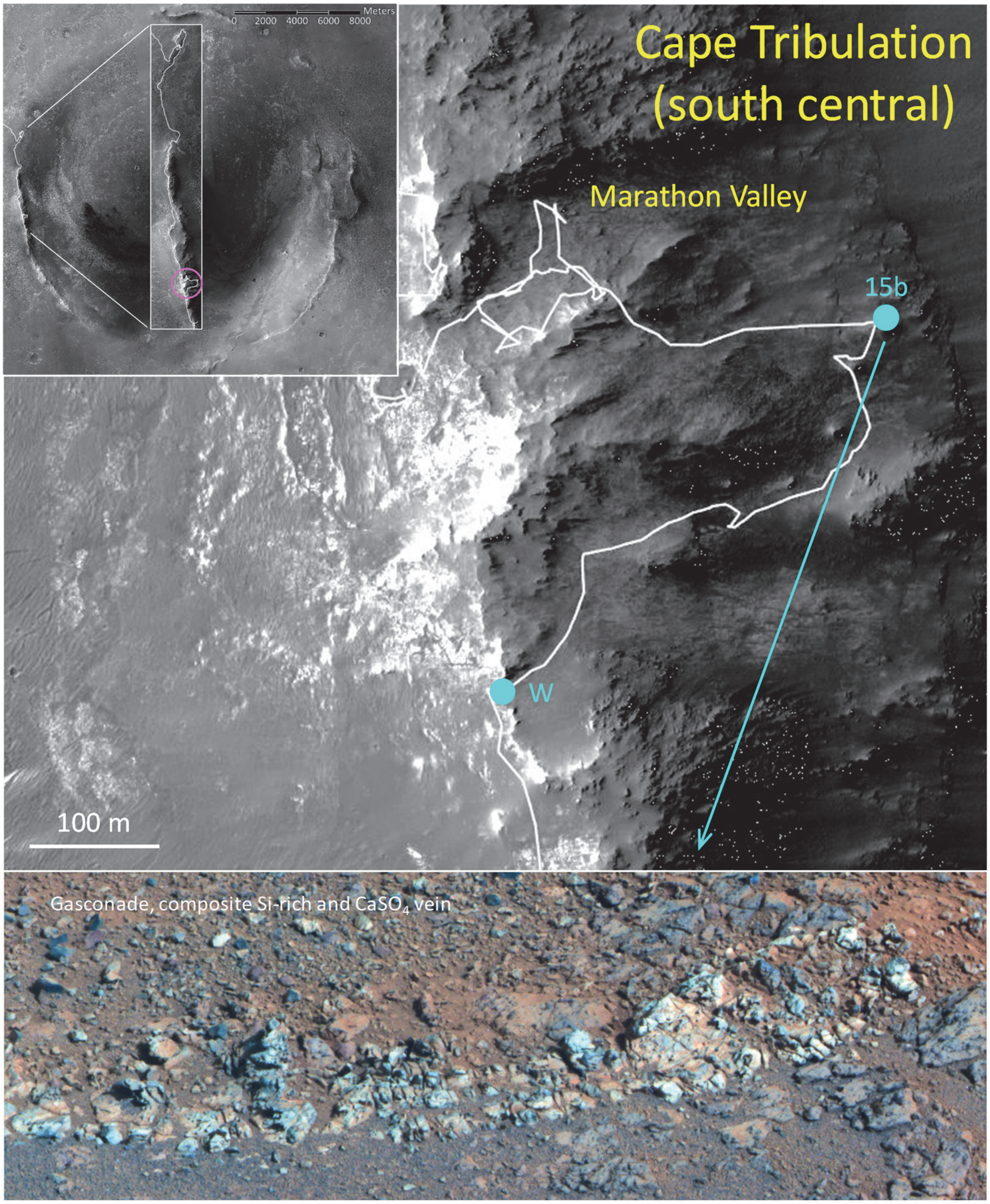

Figure L08. Locator image for the Marathon Valley region on Cape Tribulation showing the location of Fig. 15b (bottom) on Spirit Mound from the paper and the Waverly upper Shoemaker target (cyan spot). Rover track shown in white. Images from HiRISE-based mosaic of Endeavour Crater (inset, upper left).

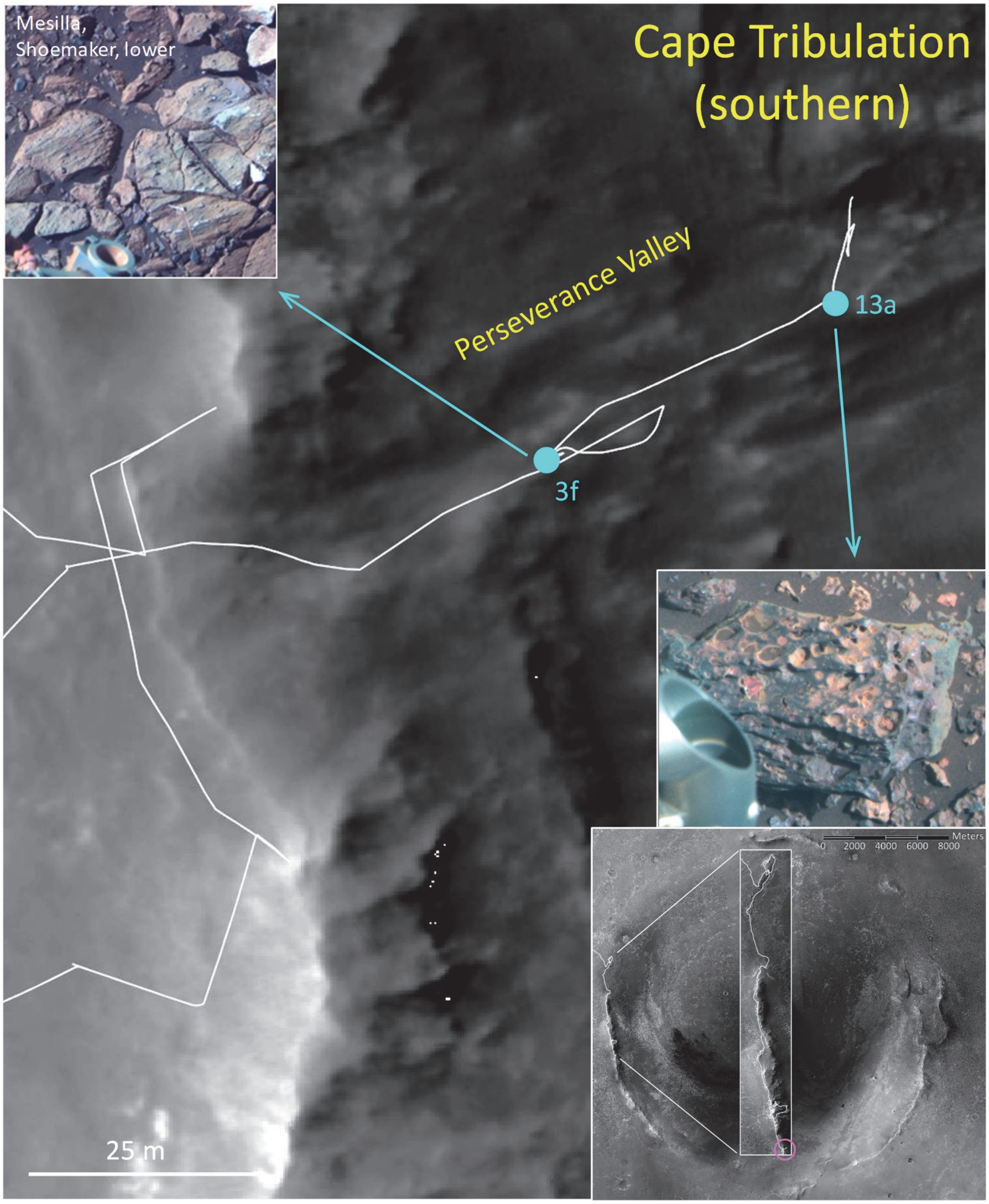

Figure L09. Locator image for the Perseverance Valley region on Cape Tribulation showing the locations of Fig. 3f (inset, upper left) and 13a (inset, center right) from the paper. Rover track shown in white. Images from HiRISE-based mosaic of Endeavour Crater (inset, lower right).

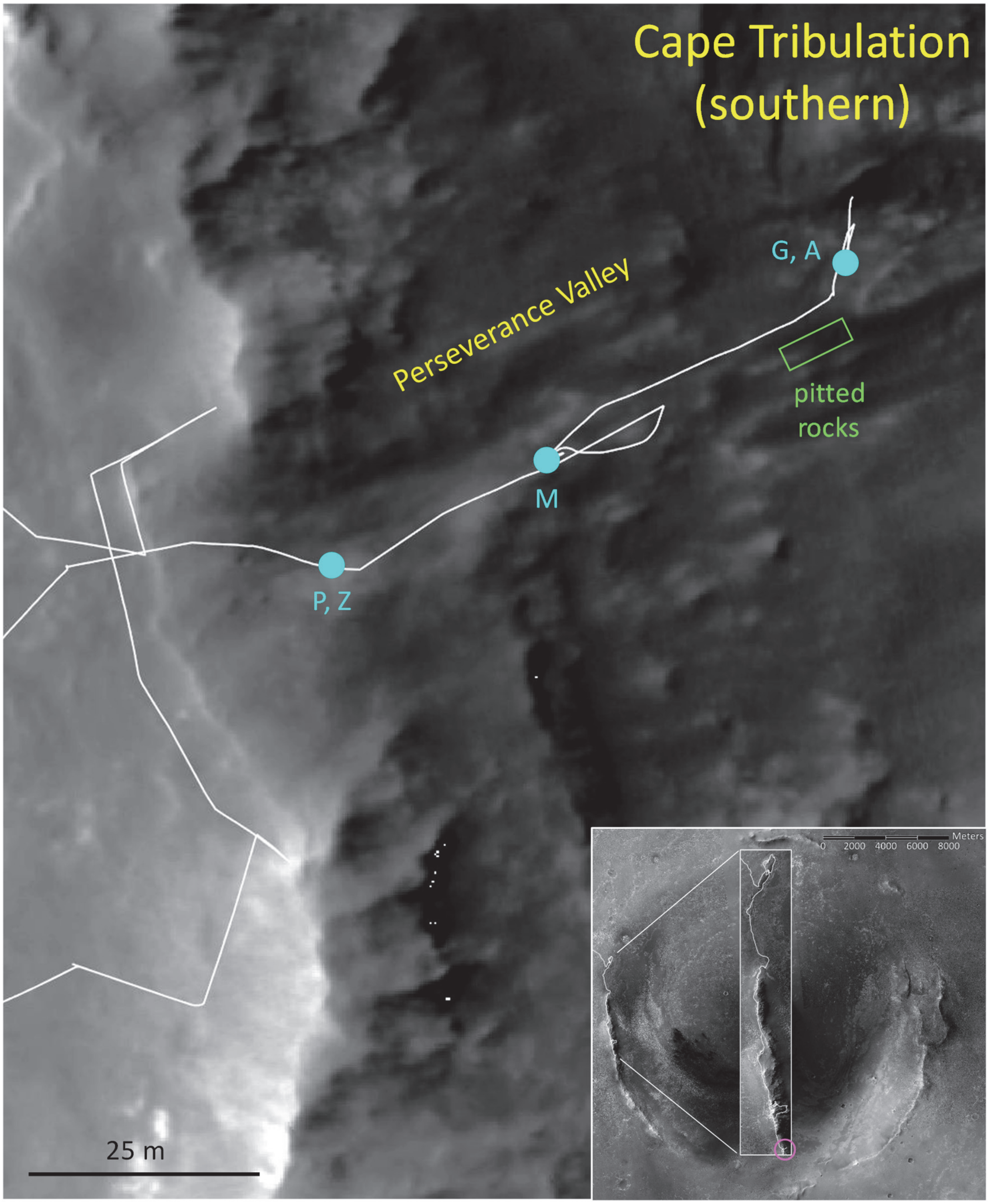

Figure L10. Locator image for the Perseverance Valley region on Cape Tribulation showing the locations of targets mentioned in the paper (cyan spots) and the area of the pitted rocks Allende, Nazas and Tomé (box). Abbreviations: P – Parral; Z – Zacatecas; M – Mesilla; A – Aguas Calientes; G – Guanajuato. Rover track shown in white. Images from HiRISE-based mosaic of Endeavour Crater (inset, lower right).

e

Legend for Figs. L11-L21

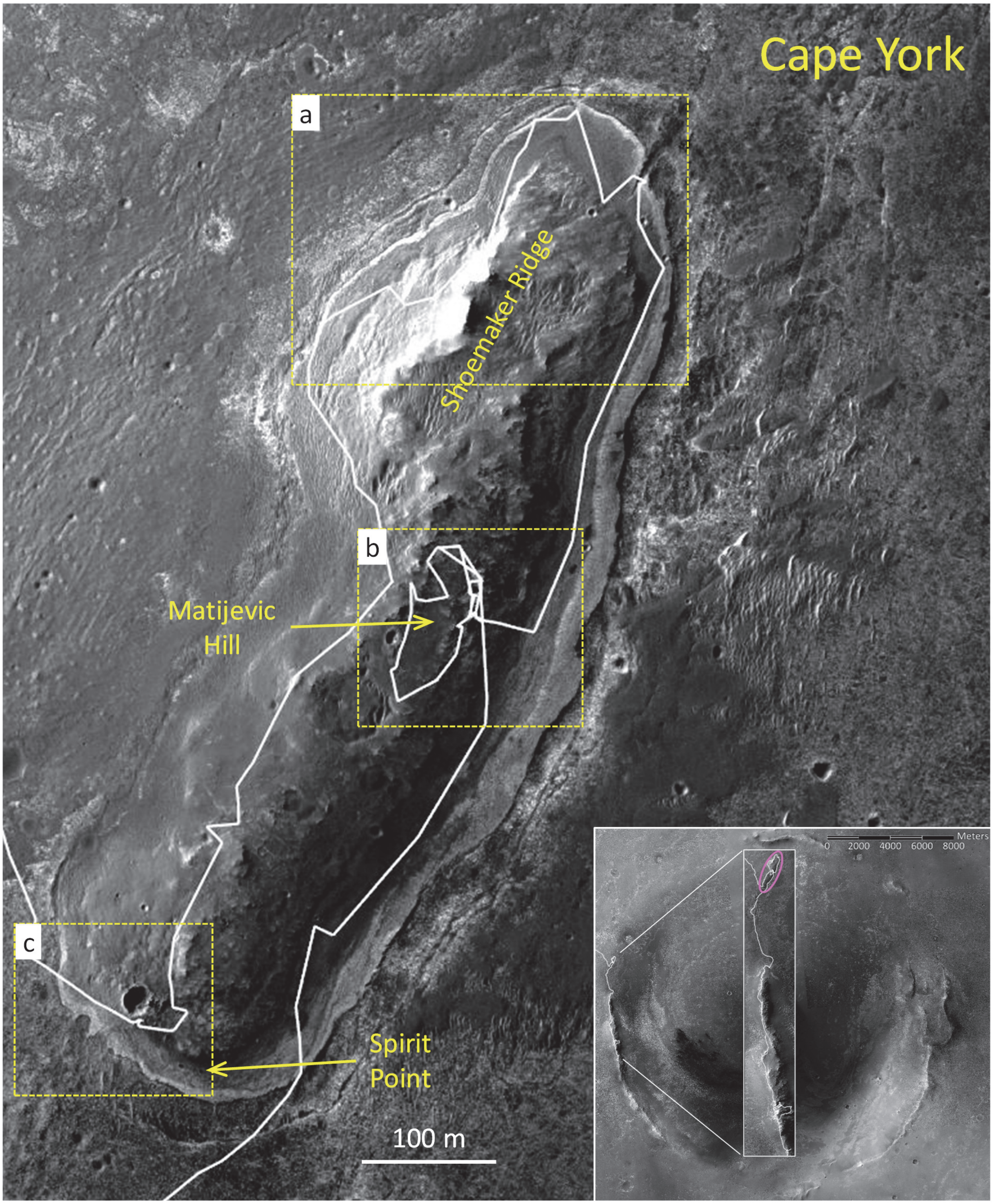

Figure L11. Locator image for the APXS targets identified by Sol and type; see legend on page 12.

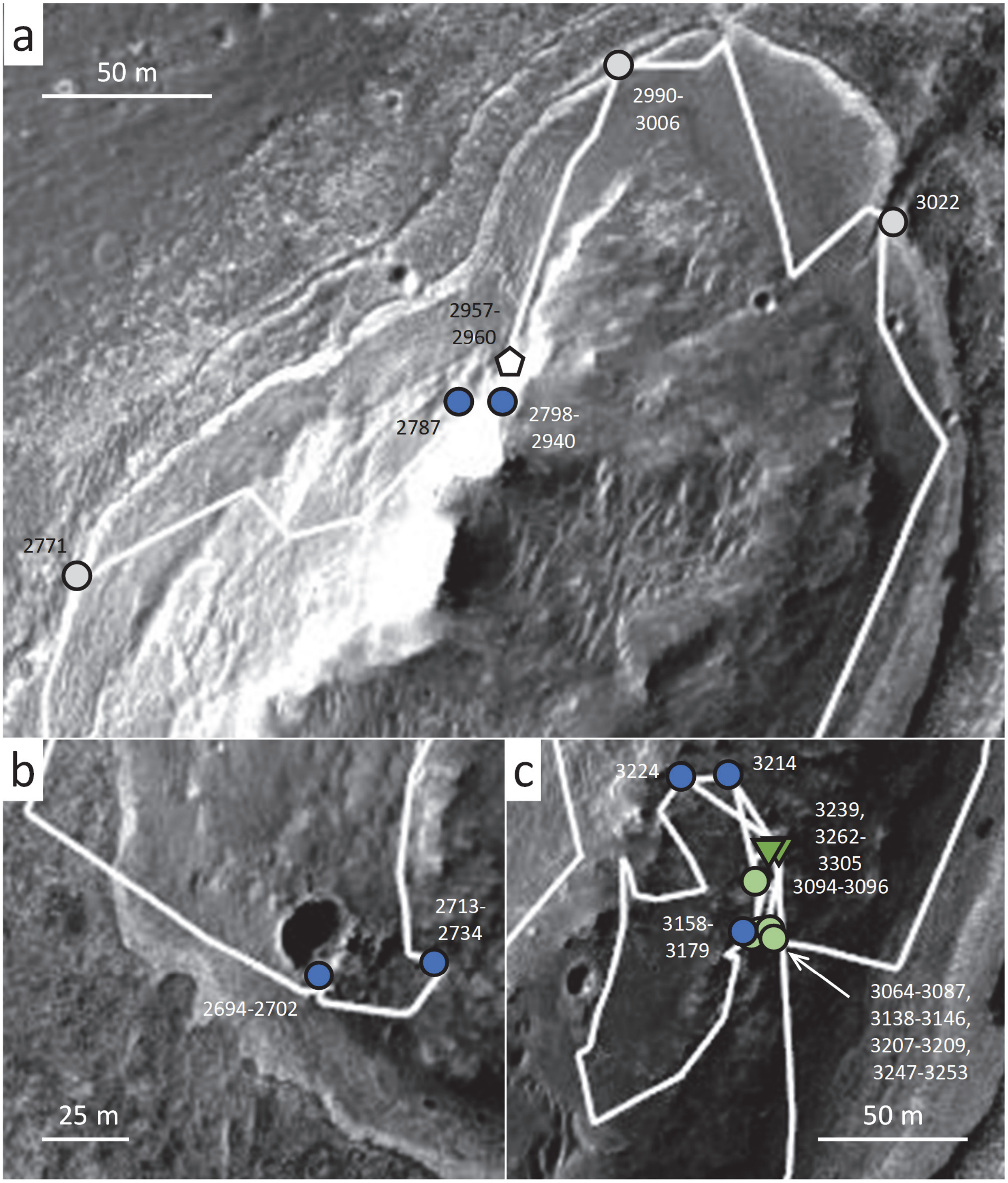

Figure L12. Locator image for the APXS targets identified by Sol and type; see legend on page 12.

Figure L13. Locator image for the APXS targets identified by Sol and type; see legend on page 12.

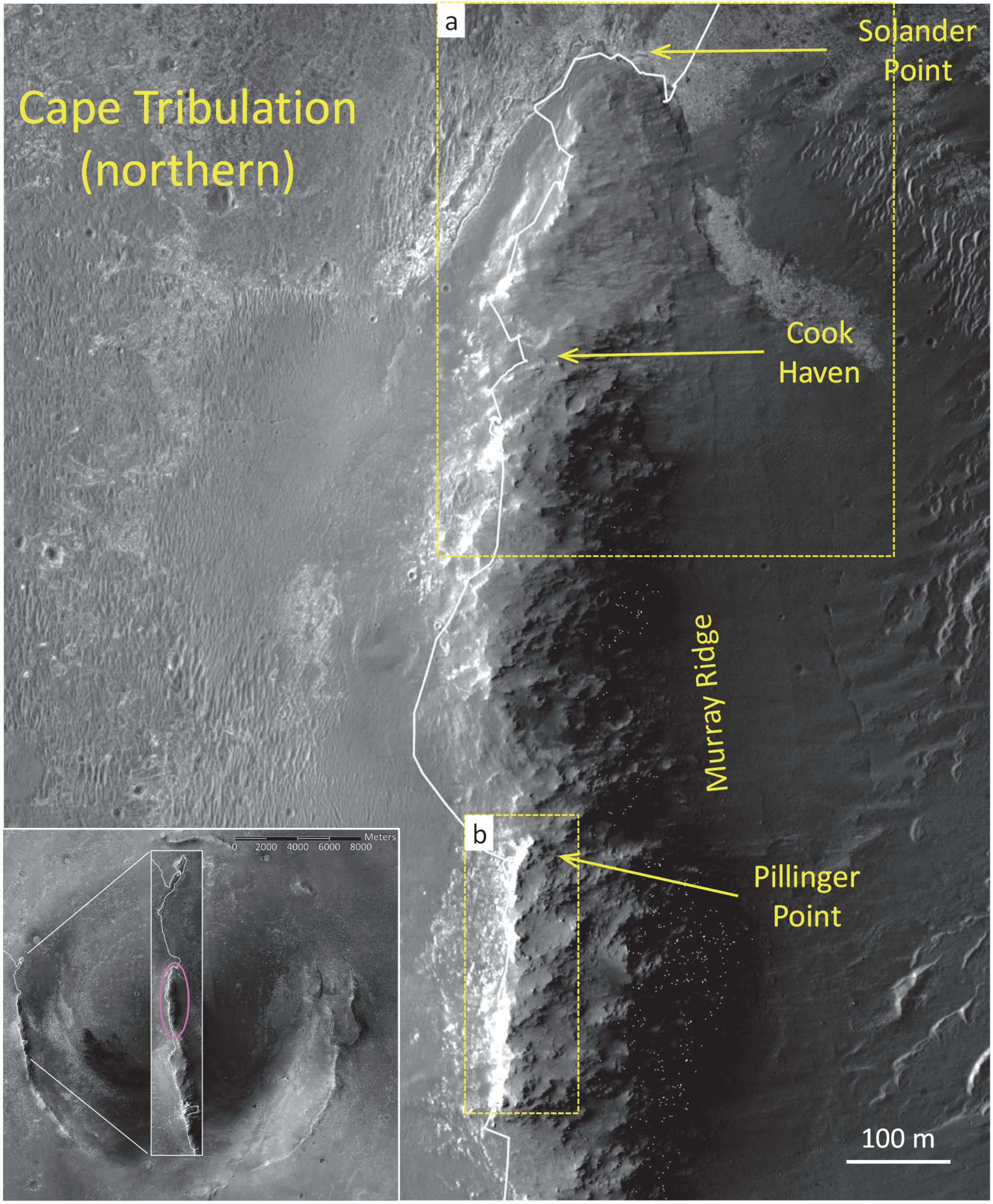

Figure L14. Locator image for the APXS targets identified by Sol and type; see legend on page 12.

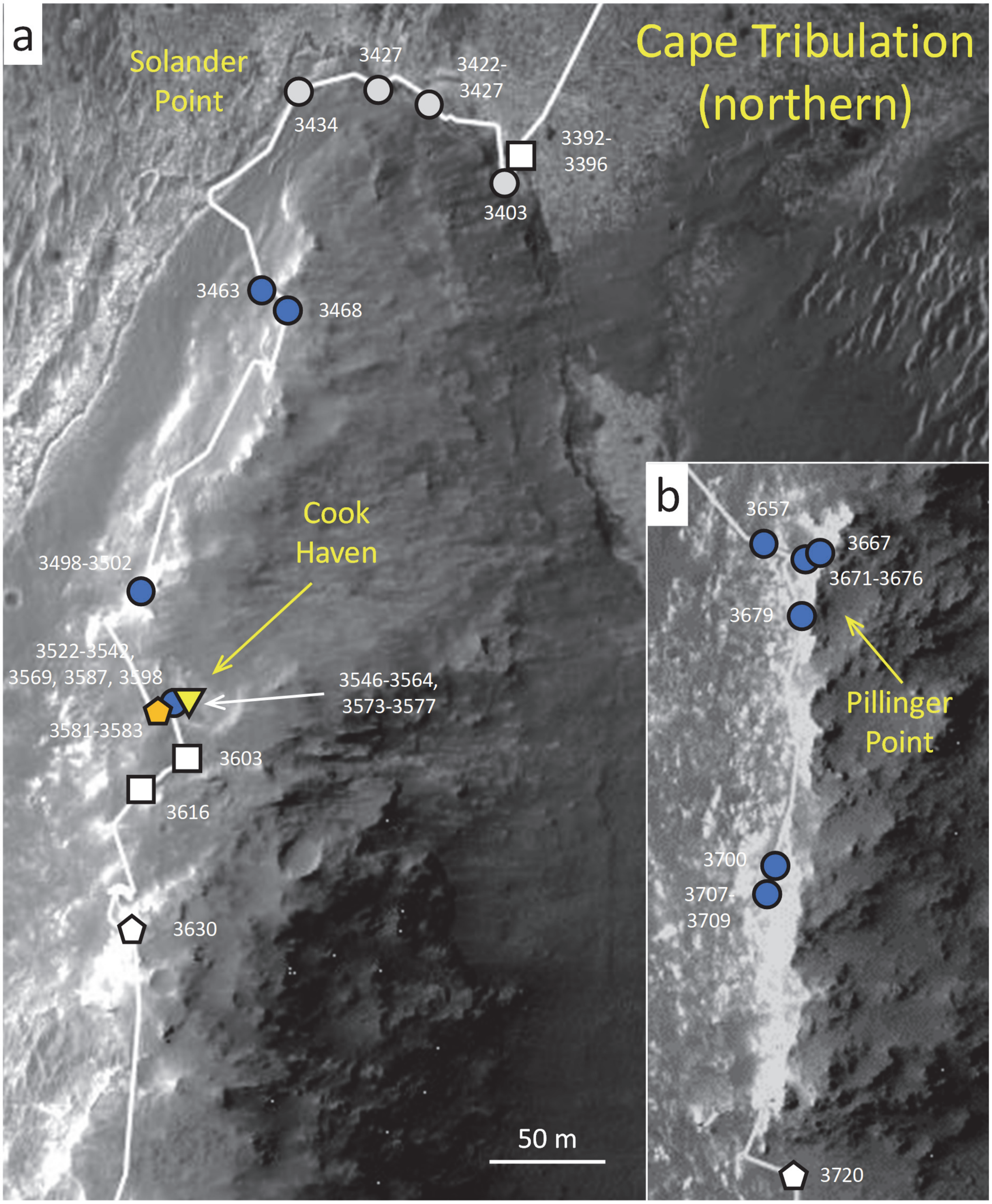

Figure L15. Locator image for the APXS targets identified by Sol and type; see legend on page 12.

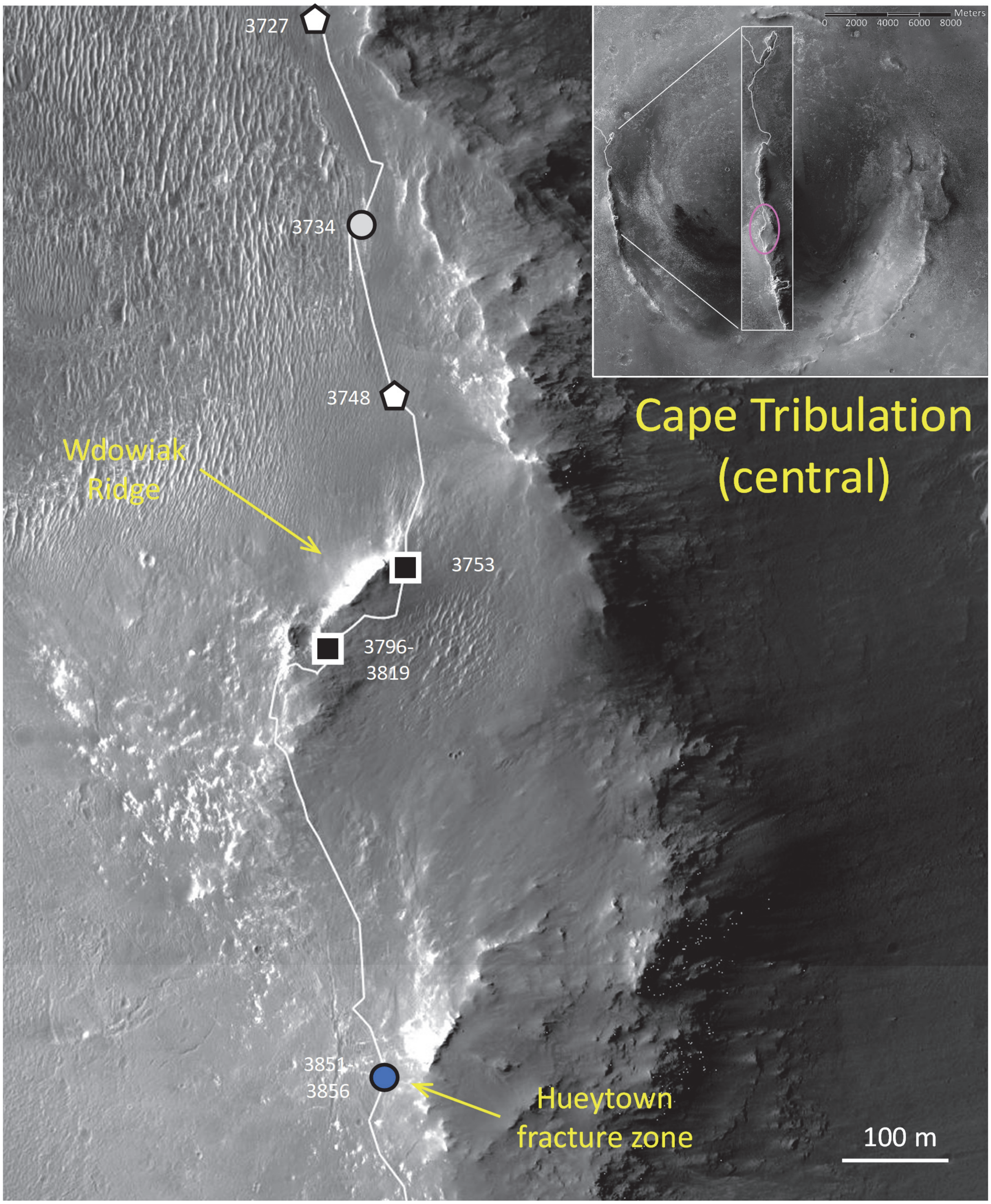

Figure L16. Locator image for the APXS targets identified by Sol and type; see legend on page 12.

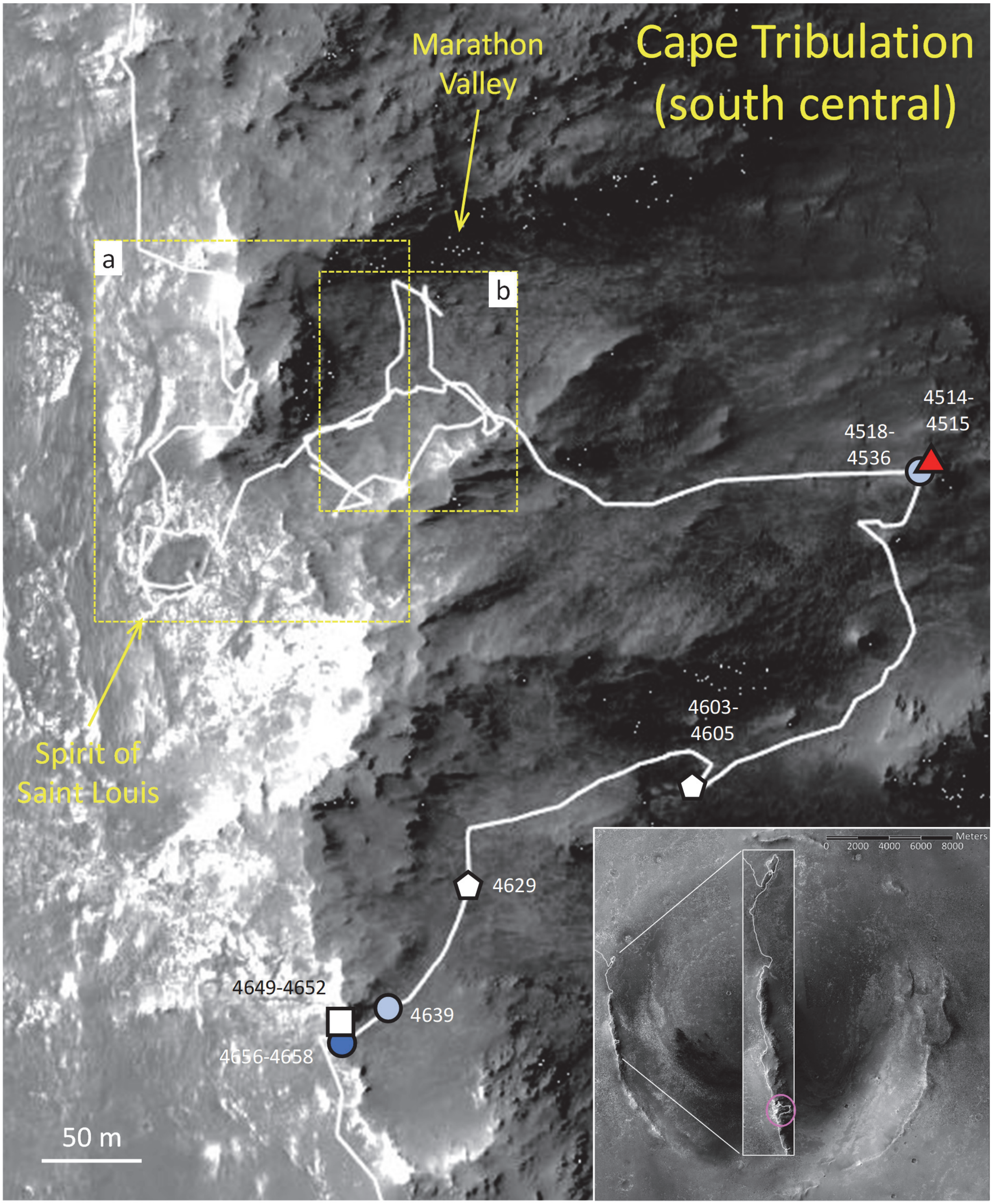

Figure L17. Locator image for the APXS targets identified by Sol and type; see legend on page 12.

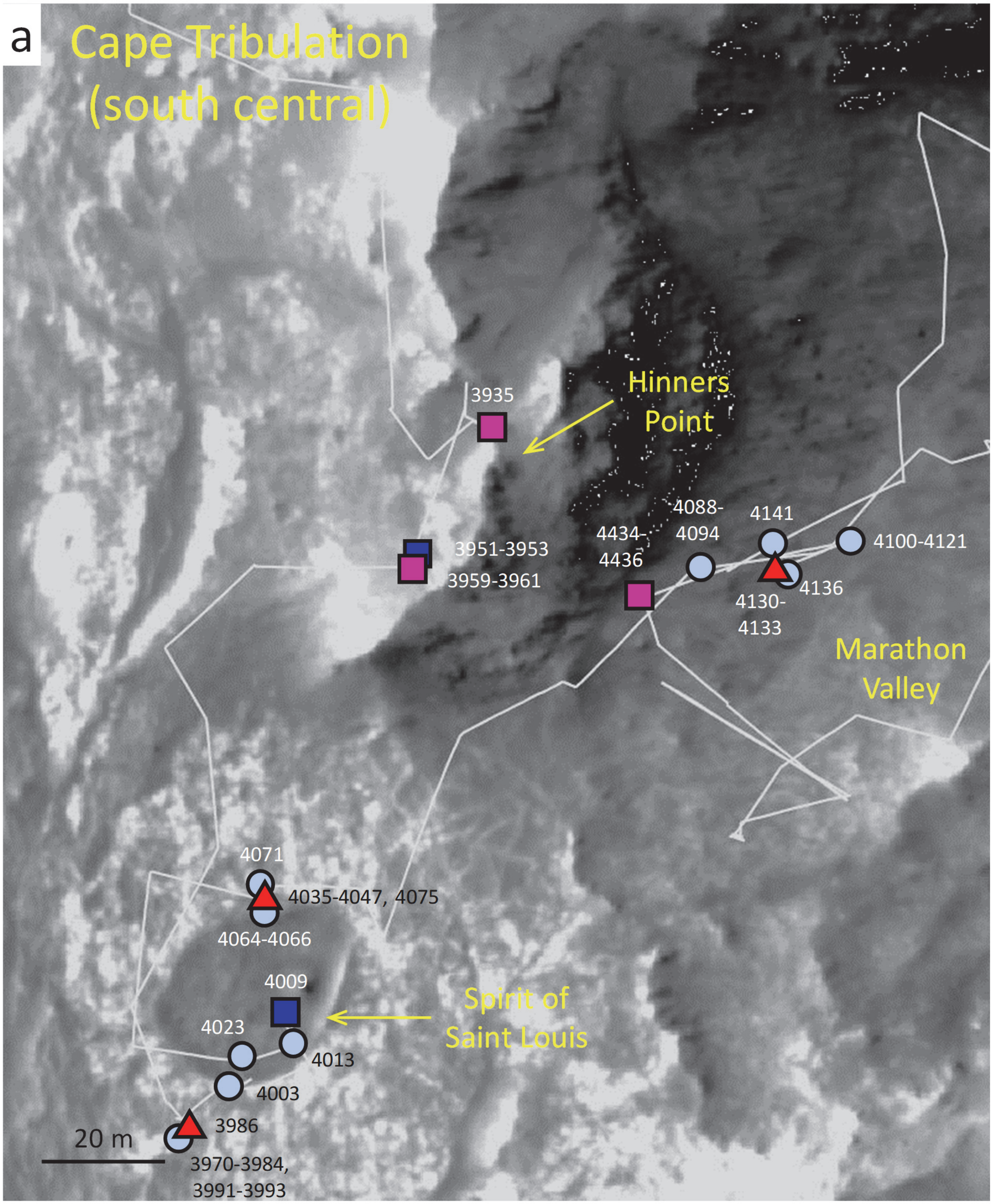

Figure L18. Locator image for the APXS targets identified by Sol and type; see legend on page 12.

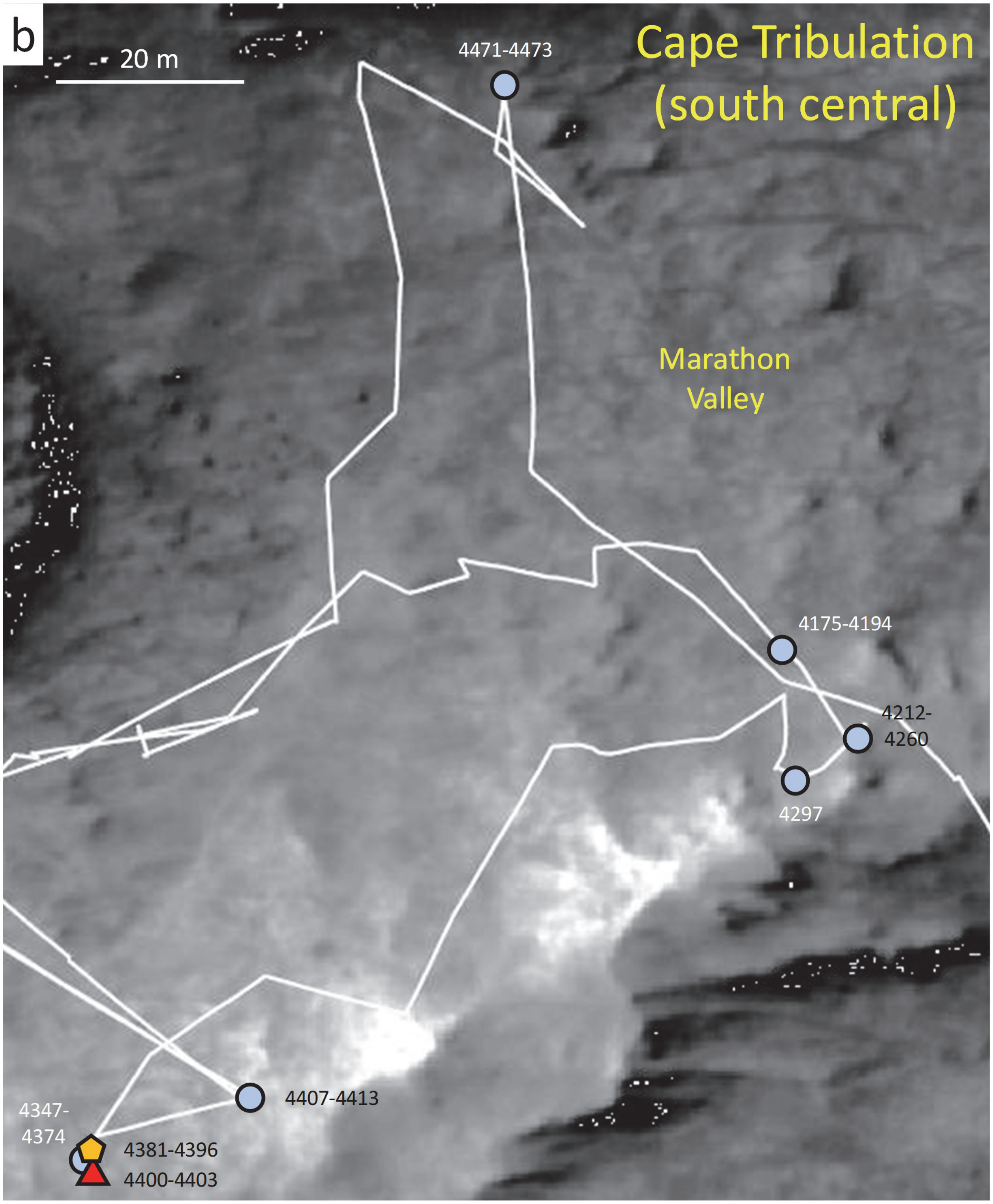

Figure L19. Locator image for the APXS targets identified by Sol and type; see legend on page 12.

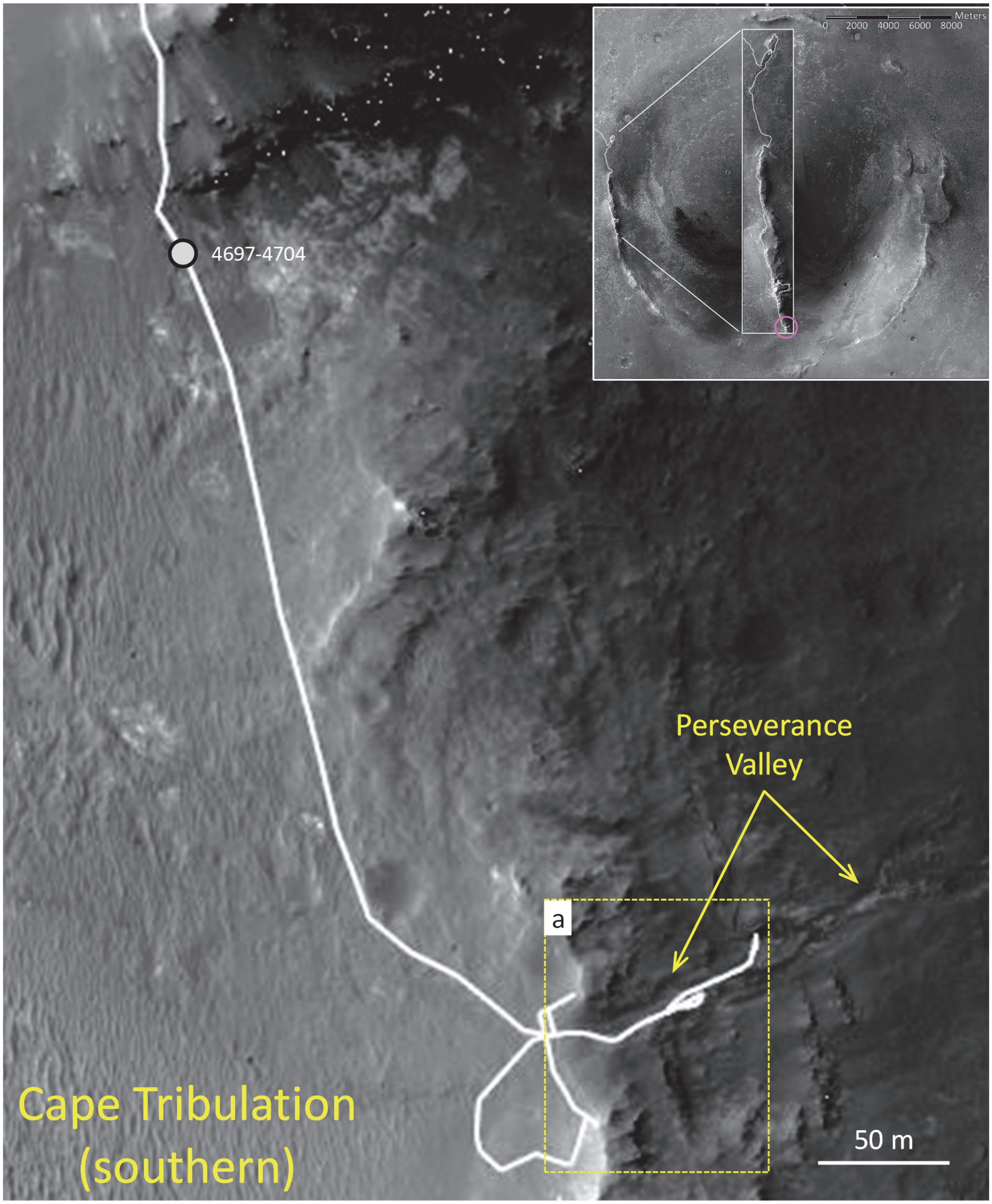

Figure L20. Locator image for the APXS targets identified by Sol and type; see legend on page 12.

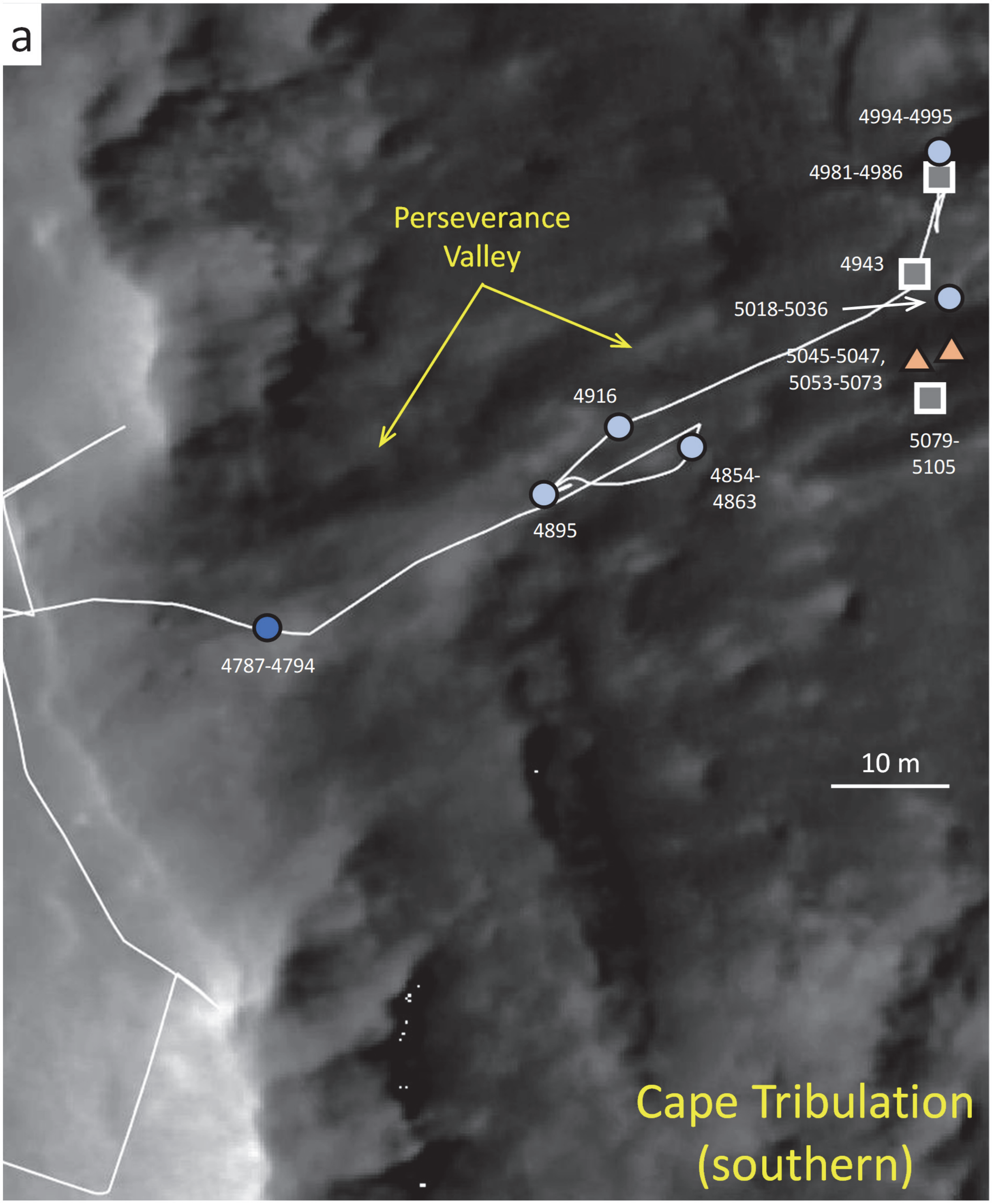

Figure L21. Locator image for the APXS targets identified by Sol and type; see legend on page 12.